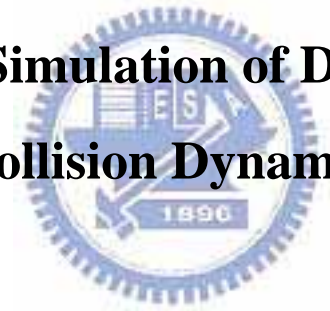# 國立交通大學

機械工程學系

博 士 論 文

應用平行化分子動力學模擬法於液滴–液滴間

碰撞力學之研究

Parallel MD Simulation of Droplet-Droplet Collision Dynamics

研 究 生：許祐霖

指導教授：吳宗信 博士

中 華 民 國 九 十 五 年 七 月

應用平行化分子動力學模擬法於液滴-液滴間碰撞力學之研究

Parallel MD Simulation of Droplet-Droplet Collision Dynamics

研 究 生：許祐霖   Student：Yu-Lin Hsu

指導教授：吳宗信 博士   Advisor：Dr. Jong-Shinn Wu

國 立 交 通 大 學
機 械 工 程 學 系
博 士 論 文

A Thesis
Submitted to Department of Mechanical Engineering
College of Engineering
National Chiao-Tung University
in partial Fulfillment of the Requirements
for the Degree of
Doctor of Philosophy
in

Mechanical Engineering

July 2006

Hsinchu, Taiwan

中 華 民 國 九 十 五 年 七 月

Parallel MD Simulation of Droplet-Droplet Collision Dynamics

Student: Yu-Lin Hsu   Advisor: Dr. Jong-Shinn Wu

Department of Mechanical Engineering

National Chiao-Tung University

Abstract

Collision dynamics between two nanoscale argon droplets with the same diameter of ~10nm under vacuum and pressurized environment is simulated using a parallelized cellular molecular dynamics (PCMD) simulation code. Simulation results show that the collision dynamics between two droplets can be very complicated, which strongly depends upon the magnitude of the background pressure, the relative inertia (or collision velocity) and impact parameter. These phenomena include bouncing, direct coalescence, stretching coalescence, stretching separation and shattering. Regime maps at different background pressures are constructed for the first time to the best knowledge of the author. Analysis of snapshots of molecular distribution, fragment size distribution, surface tension on droplet surfaces and energy transfer process during collision are used to explain the complicated collision dynamics. The research is

divided into two phases, which is described as follows.

In the first phase, a PCMD code is developed on memory-distributed parallel machines (e.g., PC-cluster system) by taking advantage of link-cell data structure, which is often used for fast search in constructing the Verlet list. Dynamic spatial domain decomposition using multi-level graph-partitioning technique is employed to enforce the load balancing among processors. A simple threshold scheme (STS), in which workload imbalance is monitored and compared with some threshold value during the runtime, is proposed to decide the proper time for repartitioning the domain. Results show that the parallel efficiency using one million L-J atoms reaches 57%, 35% and 65%, respectively, for condensed, vaporized and supercritical test cases at 64 processors of HP clusters at NCHC.
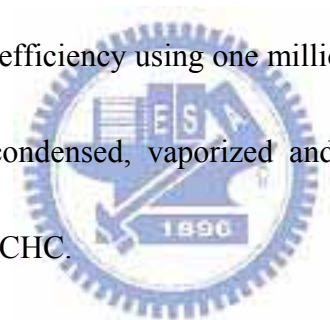
In the second phase, the above developed PCMD code using L-J (12-6) potential is used to study the collision dynamics between two nanoscale droplets under vacuum and pressurized environments. Test conditions will include variations of the impact parameter (0-8 nm), relative velocity of droplets (20-1500 m/s), background gas pressure (0, 0.055 and 0.55 atm; $\rho_{droplet}/\rho_{ambient} = \infty$, 2312.3 and 216.9) and the background gas temperature is 216K. Observed phenomena can be categorized as bouncing, direct coalescence, stretching coalescence, stretching separation and shattering. Distributions of these regimes, as a function of relative velocity and impact

parameter, are constructed for the first time for different background gas pressures. The simulation results under vacuum condition show that disruption, fragmentation and shattering can be easily observed at higher relative velocities, while direct coalescence can only be found at lower relative velocities. However, with the existence of background gas, disruption and fragmentation can only be observed at higher velocities than those under vacuum conditions. Bouncing at very low velocity (10-30 m/s) can be clearly observed under pressurized environments, which coincides with previous findings. In addition, stretching coalescence is observed for the first time at intermediate relative velocity and impact parameter under pressurized environment. Effects of the relative velocity, impact parameter and ambient pressure to the collision process are discussed in detail using the concept of the separable rotational energy and the vibration energy of the largest cluster during collision.

應用平行化分子動力學模擬法於液滴-液滴間碰撞力學之研究

學生: 許祐霖   指導教授: 吳宗信 博士

機械工程學系博士班

國立交通大學

中文摘要

本論文是利用平行化分子動力學程式(Parallelized cellular molecular dynamics. PCMD)來模擬探討兩個在奈米尺度下由氬(Argon)原子所構成的相同直徑(~10nm)的液滴在真空環境下以及含背壓環境狀態下的碰撞動力學行為。由模擬的結果,我們觀察到其動力學行為十分複雜,而且模擬的背壓條件、液滴間的相度速度以及碰撞參數(Impact Parameter) 對液滴碰撞後的行為都有決定性的影響。模擬中觀察到的行為有:液滴彈性碰撞(Bounce)、液滴結合(Direct Coalescence)、液滴變形結合(Stretching Coalescence)、液滴拉伸破裂(Stretching Separation)以及液滴碎裂(Shattering)。我們首次建構了在不同背壓條件下的液滴行為區域圖。並著利用分析,碰撞後的液滴尺寸分布以及碰撞間能量的轉換情形來進一步的解釋複雜的液滴碰撞動力學行為。本論文研究可以區分為以下兩個主要部份

第一部分,我們發展了一個在Memory-distributed 的平行計算器上(例如:

PC-cluster 系統)上執行的平行化分子動力學程式(PCMD)，結合Link-cell的結構資料的優點，來快速的搜尋建立Verlet-list。並且於動態區域切割中採用Multi-level Graph-partitioning的技巧來確保每個處理器中負載均衡。設計簡易負載重新分配機制(Simple Threshold Scheme)，當某一工作區域的負載超過設定值時，將重新分割計算區域。以一百萬顆L-J atoms為例，在不同的熱力學狀態（Condensed Vaporized Supercritical）下其平行效率分別可以達到57%、 35% 以及 65%。

第二部份中，我們利用第一部份所發展的PCMD程式以及L-J(12-6)的勢能模型，來研究兩個奈米尺度下的液滴於真空環境以及含背壓環境下的的碰撞動力學行為。測試的條件包括，不同的Impact Parameter (0-8 nm) 不同的液滴間相對速度(20-1500 m/s)以及不同的背壓環境(0, 0.055 and 0.55 atm)。觀察到的行為有可以區分為Bounce、Direct Coalescence、Stretching Coalescence、Stretching Separation以及Shattering。真空環境下，相對速度較高時可以容易的觀察到Disruption、Fragmentation及Shattering的行為，而Direct Coalescence和Stretching Coalescence則發在相對速對較低時。而當背壓氣體存在時，Disruption及Fragmentation發生時所需要的相對速度則高於真空狀態下。液滴的Bounce行為則存在於極低的相對速度下，並且Bounce只有在背壓存在時才發生，這與之前的文獻十分吻合。另外，本文中提及Stretching Coalescence的現象則是第一次被發現。針對相對速度、碰撞參數以及背壓對液滴碰撞過程的影響，我們將在本文中利用最大破裂液滴的Rotational energy及Vibration energy的方式分別做詳細的討論。

關鍵字：平行網格化分子動力學、動態化空間分割、平行效率、簡易負載重新分配機制、液滴碰撞、液滴破裂

誌　謝

Table of Contents

List of Tables

xiii

List of Figure

Nomenclature

ρ : density

τ : surface tension

k_B : Boltzmann's constant

$v_{rot,i}$: angular velocities of i atom

D : diameter of droplet

r : radius of droplet

r_i : the position vector of molecule i

F_i : the force vector of molecule i

p_i : the momentum vector of molecule i

V : relative velocity

U : potential

N : number of density

n : number of atoms

T : temperature

T_{vib} : vibrational temperature

E : energy

E_{rot} : rotational energy
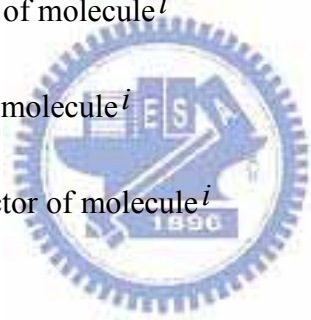
Chapter 1 Introduction

1.1 Motivation

1.1.1 Droplet collision dynamics

Droplet collision dynamics plays a key role in various technologies such as, spray combustion, ink-jet printing, rain drop formation, insecticide spraying, nuclear fusion, surface coating, and solidification, among others. In addition, collision between two droplets becomes the most frequent event in theses applications. Thus, understanding of the fundamental collision dynamics between two droplets becomes crucial in optimizing these applications. Depending upon the size of the droplets, descriptions of the collision dynamics can be generally classified into continuum-scale and atomic-scale, which are described next.
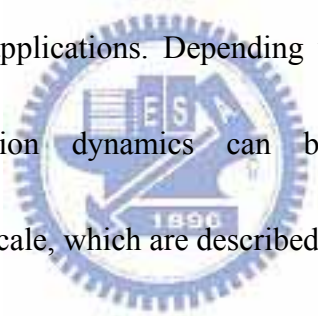
1.1.2 Continuum-scale description

Process of droplet collision itself is very complicated, while it follows conservation of energy, conservation of momentum, and conservation of angular momentum. In a collision, the droplet loses kinetic energy as the droplet strains and deforms. The strains lead to viscous dissipation, accounting for some conversion of mechanical energy to heat. More importantly, the droplet surface increases as the original droplet breakdowns into smaller ones and surface energy increases accordingly. The surface energy can be viewed as a potential energy and conversion

of kinetic energy to surface energy can be viewed as a conservative process. The increase of surface energy during the early part of a collision results in recoiling and rebounding later through the conversion of surface energy back to kinetic energy. The momentum balance occurs through a force imposed on the droplet by the other droplet in a collision as the droplet loses inertia and possibly rebounds in the other direction. For collisions between droplets that are not head-on, we can expect that conservation of angular momentum acts through a torque imposed during collision, which makes the colliding droplet rotating.

Collision dynamics between two droplets had attracted much attention in continuum scale, while it had not been well studied in the atomic scale. In this thesis, we intend to fill in this gap to provide more detailed inside about droplet collision dynamics in the nanoscale regime.
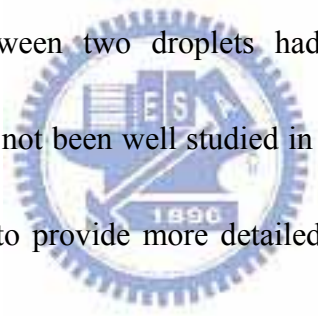
1.1.2 Atomic-scale description

In the atomic scale, continuum-scale description may fail since continuum assumption may breakdown due to very large gradient of properties caused by very small length scale. Droplet collision in this scale requires different approaches as those in continuum scale. One of the most often adopted approaches is to utilize molecular dynamics (MD) simulation to understand these non-equilibrium phenomena. Also it is interesting and possibly important in the present

nanotechnology to understand if the collision dynamics bwteen two nanoscale

droplets share the same physical pictures as those in the continuum scale? In addition,

understanding of the atomic-scale collision dynamics may further improve the

understanding of the continuum-scale collision dynamics.

1.2 Background

1.2.1 Droplet collision dynamics

In this thesis, we focus on the collision dynamics between two nanoscale droplets.

Based on the understanding in the continuum scale, droplet collision can be generally

classified into different types of collision depending on some critical parameters, as

shown in Fig. 1.1. These different types of collision process are introduced next.
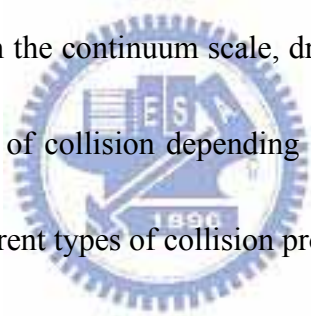
1.2.1.1 Droplet bouncing

Droplets bouncing occurs if the surfaces of the droplets do not make contact due

to the presence of a thin intervening gas film in between. In this case the droplet's

surfaces undergo a flattening deformation, but the surfaces do not make contact since

the kinetic energy of collision (CKE), is insufficient to expel the intervening layer of

gas.

1.2.1.2 Droplet coalescence

Droplet coalescence, in which an integrated post-collision droplet is formed

whose mass is equal to the sum of the mass of the pre-collision droplets, follows after

the droplet contacts. The colliding droplets coalesce when the air film thickness

reaches a critical value (~10^2 Å, Mackay *et. al*.[1963]). The droplets may coalescence

temporarily or permanently, depending on the CKE and impact parameter (*b*).

1.2.1.3 Disruption and fragmentation

Temporary coalescence occurs when the *CKE* exceeds the value for stable

coalescence and eventually results in either disruption or fragmentation. Disruption is

that case when the collision product separates into the same number of droplets which

exists prior to the collision. A collision resulting in bouncing may be difficult to

distinguish from the case when the temporary coalescence followed by disruption

results in two droplets with masses equal to the pre-collision droplet masses. As for

fragmentation, the coalesced droplet undergoes catastrophic break-up into numerous

small droplets.
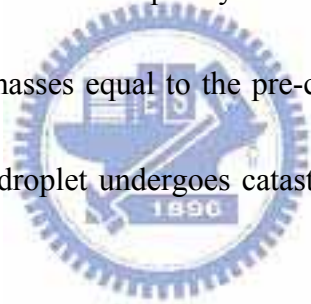
1.2.2 Crucial parameters in describing droplet collision dynamics

1.2.2.1 Continuum-scale description

In the continuum scale, it is convenient to characterize the collision process in

terms of the Webber number (*We*), the impact parameter (*b*) and Kinetic energy of

collision (*CKE*). Schematic diagram showing different droplet collision regimes as

functions of Weber number (***We***) and impact parameter (***b***) is shown in Fig. 1.3.

Physical meaning of the above these important parameters are described in the

following for completeness.

1.2.1.1.1 Weber number (*We*)

The *Webber number* is the ratio of the inertial force to the surface force and is

defined as:

$$We = \rho V^2 D_s / \tau \tag{1.1}$$

where ρ is the droplet density, D_s is the diameter of the smaller droplet and τ is

the surface tension of the droplet fluid.

1.2.1.1.2 Impact parameter (*b*)

The impact parameter (*b*), (Fig. 1.3), is defined as the distance from the center of

one droplet to the relative velocity vector placed on the center of the other droplet.

1.2.1.1.3 Kinetic energy of collision (C.K.E)

The kinetic energy of collision (*CKE*) of the droplet pair with the same droplet

fluid is given by (Low and List [1982]):

$$CKE = \frac{\rho\pi}{12}\left(\frac{D_L^3 D_S^3}{D_L^3 + D_S^3}\right)(V_L - V_S)^2 \tag{1.2}$$

The above can be rewritten as:

$$CKE = \frac{\rho\pi}{12}\left(\frac{D_L^3}{R^3 + 1}\right)(V_L - V_S)^2 \tag{1.3}$$

where R is the droplet size ratio r_L / r_S. Where r_L and r_S is radius of droplet large

and droplet small, respectively.

1.2.2.2 Atomic-scale description

In the atomic scale, characterizing the droplet collision using the

above-mentioned parameters may be misleading. Alternative way of description

becomes necessary. Among these, description using the concept of N-body dynamics Jellinek and Li [1989] may become a reasonable way to highlight the underlying physics of the collision process. In what follows, we briefly introduce the concept of N-body dynamics in section 2.8.5.

1.3 Literature reviews

1.3.1 Droplet growth

Hu, *et al*. [1998], propose the stochastic growth of cloud droplet distributions due to collection processes is studied using a detailed microphysical parcel model. The evolution of rainwater content (L-R) and the radar reflectivity factor (Z) are plotted in order to trace the progress of transfer of cloud water into rainwater and determine the importance of droplet collection in different size ranges. The results indicate that the van der Waals forces are effective in enhancing droplet collision when the droplets are small and the distributions are narrow.
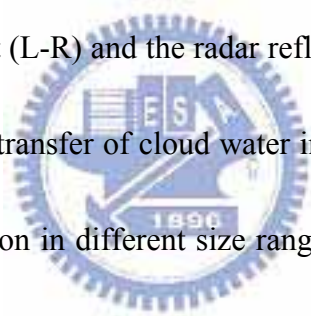
1.3.2 Droplet-droplet collision

Ashgriz and Poo [1990] carried out collision experiments with water drops in the micrometer to millimeter size range. Two drop streams collided with relative velocities of 1–20 m/s, and single collisions were followed with high-speed video recording. Two different types of separating collisions were identified, reflexive and stretching separating, and they determined the boundaries between these processes

and coalescence. Reflexive separation was found for near head-on collisions with high

velocity while stretching separation occurred for large impact parameter.

Pan and Law [2004], presented a dynamics of head-on collision between two

identical droplets was experimentally and computationally investigated, with

particular emphasis on the transitions from merging to bouncing to merging again as

the collision Weber number increased.

Later, Pan and Law [2005] extend the research to a head-on collision of a droplet

onto a liquid layer of the same material, sitting on a solid surface. Both experimental

and computational methods were applied to illuminate the transition from bouncing of

the droplet to its absorption by the film for given droplet Weber number, *We*, and the

film thickness scaled by the droplet radius, H_f.
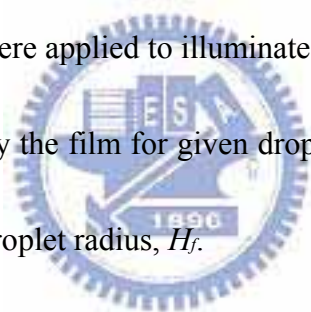
1.3.3 Simulation methods for droplet collision dynamics

The simulation methods for droplet collision dynamic can be classified into two

major groups, depending on the size scale of simulation system. as the

continuum-scale and ***atomic-scale*** methods.

1.3.3.1 Continuum-scale simulation methods
1.3.3.1.1 Navier-Stokes equation method

Harlow and Shannon [1967] were the first to simulate droplet impact on the solid

surface. They used a "marker-and-cell" (MAC) finite-difference method to solve the

fluid mass and momentum conservation equations. Tsurutani *et al*. [1990] enhanced

the MAC model to include surface tension and viscosity effects, and also considered

heat transfer from a hot surface to a cold liquid droplet as it spread on the surface.

Trapaga and Szekely [1991] used the "volume of fluid" (VOF) method, to study

impact of molten particles in a thermal spray process. Liu et al. employed another

VOF based code, to simulate molten metal droplet impact. Zhao *et al*. [1996]

formulated a finite-element model of droplets deposited on solid surfaces.

Adaptive-grid finite element methods were used first by Fukai *et al*. [1995] to

simulate water droplet impact, and later by e.g., [Bertagnolli *et al*., 1997], [Waldvogel

and Poulikakos, 1997] to study thermal spraying of molten ceramic particles.

Bussmann *et al*. [1999] publish a description of a three-dimensional,

fine-difference, fixed-grid *Eulerian* model the developed, to simulate water droplets

falling with low velocity (~1m/s), onto either an inclined plane or the edge of a step.

Pasandideh-Fard *et al*. [2002] extended the 3-dimensional model of Bussmann's

model to include heat transfer and solidification. In addition, they also accommodate

the presence of an irregular moving solidification front within the computational grid.

1.3.3.1.2 Lattice Boltzmann methods

Lattice Boltzmann method [Succi, 2001] excels in modeling flow problems

involving multiphase materials and complicated geometry. It is highly suitable to

model the droplet collision dynamics. For example, Inamuro, *et al*. [2004] presented a

lattice Boltzmann method for two-phase fluid flows with large density ratios and

applied the method to the simulations of binary droplet collisions for various Weber

numbers and impact parameters. They simulated the there exist other types of binary

droplet collisions under certain conditions, bouncing collision for low Weber numbers

and shattering collision (Disruption or fragmentation) for high Weber numbers and

discussed the mixing processes in different conditions.

1.3.3.2 Atomic-scale simulation methods
1.3.3.2.1 Molecular dynamics under vacuum

Greenspan and Heath [1991] studied the collision dynamics of nanometer-sized

particles. They carried out classical trajectory calculations of collisions between water

clusters with a size of 2051 monomers. The individual molecules were modeled as

single mass particles and the molecule–molecule interaction was described by a

Lennard–Jones potential. Different modes that the colliding system could obtain were

identified and compared with observations made for colliding large drops.
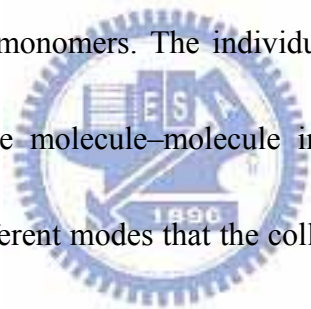
Gay and Berne [1986] studied head-on collisions between clusters where the

atom–atom interaction was described by a L-J pair potential. They varied the cluster

size ~19–135 atoms/cluster in the same temperature, and relative velocity and found

that the collisions were accompanied by internal heating and that the clusters

coalesced.

Svanberg *et al*. [1997] performed MD calculations of collision between Ar_{1000}

clusters to investigate the effects of relative velocities (100-1000 m/s) and impact

parameter (0-4 nm) on energy transfer and dynamical behavior.

Later, Svanberg *et al*. [1998] increased the complexity of the system and studied the droplet collision dynamics of liquid-like water clusters with an internal temperature of 300K. Collisions between $(H2O)_n$ (n=125, 1000), and investigated the effects of cluster velocity and impact parameter on the outcome of the collisions.

Blaisten–Barojas and Zachariah [1992] studied Si_{15}–Si_{15} collisions at a temperature of about 2000K using molecular dynamics. Chen *et al*. [1993] carried out molecular dynamics simulations of Au_{55}-Au_{55} collisions using an embedded atom method potential. Collisions with clusters initially at 0 or 300K were studied, and all collisions resulted in cluster aggregation with significant inelastic deformation of the original clusters.
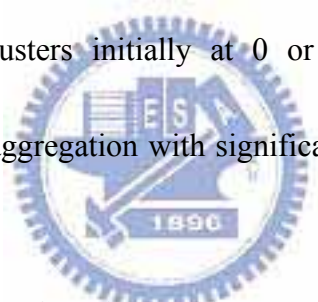
1.3.3.2.2 Molecular dynamics with ambient gas

Murad and Law [1999] presented a molecular dynamic simulation with L-J potential for droplet–droplet collision with ambient gas. Bouncing between droplets was only found within a narrow band of state conditions collision, which is mainly attributed to the existence of background gas. However, not much parametric study has been conducted to further understand the effects of the ambient pressure..

Based on the reviews in the above, only preliminary studies have been done in the simulation of nanoscale droplet-droplet collision. Understanding of the droplet collision dynamics may become important in the fast-growing nano science and

technology. Thus, MD simulation will be used to study the physics of the droplet-droplet collision dynamics in the nanocale regime.

1.4 Objectives of the thesis

The specific objectives of the thesis are summaried as follows:

1. To develop and verify a parallelized cellular molecular dynamics (PCMD) simulation code, which takes advantage of the link-cell data structure, using dynamic domain decomposition.

2. To study and explain the droplet-droplet collision dynamics in the nanoscale regime using the developed PCMD code under vacuum and pressured environment.

1.5 Organization of the thesis

In this thesis, Chapter 2 describes the classical MD simulation method and some specific ways of MD data analysis used in the present thesis. Chapter 3 describes the past efforts in parallel MD method, the proposed PCMD method in detail and its resulting parallel performance. Chapter 4 describes the simulation of droplet-droplet collision dynamics using the PCMD code. Finally, Chapter 5 describes the concluding remarks with some recommendation for the future study.

Chapter 2 Molecular Dynamics Simulation

2.1 Basic molecular dynamics simulation

Molecular dynamics (MD) has been widely used to simulate properties of liquids, solids, and molecules in several research disciplines. It is an important approach to understand microscopic character of nature. MD is derived form a new concept called, phase trajectory. We computed the trajectories of molecules using classical Newtonian mechanics and we described features of the molecule trajectory in classical nonlinear dynamics. And obtain properties by analyze the trajectory with kinetic theory, statistical mechanics, and sampling theory. In addition, periodic boundary conditions and conservation principles are used to hold accuracy of MD simulation. Combined these tools form the foundation of molecular dynamics.

Newtonian Second Law:

$$F_i = m\ddot{r}_i = m\frac{d^2 r_i}{d^2 t^2} \tag{2.1}$$

where r_i is the position vector of molecule i as shown in Fig. 2.1

Since Newton's second law is time independent or equivalently $F_i = m\ddot{r}_i = m\frac{d^2 r_i}{d^2 t^2}$ is invariant under time translations. Consequently, we expect there to be some function of the positions and velocities whose value is constant in time; this function is called the Hamiltonian,

$$H(r^N, p^N) = const \tag{2.2}$$

where $p_i = m\dot{r}_i$ is the momentum of molecule i.

For an isolated system, total energy E is conserved, where E is equal to the sum of kinetic energy and potential energy. Thus, for an isolated system, we identify total energy as the Hamiltonian; then for N spherical molecules, H can be written as

$$H(r^N, p^N) = \frac{1}{2m}\sum_i p_i^2 + U(r^N) = E \tag{2.3}$$

where $U(r^N)$ results from the intermolecular interactions.

First consider the total time derivative of the general Hamiltonian (2.2),

$$\frac{dH}{dt} = \sum_i \frac{\partial H}{\partial p_i} \cdot \dot{p}_i + \sum_i \frac{\partial H}{\partial r_i} \cdot \dot{r}_i + \frac{\partial H}{\partial t} \tag{2.4}$$

If, as is (2.3), H has no explicit time dependence, then the last term on the RHS of (2.4) vanishes and we are left with, due to H=const,

$$\frac{dH}{dt} = \sum_i \frac{\partial H}{\partial p_i} \cdot \dot{p}_i + \sum_i \frac{\partial H}{\partial r_i} \cdot \dot{r}_i = 0 \tag{2.5}$$

If Hamiltonian is expressed as (2.6), then

$$\frac{dH}{dt} = \frac{1}{m}\sum_i p_i \cdot \dot{p}_i + \sum_i \frac{\partial U}{\partial r_i} \cdot \dot{r}_i = 0 \tag{2.6}$$

On comparing (2.5) and (2.6), we find for each molecule i,

$$\frac{\partial H}{\partial p_i} = \frac{p_i}{m} = \dot{r}_i \tag{2.7}$$

and $\quad \dfrac{\partial H}{\partial r_i} = \dfrac{\partial U}{\partial r_i}$ (2.8)

Substituting (2.7) into (2.5) gives

$$\sum_i \dot{r}_i \cdot \dot{p}_i + \sum_i \dfrac{\partial U}{\partial r_i} \cdot \dot{r}_i = 0 \qquad (2.9)$$

or $\quad \displaystyle\sum_i (\dot{p}_i + \dfrac{\partial H}{\partial r_i}) \cdot \dot{r}_i = 0$ (2.10)

Since the velocities are all independent of one another, (2.10) can be satisfied only, for each molecule i, we have

$$\dfrac{\partial H}{\partial r_i} = -\dot{p}_i \qquad (2.11)$$

Eq.(2.7) and (2.11) are Hamilton's equation of motion. For a system of N particles, (2.7) and (2.11) represent 6N first-order differential equations that are equivalent to Newton's 3N second-order differential equations (2.1).

In the Newtonian view, motion is a response to an applied force. However, in the Hamiltonian view, motion occurs in such a way as to preserve the Hamiltonian function, where the force does not appear explicitly.

For an isolated system, the particles move in accordance with Newton's second law, tracing our trajectories that can be represented by time-dependent position vectors $r_i(t)$. Similarly, we also have time-dependent momentum $p_i(t)$.

At one instant, there are positions and momenta of the N particles in a

6N-dimensional hyperspace. Such a space, called phase space, is composed of two parts: a 3N-dimensional configuration space, in which the coordinates are the components of position vectors $r_i(t)$, and a 3N-dimensional momentum space (or velocity space), in which the coordinates are the components of the momentum vectors $p_i(t)$. As time evolves, the points defined by positions and momentum in the 6N phase space moves, describing a trajectory in phase space.

2.2 Potential model

We can say that the potential model is the role of molecular dynamic simulation. As you want approach the different realistic material in simulation, you have to change the potential model. Because the force on an atom in simulation is due to interaction with surrounding neighbors. And the force is derived from potential. To creative a potential model you must to do a lot of abstruse computations in Quantum Chemistry. Fortunate, there are a lot accurate potential model had been devised by chemists and physicists, today. There are some potential models will be introduce as follow.

2.2.1 Lennard-Jones potential

The potential first introduced by J.E. Lennard-Jones [1924]. The pair-wise intermolecular potential form as follow:

$$U(r_{ij}) = 4\varepsilon[(\frac{\sigma}{r_{ij}})^{12} - (\frac{\sigma}{r_{ij}})^6], \quad r_{ij} \leq r_c \tag{2.12}$$

where $r_{ij} = r_i - r_j$ and is shown in Fig.2.2. The parameter ε presents the strength

of the interaction and σ defines a length scale. This potential repels at close range,

then attracts, and is eventually cut off at some limiting separation r_c. While the

strongly repulsive core arising from the nonbonded overlap between the electron

clouds has a rather arbitrary form (other powers and functional form are sometimes

used), the attractive tail actually represents van der Waals interaction due to electron

correlations. Most importantly, this L-J potential assumes the interactions involve

individual pairs of atoms: each pair is treated independently, with other atoms in the

neighborhood having no effect on the force between them.
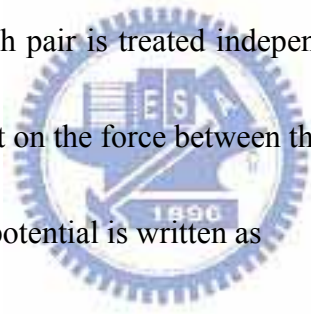
Force resulting from LJ potential is written as

$$f = -\nabla U(r) \tag{2.13}$$

or $\quad f_{ij} = (\frac{48\varepsilon}{\sigma^2})[(\frac{\sigma}{r_{ij}})^{14} - \frac{1}{2}(\frac{\sigma}{r_{ij}})^8]r_{ij}$ (2.14)

provided $r_{ij} \leq r_c$, zero otherwise and is shown in Fig. 3.2. As r increases towards

r_c the force drops to zero, so that there is no discontinuity at r_c; f and higher

derivatives are discontinuous.

In general, we would like to express these equations used in MD in

dimensionless format. There are several reasons for doing this, not the least being the

ability to work with numerical values not far from unity, instead of the extremely

values normally associated with the atomic scale. Another benefits of using dimensionless units is that the equations of motion are simplified because some, if not all, of the parameters defining the model are absorbed into the units. Finally, using such dimensionless units lies in the fact that general notion of scaling can be applied to whole class of problems. Of course, from practical viewpoint, the switch to such units removes any risk of encountering values lying outside the range that is representable by the computer hardware. Units used to nondimensionalize the related MD equations are listed in Table 1 for reference.

2.2.2 Water potential

The biggest difference between the water potential and the L-J potential is the polar and structure of molecule of water potential. For water molecule i and j shown in Fig.2.3, the effective pair potential $u(r_{ij})$ is actually a function of the distances among the two sets of atoms and point changes, That is,

$$u(r_{ij}) = f(r_{13}, r_{14}, r_{16}, r_{18}, r_{23}, r_{24}, r_{26}, r_{28}, r_{35}, r_{37}, r_{45}, r_{47}, r_{56}, r_{78})$$
(2.15)

where the indices *1, 2, 3, 4, 5, 6, 7* and *8* denote the site of atoms or point charges H_1, H_2, H_3, H_4, O_5, O_6, M_7 and M_8.

On the other hand, the rotational motion of water molecule i is simulated based on the angular momentum equation of motion,

$$M_i = \frac{dH_i}{dt}$$
(2.16)

17

where M_i and H_i are the moment vector and angular momentum vector acting on the molecule i.

2.3 Initial conditions

1. A minimum requirement for the MD simulation to be valid is that the results of a simulation of adequate duration are *insensitive* to the initial state, so any convenient initial state is allowed.

2. A particular *simple but practical* choice is to start the with the particles at the sites of some regular lattice, e.g., the square or simple cubic lattice, and spaced to give the desired density.

3. The velocities are assigned random directions and a fixed magnitude based on temperature.

4. The speed of equilibration to a state in which there is no memory of this arbitrarily selected initial configuration is normally quite rapid, so that more careful attempts at the constructing a 'typical" state are of little benefit.
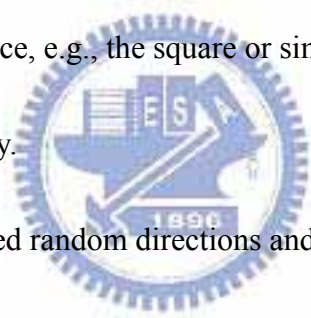
2.3.1 Initial coordinates

For **FCC** lattice, there are *four atoms per unit cell*, and the system is centered at the origin.

2.3.2 Initial velocities

The velocity magnitude is fixed, each velocity vector is assigned a random direction, and the velocities are then adjusted to ensure that the center of mass is at rest.

2.3.3 Initialization of integration variables

For leapfrog method, if the users do not care the minor difference between t=0 and t=Δt/2 in setting the initial velocities, then there is no further work required. If the difference is not to be overlooked, a single interaction computation is all that is required.

2.4 Boundary condition

2.4.1 Periodic boundary Condition

Unless the purpose of the MD simulation is to capture the physics near real walls, a problem that is actually of considerable importance, walls are better eliminated by using periodic boundary conditions (PBC). Physical meaning of periodic boundary conditions is shown in Fig. 2.4. The introduction of PBC is equivalent to considering an infinite space-filling array of identical copies of simulation region.

There are some consequences of this PBC:

1.   A particle that *leaves* the simulation region through a particular bounding

face immediately *reenters* the region through the opposite face.

2. A *wraparound effect* needs to be considered. Particles lying within a distance r_c of a boundary interact with particles in an adjacent copy of the system, or, equivalently, with particles near the opposite boundary.

3. This wraparound effect of the PBC must be taken into account in both the *integration of the equations of motion* and the *interaction computations*. (checking the coordinates of particles if they move outside the region.)

4. Periodic boundary conditions are most easily handled if the region is rectangular in two dimensions, or a rectangular prism in three dimensions. This is not an essential requirement, and any space-filling convex region can be used, although the boundary computation is not as easy as those in rectangular one. The motivation to choose alternative region shapes is to *enlarge the volume to surface ratio*, thus increase the maximum distance between particles before periodic ambiguity appears.

5. Using PBC will restrict the interaction range to *no more than half* the smallest region dimension.

6. Even with PBC, finite-size effects are still present. So how big the simulation region should be? It depends on what kind of system and the properties of the interest. As a minimum requirement, the size should

exceed the range of any significant correlations. Only detailed numerical experiments can hope to resolve this question.

2.4.2 Wall boundary conditions

When we simulate some problems, we would like to keep the wall isothermal. For the purpose, we define a correction layer on wall ,and there are two ways to modify correction layer on wall ; one is Rescaling method, the other is Langevin method.

2.4.2.1 Rescaling method

Rescaling method keep wall isothermal by modify total kinetic energy .In microcosmic size, temperature is related to kinetic energy, when we set the temperature of correction layer ,it means to set the average kinetic energy of atoms on the correction layer, so we must keep the kinetic energy fixed. (Eq. 2.17), so we have a reference valve. Then, use Eq.2.18 we compute the total kinetic energy of atoms. Finally, we start rescaling by using Eq.2.19 to make the total kinetic energy in the correction layer is the same as reference value which we computed in Eq.2.18

$$E_{kd} = \frac{3}{2} N k_B T_d \tag{2.17}$$

$$E_{Ka} = \frac{1}{2} m \sum_{i=1}^{N} V_i^{old^2} = \frac{3}{2} N k_B T_a \tag{2.18}$$

$$V_i^{new} = V_i^{old} \cdot \sqrt{\frac{E_{kd}}{E_{ka}}} = V_i^* \sqrt{\frac{T_d}{T_a}} \tag{2.19}$$

where
N   : total atoms in the correction layer

k_B : Boltzmann constant

E_{kd} : the total kinetic energy define by T_d

E_{ka} : the total kinetic energy of atoms in the correction layer

T_d : the boundary temperature which we need

T_a : the average temperature of atoms in the correction layer before modification

V_i^{old} : the velocity of atom in the correction layer before modification

V_i^{new} : the velocity of atom in the correction layer r after modification

2.4.2.2 Langevin method

Langevin method keep thermal boundary isothermal by modifying equations of

motion as below

$$m_i \dot{v}_i = -\nabla U - m_i \beta_i v_i + R(t) \qquad (2.20)$$

where

m_i :mass of atom

v_i : atom velocity

β_i :Damping constant

R(t): Random Force ,which average valve is 0

2-5 Force computations

2.5.1 All pairs method

It is the simplest one to implement, but extremely inefficient when the interaction

range r_c is relatively small compared with the linear size of simulation region. In this

case, all pairs must be considered when computing interactions. Resulting

computational time grows as $O(N^2)$, where N is the number of particles. This constraint rules out the method for all but the smaller values of N. Two other techniques, including cell-link and Verlet list, to reduce the grow rate $O(N^2)$ are introduced next in turn.

2.5.2 Cutoff distance method

2.5.2.1 Cell-link

Basic idea of this method is to divide the simulation region into a lattice of small cells, and that the cell width exceeds r_c. If particles are assigned to cells based on their instantaneous positions, then it is obvious that interactions are only possible between particles that are either in the same cell or in immediately adjacent cells. Because of symmetry only half the neighboring cells need to be considered. For example, a total of **14** neighboring cells must be examined in three dimensions (include the cell itself). In addition, the wraparound effects can be readily incorporated into the scheme. In general, the region size must be at least 4 r_c for this method to be useful.

There are several ways of implementing this cell-link list method to connect the relation between particles and cells. In the current demonstration code, it utilizes concept of the pointers for particles and cells. Each cell stores a particle number, which may be zero or nonzero. Nonzero value represents a true particle number, while the zero value represents either the last atom in the cell or an empty cell. In addition,

only one array **cell List** is used to represent the particles and cells. The obvious

advantage of doing this is we know exactly the size of this array in advance if periodic

boundary conditions are used. Of course, there are several other methods to

implement this idea of cell-link list technique. Ideas depicting in the above can be

clearly illustrated as Fig. 2.5:

2.5.2.2 Verlet list

A list of all particle pairs with separation $r_{max} > r_c$ is maintained and updated

every say 10 or 20 time steps. r_{max} is chosen large enough that it is unlikely that a

particle pair not in the list will come closer than r_c before the list is updated. It is also

possible to decide automatically when the neighbor list needs to be updated. When the

list is created, a vector for each particle is set to zero. At each time step, the vector is

incremented by the particle displacement. For example, see the Fig. 2.6.
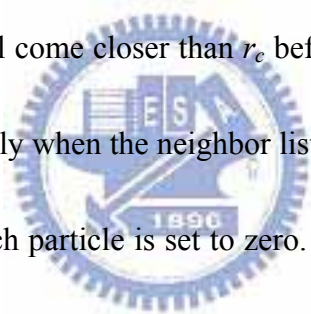
2.5.2.2 Cell link + Verlet list

we could combine cell link method and Verlet list method, see Fig. 2.7 ;by this

way ,it could promote the performance of the simulation.

2.6 Equation of motion

2.6.1 Leap-Frog method

Leapfrog method is completely equivalent algebraically and yield coordinates

that are accurate to third order in Δt. However, it tends to be considerably better than the higher-order methods from the viewpoint of energy conservation. In addition, their storage requirements are also minimal.

The derivation of the Verlet formula follow simmediately from the Taylor expansion of the coordinate variable – typically *x(t)*

$$x(t+h) = x(t) + h\dot{x}(t) + (h^2/2)\ddot{x}(t) + O(h^3) \tag{2.21}$$

where t is the current time , and $h \equiv \Delta t$. Here, $\dot{x}(t)$ is the velocity component, and $\ddot{x}(t)$ the acceleration –or force *f(t)* in reduced MD units. Note that although $\ddot{x}(t)$ has been expressed as a function of *t*, it is actually a known function – via the force law – of the coordinates at time *t*. After rearrange Eq.2.21, we obtain

$$x(t+h) = 2x(t) - x(t-h) + h^2\ddot{x}(t) + O(h^4) \tag{2.22}$$

The truncation error is of order $O(h^4)$ because the h^3 term cancel. A possible disadvantage of Eq. 2.22 is that at low machine precision the h^2 term multiplying the acceleration may prove a source of inaccuracy. The velocity is not directly involved in the solution, but if required it can be obtained from

$$\dot{x}(t) = [x(t+h) - x(t-h)]/2h + O(h^2) \tag{2.23}$$

with higher-order expression based on values from earlier time steps available if needed, though rarely used.

The leapfrog method is equally simple to derive. Rewrite the Taylor expansion as

$$x(t+h) = x(t) + h[\dot{x}(t) + (h/2)\ddot{x}(t)] + O(h^3) \tag{2.24}$$

The term multiplying h is just $\dot{x}(t+h/2)$, so Eq.2.24 becomes 2.26 below.

The leapfrog integration formulate are then

$$\dot{x}(t+h/2) = \dot{x}(t-h/2) + h\ddot{x}(t) \tag{2.25}$$

$$x(t+h) = x(t) + h\dot{x}(t+h/2) \tag{2.26}$$

The fact that coordinates and velocities are evaluated at different times dose not present a problem; if an estimate for $\dot{x}(t)$ is required there is a simple connection that can be expressed in either of two ways:

$$\dot{x}(t) = \dot{x}(t \mp h/2) \pm (h/2)\ddot{x}(t) \tag{2.27}$$

The initial conditions can be handled in a similar manner, although a minor inaccuracy in describing the starting state, namely, the distinction between $\dot{x}(0)$ and $\dot{x}(h/2)$, is often ignored.
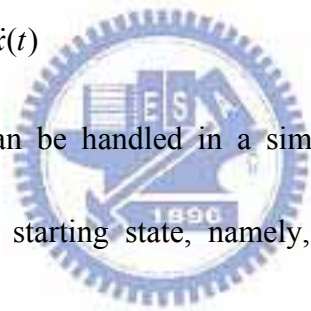
2.6.2 Gear's predictor method

Predictor-corrector algorithms commonly used in molecular dynamics are often taken from the collection of methods devised by Gear. Predict molecular position r_i a time $t + \Delta t$ using a fifth-order Taylor series based on positions and their derivatives at time t:

$$r(t+\Delta t) = r_i(t) + \dot{r}_i(t)\Delta t + \ddot{r}_i(t)\frac{(\Delta t)^2}{2!} + r_i^{(iii)}(t)\frac{(\Delta t)^3}{3!} + r_i^{(iv)}(t)\frac{(\Delta t)^4}{4!} + r_i^{(v)}\frac{(\Delta t)^5}{5!} \tag{2.28}$$

$$\dot{r}(t+\Delta t) = \dot{r}_i(t)\Delta t + \ddot{r}_i(t)\Delta t + r_i^{(iii)}(t)\frac{(\Delta t)^2}{2!} + r_i^{(iv)}(t)\frac{(\Delta t)^3}{3!} + r_i^{(v)}\frac{(\Delta t)^4}{4!} \tag{2.29}$$

$$\ddot{r}(t+\Delta t) = \ddot{r}_i(t) + r_i^{(iii)}(t)\Delta t + r_i^{(iv)}(t)\frac{(\Delta t)^2}{2!} + r_i^{(v)}\frac{(\Delta t)^3}{3!} \tag{2.30}$$

$$r^{(iii)}(t+\Delta t) = r_i^{(iii)}(t) + r_i^{(iv)}(t)\Delta t + r_i^{(v)}\frac{(\Delta t)^2}{2!} \tag{2.31}$$

$$r^{(iv)}(t+\Delta t) = r_i^{(iv)}(t) + r_i^{(v)}\Delta t \tag{2.32}$$

$$r^{(v)}(t+\Delta t) = r_i^{(v)}(t) \tag{2.33}$$

$$\Delta\ddot{r}_i = \left[\ddot{r}_i(t+\Delta t) - \ddot{r}_i^{P}(t+\Delta t)\right] \tag{2.34}$$

In Gear's algorithms for second-order differential equations, this difference term

is used to correct all predicted positions and their derivatives; thus,

$$r_i = r_i^{P} + \alpha_0\Delta R2 \tag{2.35}$$

$$\dot{r}_i\Delta t = \dot{r}_i^{P}\Delta t + \alpha_1\Delta R2 \tag{2.36}$$

$$\frac{\ddot{r}_i(\Delta t)^2}{2!} = \frac{\ddot{r}_i^{P}(\Delta t)^2}{2!} + \alpha_2\Delta R2 \tag{2.37}$$

$$\frac{r_i^{(iii)}(\Delta t)^3}{3!} = \frac{r_i^{(iii)P}(\Delta t)^3}{3!} + \alpha_3\Delta R2 \tag{2.38}$$

$$\frac{r_i^{(iv)}(\Delta t)^4}{4!} = \frac{r_i^{(iv)P}(\Delta t)^4}{4!} + \alpha_4\Delta R2 \tag{2.39}$$

$$\frac{r_i^{(v)}(\Delta t)^5}{5!} = \frac{r_i^{(v)P}(\Delta t)^5}{5!} + \alpha_5\Delta R2 \tag{2.40}$$

$$\text{where} \quad \Delta R2 = \frac{\Delta\ddot{r}_i(\Delta t)^2}{2!} \tag{2.41}$$

$\alpha_0 = 3/16, \quad \alpha_1 = 251/360, \quad \alpha_2 = 1, \quad \alpha_3 = 11/18, \quad \alpha_4 = 1/6, \quad \alpha_5 = 1/60$

2.7 Thermodynamic properties

Measurements of thermodynamic equilibrium properties can be considered as

exercises in numerical statistical mechanics. MD simulation provides an alternative to

Monte Carlo (MC) simulation, and if no further information is required about the

system, computational efficiency alone should determine the choice of simulation

technique.

2.7.1 Absolute temperature

For an isolated system the total internal energy E is just the Hamiltonian ,which
divides into a Kinetic part E_k and a configurational part U_c.

$$E = E_k + U_c \tag{2.42}$$

$$\frac{U_c}{N} = 2\pi\rho \int_0^\infty u(r)g(r)r^2 dr \tag{2.43}$$

The average Kinetic energy is proportional to the absolute temperature:

$$< E_k > = \frac{3}{2}NKT \tag{2.44}$$

by Eq.2.44 so we could get the absolute temperature

Estimation of C_v:

$$C_v = \frac{N_a}{k_B T^2} < \delta E^2 > \tag{2.45}$$

where $< \delta E^2 > = < E^2 > - < E >^2$. However, this is inappropriate for the
microcanonical (NVE) MD simulation since E=constant. Instead, it can be
shown that, using the variance of E_k or E_u,

$$C_v = \frac{3k_B}{2}(1 - \frac{2N_a}{3(k_B T)^2} < \delta E_k^2 >)^{-1} \tag{2.46}$$

2.7.2 Pressure

Pressure is obtained from the virial expression as shown below:

$$PV = NT + \frac{1}{d}\left\langle \sum_{i=1}^{N} r_i \cdot F_i \right\rangle \tag{2.47}$$

2.8 Data analysis method

We using the several methods to analysis the data which generated by MD simulation, in order to understand the behaviors and nature of droplet after collisions. Such as *Evaporate rate*, *Fragment distribution*, *Surface increased ratio* and *Energy transfer process*.

2.8.1 Size distribution

The fragment distribution was analyzed at the end of each simulation. Clearly, fragmentation depends strongly on the collision energy and the impact parameter. We define the fragment clusters is follow Stillinger [1963]. We identify a cluster if the distance between two atoms is less 2.5 . There is a Verlet-list in previous chapter. So we can identify the cluster in the space by the Verlet-list.

2.8.2 Evaporation rate

In current study, we perform a lot of droplet pair collisions cases under vacuum and with different ambient gas pressures. Since the evaporate rate is maybe an important parameter of our simulation. We can identify the cluster in previous chapter. While the collisions energy is relative low the droplet pair will coalescence become to a big cluster. At the same time the cluster evaporated effect is still going on. The evaporate rate can obtains from calculate the number of atoms of the cluster step by

step.

2.8.3 Energy transfer process

The kinetic energy of collision (*CKE*) will be transferred to the rotational and vibrational energies after droplet impact. For the fragment with N atoms after droplets collisions, the instantaneous rotational was obtained as

$$E_{rot} = \frac{1}{2}\omega \cdot L \qquad (2.48)$$

where L is the angular momentum with respect to the center of mass of the fragment and ω is the corresponding angular velocity [3]. The instantaneous rotational energy varies rather smoothly with time because the overall shape of the largest fragment usually do not change rapidly. The instantaneous vibrational energy of fragment with N atoms was obtained as

$$E_{v,k} = \sum_{1}^{N} E_{v,k,i} = \frac{1}{2}m\left[\left(\frac{p_{x,i}}{m} - v_{rot,x,i}\right)^2 + \left(\frac{p_{y,i}}{m} - v_{rot,y,i}\right)^2 + \left(\frac{p_{z,i}}{m} - v_{rot,z,i}\right)^2\right] \qquad (2.49)$$

where $E_{v,k,i}$ is the vibrational kinetic energy, p_i is the momentum and $v_{rot,i}$ is angular velocities of i-th atom. And the vibrational kinetic temperature of the fragment was obtained as

$$T_{vib} = 2E_{v,k}\Big/(3N-6)k_B \qquad (2.50)$$

where k_B is the Boltzmann's constant.

2.8.4 Surface tension

The cohesive forces between liquid molecules are responsible for the

phenomenon as known as the surface tensions. The molecules at the surface do not have other like molecules on all sides of them and consequently they cohere more strongly to those directly associated with them on the surface. This forms a surface "film" which makes it more difficult to move an object through the surface than to move it when it is completely submersed. The surface tension is typically measured in dynes/cm, the force in dynes required to break a film of length 1 cm. And it can be stated as surface energy in ergs per square centimeter. Water at 20°C has a surface tension of 72.8 dynes/cm and Argon at 84°K has a surface tension of 13.45 dynes/cm via experiment. In current study, the surface tension computation is based on molecular interpretation presented by Tabor [1991].
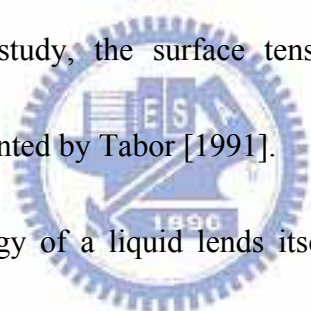
"The free surface energy of a liquid lends itself to a very simple molecular interpretation. Molecular in the bulk are subjected to attraction by surrounding molecular; the field is symmetrical and has no net effect. At the surface, however, the surface molecules are pulled in towards the bulk of the liquid. Apart from a few vapor molecules there is no attraction in the opposite direction. Consequently if we wish to increase the area we have to pull molecules up to the surface from the bulk against this one-sided attraction. This accounts for surface energy." Tabor [1991]

The concept is shown in Fig 2.8. The pull forces within interior of the droplet or vaporized atoms are balanced. Only the atoms on the surface, where a density

gradient exits, will generate a net force on the atoms on the surface. The pulling

against this force when expanding the surface is the surface energy described by

Tabor.

2.9 Summary

In this chapter has presented an overview of classical Molecular Dynamic

simulation process in brief. The first part (Section 2.1~2.6) of this chapter was

concerned with the general description of standard MD simulation. The second part

(Section 2.7~2.8) of this chapter introduced the measurement properties in MD

simulation and we will adopt data analysis method in current study.
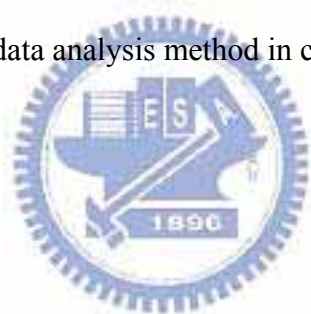
Chapter 3 Parallel Cellular Molecular Dynamics (PCMD) Simulation Method

3.1 Reviews of parallel molecular dynamics method

There is no doubt about that MD simulation is a useful and valuable tool. But MD simulation is very time-consuming due to large number of time steps and possibly large number of atoms required to complete a meaningful simulation. In liquids and solids, MD simulation is required to resolve the vibration of the atoms, which limits the time step to be on the order of fentosecond. Many hundreds of thousand or even millions of time steps are needed to simulate a nanosecond in "real" time scale. In addition, up to hundreds of thousand or millions of atoms are needed in the MD simulation, even for a system size in the nanometer scale..
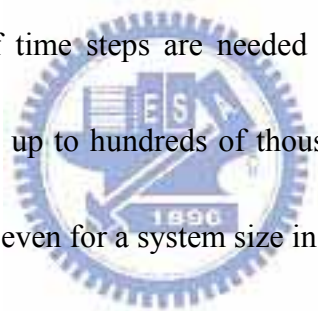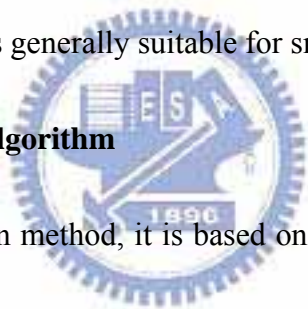
In the past, there have been considerable effort [Plimpton, 1995] that concentrated on parallelizing MD simulation on the memory-distributed machine by taking the inherently parallelism e.g., Boghosian [1990], Fox [1998]. Generally, parallel implementation of the MD method can be divided into three categories, including the atom decomposition, the force decomposition and the spatial decomposition among processors [Plimpton, 1995].

3.1.1 Atomic–decomposition algorithm

In the atom decomposition method, each processor, which owns nearly the same

number of atoms as other processors and in which atoms are not necessarily geometrically nearby, integrates the Newton's equation for all atoms and moves the atoms of their owns. However, this method requires global communication at each time step, which becomes unacceptably expensive as compared with the "useful" MD computation when the number of atoms increases to a certain amount, since each processor has to know all information (position and velocities) of all atoms at each time step. Or equivalently, the communication is $O(N)$, where N is the number of atoms in the system that is independent of the number of the processors, P. Thus, the atom decomposition method is generally suitable for small-scale problem

3.1.2 Force–decomposition algorithm

In the force decomposition method, it is based on a block-decomposition of the force matrix rather than a row-wise decomposition in the atom-decomposition method. It improves the $O(N)$ scaling to be $O(N/\sqrt{P})$. It generally performs much better that the atom decomposition method; however, there exists some disadvantages. First, the number of processors has to be square of an integer. Second, load imbalance may become an issue. From previous experience [Plimpton, 1995], it is suitable for small- and intermediate-size problems.

3.1.3 Spatial–decomposition algorithm

In the spatially static domain decomposition method, simulation domains are

physically divided and distributed among processors. This method so far represents

the best parallel algorithm for large-scale problem in MD simulation for short-ranged

interaction [Karypi *et. al.*, 1998]; however, it only works well for a system, in which

the atoms move only a very short distance during simulation or possibly distribute

uniformly in space. MD simulation of solids represents one of the typical examples. In

contrast, if the distribution of the atoms tends to vary very often in the configuration

space, then the load imbalance among processors develops very fast during simulation,

which detriments the parallel performance. Thus, a parallel MD method capable of

adaptive domain decomposition may represent a better solution for resolving this

difficulty.
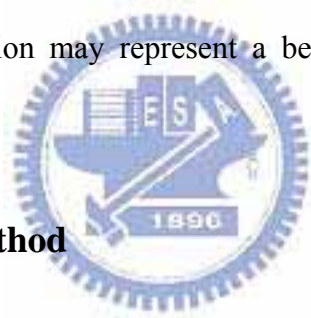
3.2 Proposed PCMD method

3.2.1 Basic algorithm

A new parallel algorithm for MD simulation, named parallel cellular molecular

dynamics (PCMD), is developed by MuST (Multiscale Science & Technology)

laboratory in NCTU in Taiwan, employing dynamic domain decomposition to

address the issue of load imbalance among processors in the spatially static

domain-decomposition method. We focus on developing a parallel MD method

using dynamic domain decomposition by taking advantage of the existing link-cells

as mentioned earlier. In this proposed method, not only are the cells used to reduce

the cost for building up neighbor list, but also are used to serve as the basic partitioning units. Similar idea has been applied in the parallel implementation of direct simulation Monte Carlo (DSMC) method [Nicol *et. al.*, 1988], which is a particle simulation technique often used in rarefied gas dynamics. Note that in the following IPB stands for interprocessor boundary. General procedures (Fig. 3.1) in sequence include:

1. initialize the positions and velocities of all atoms and equally distribute the atoms among processors;

2. Check if load balancing is required. If required, then first repartition the domain, followed by communicate cell/atom data between processors, renumber the local cell and atom numbers, and update the neighbor list for each atom due to the data migration;

3. Receive positions and velocities of other atoms in the neighbor list for all cells near the IPB;

4. Compute force for all atoms;

5. Send force data to other atoms in the neighbor list for all cells near the IPB;

6. Integrate the acceleration to update positions and velocities for all atoms;

7. Apply boundary conditions to correct the particle positions if necessary;

8. Check if preset total runtime is exceeded. If exceeded, then output the data and stop the simulation. If not, check if it is necessary to rebuild the neighbor list of all atoms using the most update atom information.

9. If it is necessary to rebuild the neighbor list ($N=8$ in the current study), then communicate atom data near the IPB and repeated the steps 2-8. If not necessary, then repeat steps 3-8.

In the above, in addition to the necessary data communication when atoms cross the IPB and particle/cell data near the IPB, there are two more important steps in the proposed parallel MD method as compared with the serial MD implementation. One is how to repartition the domain effectively and the other is the decision policy for repartitioning. These two steps are described next, respectively.

3.2.2 Repartitioning scheme

Under the framework of graph theory, centers of each link-cell are considered as the *vertices* and the lines connecting them are considered as *edges*. Each vertex and edge can be assigned with weight for the purpose of partitioning. Graph partition has been found very useful for unstructured mesh in computing community in the past. In the current study, a parallel multilevel graph-partitioning runtime library, *PMETIS*

[Karypi *et. al*., 1998], is used as the repartitioning tool in our PCMD code. Thus, the

data structure of the link-cell is reconfigured as unstructured for graph-partitioning

purpose. Multilevel graph partitioning scheme uses the multilevel implementation

that matches and combines pairs of adjacent vertices to define a new graph and

recursively iterate this procedure until the graph size falls under some threshold. The

coarsest graph is then partitioned and the partition is successively refined on all the

graphs starting with the coarsest and ending with the original. At evolution of levels,

the final partition of the coarser graph is used to give the initial partition for the next

finer level. A corresponding parallel version, *PMETIS* [Karypi *et. al*., 1998], uses an

iterative optimization technique known as relative gain optimization, which both

balances the workload and attempts to minimize the inter-processor communication

overhead.
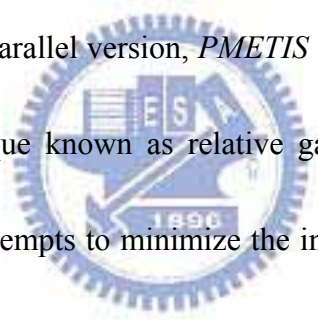
This parallel multilevel graph partition runs on single program multiple data

(*SPMD*) paradigm with message passing in the expectation that the underlying mesh

will do the same. Each processor is assigned to a physical sub-domain and stores a

double-linked list of the vertices within that sub-domain. However, each processor

also maintains a "halo" of neighboring vertices in other sub-domains. For the serial

version, the migration of vertices simply involves transferring data from one

linked-list to another. In parallel version, this process is far more complicated than

just migrating vertices. The newly created halo vertices must be packed into messages as well, sent off to the destination processor, unpacked, and the pointer based data structure recreated there. This provides a possible solution to the problem of adaptive load balancing [Karypi *et*. *al*., 1998].

3.2.3 Decision policy for repartitioning

MD represents a typical dynamic (or adaptive) irregular problem, i.e., the workload distributions are known only at runtime, and can change dramatically as simulation proceeds, leading to a high degree of load imbalance among the processors. This load-changing situation is even obvious in simulating liquids or gases. Thus, the partitioning runtime library, *PMETIS* [Karypi *et*. *al*., 1998], described in the above is used to repartition the mesh based on some sort of decision policy. In the direct simulation Monte Carlo (DSMC) simulation [J.-S. and K.-C., 2002], it has been shown that a decision policy based on stop at rise (SAR) [Nicol *et*. *al*., 1988] works well for improving the parallel performance. However, from our preliminary study, it does not work very well in the MD simulation since the domain repartition is too often and, thus, too costly in practice. In addition, the data locality of the MD simulation using link-cells is lower than that of the DSMC simulation, which only considers collision (interaction) among atoms within the same cell. Instead, a simple threshold-like decision policy, termed as "simple threshold

scheme" (STS), is designed to decide the proper time to repartition. This scheme simply asks for domain repartitioning if the workload in some processor is detected over the specified threshold (e.g., ±20% of the average workload). Number of atoms in each link-cell is used as the weighting for graph partitioning. Right after the repartition, the communication between geometrically neighboring processors is required to transfer the cell number and particle data to the destination processor, followed by renumbering of the cell and particle data into the local numbering in the destination processor. Since all processors know the geometrical information of all cells, the renumbering of the received cells in some specific processor is done simply by adding up sequentially the local cell number for the new cell. Similarly, the cells sent out to other processors are simply removed sequentially by copying the information of the final cell onto the memory of the sent cells. This decision policy for repartitioning the domain is inherently advantageous in which no prior knowledge of the evolution of the problem is necessary to determine the repartitioning interval, and the repartitioning can be expected to follow the dynamics of the problem.

Current PCMD code is implemented on a 64-bit Itanium PC-cluster system running Linux OS at National Center for High-performance Computing in Taiwan (64-node, dual processor and 4GB RAM per node). Standard message-passing

interface (MPI) is used for data communication. It is thus expected that the current

PCMD code should be highly portable among the memory-distributed parallel

machines that is running with Linux (or equivalent) operating system.

3.2.4 Simulation conditions

There are three test problems we using to test the performance of PCMD code,

including L-J (12, 6) atoms in condensed, vaporized and supercritical states, are

chosen to test the current parallel implementation of the molecular dynamics

simulation. Related simulation conditions are summarized in Table 2. Densities

($\rho^* = N\sigma^3/V$) are all taken to be 0.7 for convenience, while temperatures

($T^* = kT/\varepsilon$) are varied to represent different states. Note that the number of cells in

Table 2 represents the number of link-cells used for simulation. Note that the

simulation volume is generally much larger (~10 times) than the initial volume of

FCC-arranged atomic structure near the system center, except the case of

supercritical state, which simulation volume is approximately the same as the initial

FCC volume. Each atom of an initially FCC-arranged atomic structure is given

random velocities based on the desired temperature and starts to run for 10^5 time

steps. Rescaling the kinetic energy of the system during runtime enforces the desired

temperature of the simulation system for all three test cases. Simulation time step is

0.005 dimensionless MD time scale (or about 0.005*10 *fs*). Current test problems

represent a more severe test to the parallel implementation of MD method due to the

rapidly changing workload among processors during the simulation. For example, it

is rather difficult to parallel compute the condensed state efficiently if conventional

parallel paradigm such as static domain decomposition is used. All results presented

below obtained using 25 processors, unless otherwise specified. In addition, periodic

boundary conditions are used to simplify the analysis in the current study.

3.2.5 Parallel performance

Figs. 3.2(a), Figs. 3.2(b) and Figs. 3.2(c) show the domain decompositions

(initial and final) for the condensed, vaporized and supercritical states, respectively,

on the system surface and on some special cross sections cutting through the system

center. By comparing these figures, we can find that the domain decomposition

changes to a large extent from the initial to the final state, except the case of

supercritical state, in which the initial FCC structure almost occupies the simulation

volume. In Fig. 3.2(a) (condensed state), the domain size near the center the system

center is very small as compared with the domain size in other regions since the

atoms are clustered near the system center. In contrast, the distribution of the domain

size is relatively uniform in Fig. 3.2(b) (vaporized state) in the simulation volume

since the atoms are spreading randomly in the computational domain. Fig. 3.2(c)

shows the domain decomposition of the supercritical state, in which the distribution

of domain is similar to the vaporized state (Fig. 3.2(b)) but with higher ordered

structure. The above arguments about the evolution of domain decomposition in the

test cases, along with the time-dependent distributions of number of atoms in each

processor, can explain the parallel performance obtained in the current study, which

are introduced next.

Fig. 3.4 shows the corresponding parallel speedup for all three test cases (up to

49 processors) in the current study along with the ideal speedup (dotted line). Using

49 processors, the parallel speedup is 32 (~65% parallel efficiency) for the

supercritical-state case and 28 (~57% parallel efficiency) for the condensed-state

case, while it is 17 (or 35% parallel efficiency) for the vaporized-state case. Note

that the above parallel speedup/efficiency are all computed assuming the value of

speedup as two for two processors. It is attributed to the too frequent repartition of

the domain in the vaporized-state case, although slightly better load balancing is

observed than other two cases (Fig. 3.3.(b)). This could further deteriorate the

speedup due to the rapid increase of the frequent communication required for

repartition the domain, in addition to the large number of processors. This can be

shown by the increase of speedup to 21 (49 processors) if we do not repartition the

domain after the thermal equilibration period (~30,000 time steps). Using the current

parallel implementation of the MD code, approximately 70-80% of parallel

efficiency can be achieved at 25 processors, which may be most accessible for researchers from a practical PC-cluster system.

In the PCMD study, a parallel molecular dynamics simulation for short-ranged interactions using dynamic domain decomposition is developed for the large-scale problem on the memory-distributed PC-cluster system, which uses MPI as the communication protocol. In the method, a multi-level graph-partitioning scheme is used to dynamically re-decompose the computational domain based on a simple threshold scheme (STS), which is expected to keep the number of atoms in each processor within the range of the threshold values. Parallel performance of the current parallel MD method is studied using three different test cases, including the condensed, vaporized and supercritical states, using approximately one million L-J atoms, which all are initialized from a FCC atomic structure. Results show that fairly good parallel efficiency in the range of 40-65% using 49 processors can be achieved for the three test cases, otherwise very low if static domain decomposition or other methods are employed.

3.2.6 Summary

The first part of chapter introduced several algorithms of Parallel Molecular Dynamic simulation process in brief. Then we propose our new algorithms of parallelized MD simulation, named "PCMD". End of this chapter, we test the PCMD

code on a 64-bit Itanium PC-cluster system running Linux OS at National Center for

High-performance Computing in Taiwan (64-node, dual processor and 4GB RAM per

node).

Chapter 4 Simulation of argon droplet-droplet collision dynamics

4.1 Simulation conditions

We perform a lot of test cases of droplet pair collision under vacuum, low pressurized ambient (~0.055 atm) and high pressurized ambient (~0.55 atm), respectively. To check out the influence of crucial parameter impact parameter (*b*) and Weber number which depends on the relative velocity between droplet pair. The diameter of droplet is ~105Å which contain ten thousand atoms. And we copy the droplet relative coordinate to make the other droplet in different center of droplet in space. And give a opposite initial velocity to droplet pair, respectively. The pressurized ambient is made by 4 thousand atoms of low pressurized (~0.055 atm) case and 40 thousand atoms of high pressurized (~0.55 atm) case, then equilibrium at 216K during a hundred thousand time steps ensure which is vapor state. The non-head-on collision cases (Fig. 3.4) system dimension is 600σ*300σ*300σ for to check out the droplet pair behavior more clear. The head-on collision cases (Fig. 3.3) dimension is 200σ*500σ*500σ, because the "disruption" or the "fragmentation" of head-on collision is more clear on Y-Z plane. At last, we applied the PBC condition in each direction only on ambient gas atoms.

4.1.1 Droplet formation

We make the droplet follow general MD pre-process . First we arranged the L-J

potential atoms (single atoms) by FCC crystal structure in center of system, which the

local density of FCC structure is 0.7 and equilibrium at 84K during a hundred

thousand time steps, then to abandon the vaporized atoms of droplet. Then we get the

droplet of L-J atom which contains ten thousand. Before we setup the droplet pair by

copy the droplet relative coordinate, we tested the droplet pair collision in different

relative angle, make sure the droplet unit is in liquid state, the structure of droplet will

not effect the droplet pair behaviors after collision.

4.1.2 Background gas formation

As the droplet formation, first we arranged the atoms by FCC crystal structure in

center of system, then we configure the system domain is $600\sigma*300\sigma*300\sigma$ for

non-head on case and $200\sigma*500\sigma*500\sigma$ for head on case. We setup the local density

of FCC structure is 0.2 and equilibrium at 216K during a hundred thousand time steps.

In the low pressurized ambient condition, the head on cases domain contains 3700 gas

atoms and the non-head on cases domain contains 4000 gas atoms. In the High

pressurized ambient condition, the head on cases domain contains 37000 gas atoms

and the non-head on cases domain contains 40000 gas atoms. Final, we configure the

droplet pair collision by abandoned the gas atoms in droplet pair initial positions area.

4.1.2 Test conditions

We perform a lot of cases under several conditions and for several subjects (Fig. 4.1~Fig. 4.3). So we to describe the test conditions of *head-on cases*, *non-head on cases* and *bounce cases*, respectively.

In head-on cases (Fig. 4.5), we simulate the droplet collisions with different relative velocities (V=100~1500 m/s) and the impact parameter is fixed at 1 (the distance between center of droplet pair in Y-direction=0.). Because the droplet pair "disruption" and "fragmentation" behaviors of head-on cases only occur with high relative velocities, so the collisions velocities range is widest in current study. The distance between center of droplet pair is ~140 Å in X-direction at initial.

In non-head-on cases (Fig. 4.6), we simulate the droplet collisions with different relative velocities (V=100~1375 m/s) and the impact parameter is varies form 0.875~0.25. As the head-on cases, we setup distance between center of droplet pair is ~140 Å in X-direction at initial.

In bounce cases, we simulate the droplet collisions with different relative velocities (V=10~30 m/s) and the impact parameter is fixed at 1. Because the droplet pair "bounce" behavior of head-on cases only occur within the low and narrow relative velocities range, so we must extend the simulation time until the bounce occurs. We extend the distance between centers of droplet pair form ~140 Å to ~204

Å in X-direction at initial, for observed the bounce behavior clearly and easily.

For identify the droplet pair behavior easily and in objectivity, we classify each collision behavior in following manner [Svanberg *et. al*., 1998]:

i. Coalescence: The largest fragment contains > 80% of the molecules.

ii. Stretching Coalescence: The largest fragment contains > 80% of the molecules, the droplet shape transform form a ball to a rotational bar, and never breakup.

iii. Stretching Separation: The largest fragment contains < 60%, while the sum of the two largest fragments consists of > 90% of the molecules.

iv. Shattering: The largest fragment contains < 40%, and the sum of the two largest fragments consists of < 65% of the molecules.

v. Bounce: The droplet pair is never touch each other in simulation, while the two largest fragments consists of > 80% of the molecules.
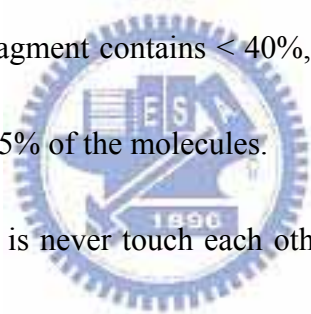
4.2 Results and discussion

Evaporation rate

At the first, we structured the different ambient conditions, is vacuum, low pressurized (~0.055 atm) and high pressurized (~0.55 atm), respectively. The Fig. 4.4 is the evaporation rate function of time-step under different ambient conditions using coalescence cases (b=0.75, V=250 *m/s*). In this Figure, we can clearly find out the evaporation rate of 0.55atm case is much less then others cases. The evaporation rate curve of 0.055atm case is almost the same the vacuum one, but in serious the

evaporation rate under vacuum is still bigger then others. This effect the different conditions has different regime maps. Therefore we can find out the stretching coalescence collisions for the first time.

4.2.1 Droplet-droplet collision under vacuum environment

The Fig. 4.7~Fig. 4.9 is the snapshots of the head-on (b=0) droplet pair collision under vacuum environment with different initial velocity (V= 1250, 1375 and 1500 *m/s*). In Fig. 4.7, (V=1250 *m/s*), we can find out the droplet area is increase as the beginning and then the area is decrease depends on the time-steps with a few droplet fragmentation. In Fig. 4.8, (V=1375 *m/s*), we can see the droplet area is increase as the beginning and then the area ruptures to a "ring", at last the ring become a droplet again. In Fig. 4.9, (V=1500 *m/s*), we can see the droplet area is increase as the beginning and then the area ruptures to a "net", at last the "net" fragment into several small droplets.
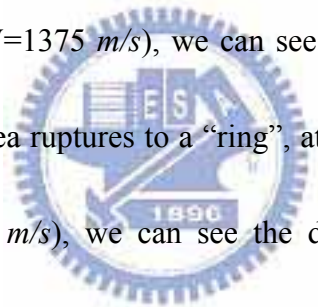
The Fig. 4.16~Fig. 4.18 is the snapshots of the non-head-on droplet pair collision under vacuum environment with different initial velocity and different impact parameter.

The collision behavior of Fig. 4.16 (b=0.25, V=250 *m/s*) is be classified in coalescence regime. In this case, the droplet pair move slowly and coalescence become a rotating "bigger" droplet which mass is almost equal the sum of droplet pair

mass. The Fig. 4.37(a) is the number of atoms of the largest fragment. We can find out the number of atoms is became double of one droplet, because this is a coalescence case. Then the number of atoms is decreased function of time, because the droplet evaporation is occurring with time increasing. The Fig. 4.37(b) is the vibrational temperature of atoms of the largest fragment, we find out the temperature rapidly increased when the droplet pair occur impact. After the droplet impact the temperature is cold down during time at 40~80ps, at this time the impact energy is completed has been transferred into temperature energy and complete the thermo-equilibrium inside the droplet. After 90ps, the temperature is increased with time, because the droplet evaporation is pulling the atoms from droplet surface. The Fig. 4.37(c) is the rotational energy of the largest fragment, we find out the rotational energy rapidly increased, because the initial relative translation contributed to rotational energy. And the Fig. 4.37(d) is the angular momentum of the largest fragment in different directions.

The collision behavior of Fig. 4.17 (b=0.625, V=1000 *m/s*) is be classified in stretching separation regime. In this case, the droplet pair disrupted into 2 droplets and 2 "satellite" droplets follow long a narrow tail. The Fig. 4.38(a) is the number of atoms of the largest fragment. At the first, the number of atoms is became double of one droplet, then the droplet separation in two main droplet, when the time at near

100ps the largest fragment to meet the 2nd separation, because the trail breakup. At final stage the number of fragment is decreasing by evaporation effect. The Fig. 4.38(b) is the vibrational temperature of atoms of the largest fragment, we find out the temperature rapidly increased when the droplet pair occur impact. After the droplet impact the temperature rapidly fall off during 7~10ps, then the temperature raise up until ~50ps, then the temperature rapidly fall off again when separation occurred. The Fig. 4.38(c) is the rotational energy of the largest fragment, we find out the rotational energy rapidly increased, because the initial relative translation contributed to rotational energy. During 15~100ps the rotational energy decreased function of time, because the largest fragment be stretching, then the energy rapidly fall off when separation occur. And the Fig. 4.38(d) is the angular momentum of the largest fragment in different directions.
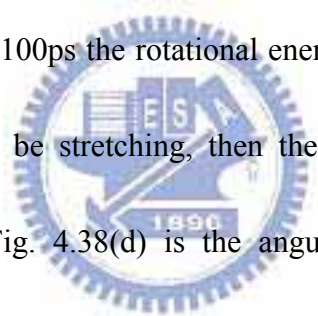
The collision behavior of Fig. 4.18 (b=0.25, V=1375 *m/s*) is be classified in shattering separation regime. In this case, the droplet pair to meet huge impact kinetic energy, the droplet fragments into over 5 droplets. The Fig. 4.39(a) is the number of atoms of the largest fragment. At the first, the number of atoms is became double of one droplet, then the largest fragment to meet twice serious fragmentation, during the process the number of fragment is decreased serious than other cases. The Fig. 4.39(b) is the vibrational temperature of atoms of the largest fragment, we find out the

temperature rapidly increased when the droplet pair occur impact, and the peak value

of the temperature is higher than others. Then the temperature fall off rapidly when

separation occurred at 70ps. The Fig. 4.39(c) is the rotational energy of the largest

fragment, we find out the rotational energy rapidly increased, because the initial

relative translation contributed to rotational energy. During 15~60ps the rotational

energy decreased function of time, because the largest fragment be stretching, then the

energy rapidly fall off twice when fragmentations occur. And the Fig. 4.39(d) is the

angular momentum of the largest fragment in different directions.

4.2.2 Droplet-droplet collision under low pressurized ambient

Under this condition, we find out the stretching coalescence for the first time.

But unfortunately, we do not capture any droplet pair bouncing under this condition.

The Fig. 4.10~Fig. 4.12 is the snapshots of the head-on (b=0) droplet pair

collision under low pressurized ambient with different initial velocity (V= 1250, 1375

and 1500 m/s). In Fig. 4.10, (V=1250 m/s), we can see the droplet area is increase as

the beginning and then the area ruptures to a "ring", at last the ring become a droplet

again. In Fig. 4.11, (V=1375 m/s), we can see the droplet area is increase as the

beginning and then the area ruptures to a "net", at last the "net" fragment into several

bigger droplets. In Fig. 4.12, (V=1500 m/s), we can see the droplet area is increase as

the beginning and then the area ruptures to a "net", at last the "net" fragment into

several small droplets. The fragmented droplets size is still bigger than the droplets of

simulation of the same condition under vacuum. Because, there are less atoms be

vaporized under low pressurized (~0.055 atm) ambient

The Fig. 4.19~Fig. 4.22 is the snapshots of the non-head-on droplet pair collision

under low pressurized ambient (~0.055 atm) with different initial velocity and

different impact parameter.

The collision behavior of Fig. 4.19 (b=0.25, V=250 *m/s*) is be classified in

coalescence regime. In this case, the droplet pair move slowly and coalescence

become a rotating "bigger" droplet which mass is almost equal the sum of droplet pair

mass, as the same conditions under vacuum. The Fig. 4.40(a) is the number of atoms

of the largest fragment. We can find out the number of atoms is became double of one

droplet, because this is a coalescence case. Then the number of atoms is decreased

function of time, because the droplet evaporation is occurring with time increasing.
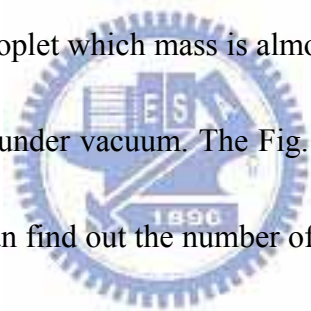
The Fig. 4.40(b) is the vibrational temperature of atoms of the largest fragment, we

find out the temperature rapidly increased when the droplet pair occur impact. After

the droplet impact the temperature is cold down during time at 100~250ps, at this time

the impact energy is completed has been transferred into temperature energy and

complete the thermo-equilibrium inside the droplet. After 250ps, the temperature is

increased with time, because the droplet evaporation is pulling the atoms from droplet

surface. The Fig. 4.46(c) is the rotational energy of the largest fragment, we find out the rotational energy rapidly increased, because the initial relative translation contributed to rotational energy. And the Fig. 4.40(d) is the angular momentum of the largest fragment in different directions. In this case, the Fig. 4.40 is almost the same with Fig. 4.37. Because the relative velocity is too small, in this case we can't find out the pressurized ambient effect.

The collision behavior of Fig.4.20 (b=0.25, V=750 *m/s*) is be classified in stretching coalescence regime. In this case, the droplet be stretched and rotated during the process, at final stage, the droplet become into a rotating ball, and there no breakup occur. The Fig. 4.41(a) is the number of atoms of the largest fragment. In this figure, we can clearly classified this is a coalescence case. But there two stage of vaporized rate and the vaporized effect is clearly stronger than typical coalescence case. Because the droplet be stretched, the surface of droplet is bigger than a coalescence droplet. The Fig. 4.41(b) is the vibrational temperature of atoms of the largest fragment, we find out the temperature rapidly increased when the droplet pair occur impact. After the droplet impact the temperature rapidly fall off during 7~10ps. The Fig. 4.41(c) is the rotational energy of the largest fragment, we find out the rotational energy rapidly increased, because the initial relative translation contributed to rotational energy. During the process the rotational energy decreased function of
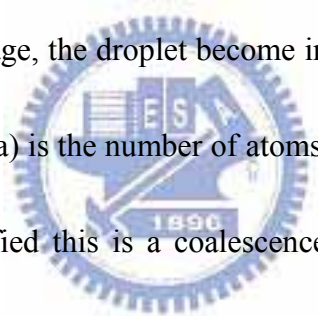
time, because the largest fragment be stretched. The energy never falls off rapidly, and value is ten times of coalescence case, it show clear that the droplet is rotating with out of shape. And the Fig. 4.41(d) is the angular momentum of the largest fragment in different directions.

The collision behavior of Fig. 4.21 (b=0.625, V=1000 *m/s*) is be classified in stretching separation regime. In this case, the droplet pair disrupted into 2 droplets and several "satellite" droplets follow long a narrow tail. The Fig. 4.42(a) is the number of atoms of the largest fragment. At the first, the number of atoms is became double of one droplet, then the droplet separation in two main droplet, when the time at near 100ps the largest fragment to meet the 2nd separation, because the trail breakup. At final stage the number of fragment is decreasing by evaporation effect. The Fig. 4.42(b) is the vibrational temperature of atoms of the largest fragment, we find out the temperature rapidly increased when the droplet pair occur impact. After the droplet impact the temperature rapidly fall off during 7~10ps, then the temperature raise up until ~50ps, then the temperature rapidly fall off again when separation occurred. The Fig. 4.42(c) is the rotational energy of the largest fragment, we find out the rotational energy rapidly increased, because the initial relative translation contributed to rotational energy. During 15~100ps the rotational energy decreased function of time, because the largest fragment be stretching, then the energy rapidly fall off when

separation occur. And the Fig. 4.42(d) is the angular momentum of the largest fragment in different directions. Compared Fig. 4.40(a) and Fig. 4.42(a), we find out a interest phenomenon. During 80~120ps, while fragment size decreased by to meet 2nd separation the rotational energy is increased by out of shape of to meet 2nd separation.

The collision behavior of Fig. 4.22 (b=0.25, V=1375 *m/s*) is be classified in shattering separation regime. In this case, the droplet pair to meet huge impact kinetic energy, the droplet fragments into over 5 droplets. The Fig. 4.43(a) is the number of atoms of the largest fragment. At the first, the number of atoms is became double of one droplet, then the largest fragment to meet twice serious fragmentation, during the process the number of fragment is decreased serious than other cases. In the shattering case, we can find out the fragment times is more than shattering case under vacuum. The Fig. 4.43(b) is the vibrational temperature of atoms of the largest fragment, we find out the temperature rapidly increased when the droplet pair occur impact, and the peak value of the temperature is higher than others under the same condition. Then the temperature fall off rapidly when separation occurred at 90ps. The Fig. 4.43(c) is the rotational energy of the largest fragment, we find out the rotational energy rapidly increased, because the initial relative translation contributed to rotational energy. During 15~90ps the rotational energy decreased function of time, because the largest fragment be stretching, then the energy rapidly fall off twice when fragmentations

occur. And the Fig. 4.43(d) is the angular momentum of the largest fragment in different directions.

4.2.3 Droplet-droplet collision under high pressurized ambient

Under this condition, we find out the stretching coalescence, too. At the same time we do captured very clear droplet pair bouncing with very low relative velocities.

The Fig. 4.13~Fig. 4.15 is the snapshots of the head-on (b=0) droplet pair collision under high pressurized ambient (~0.55 atm) with different initial velocity (V=1000, 1250, 1375 and 1500 *m/s*). In Fig. 4.13, (V=1250 *m/s*), we can see the droplet area is increase as the beginning and then the area ruptures to a "ring", at last the ring become a droplet again. In Fig. 4.14, (V=1375), we can see the droplet area is increase as the beginning and then the area ruptures to a "net", at last the "net" fragment into several bigger droplets. In Fig. 4.15, (V=1500 *m/s*), we can see the droplet area is increase as the beginning and then the area ruptures to a "net", at last the "net" fragment into several small droplets. The size of fragmented droplets is still bigger than the droplets of simulation of the same condition under vacuum, and the number of fragments is more than low pressurized ambient (~ 0.055 atm). Because, there are less atoms be vaporized under pressurized ambient, higher pressurized make the droplet atoms collisions times more than others.

The Fig. 4.23~Fig. 4.26 is the snapshots of the non-head-on droplet pair collision

under high pressurized ambient (~0.55 atm) with different initial velocity and different impact parameter.

The collision behavior of Fig. 4.23 (b=0.25, V=250 *m/s*) is be classified in coalescence regime. In this case, the droplet pair move slowly and coalescence become a rotating "bigger" droplet which mass is almost equal the sum of droplet pair mass, as the same conditions under vacuum. The Fig. 4.44(a) is the number of atoms of the largest fragment. We can find out the number of atoms is became double of one droplet, because this is a coalescence case. Then the number of atoms is decreased function of time, because the droplet evaporation is occurring with time increasing. The Fig. 4.44(b) is the vibrational temperature of atoms of the largest fragment, we find out the temperature rapidly increased when the droplet pair occur impact. After the droplet impact the temperature is cold down during time at 100~250ps, at this time the impact energy is completed has been transferred into temperature energy and complete the thermo-equilibrium inside the droplet. After 250ps, the temperature is increased with time, because the droplet evaporation is pulling the atoms from droplet surface. The Fig. 4.44(c) is the rotational energy of the largest fragment, we find out the rotational energy rapidly increased, because the initial relative translation contributed to rotational energy. And the Fig. 4.44(d) is the angular momentum of the largest fragment in different directions. In this case, the Fig. 4.44 is almost the same
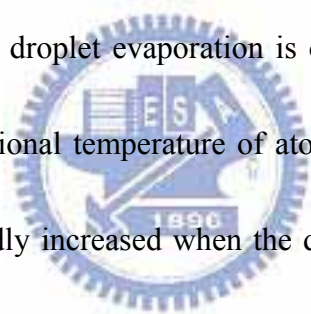
with Fig.4.40. Because the relative velocity is too small, in this case we can't find out

the pressurized ambient effect.

The collision behavior of Fig. 4.24 (b=0.25, V=750 *m/s*) is be classified in

stretching coalescence regime. In this case, the droplet be stretched and rotated

during the process, at final stage, the droplet become into a rotating ball, and there no

breakup occur. The Fig. 4.45(a) is the number of atoms of the largest fragment. In this

figure, we can clearly classified this is a coalescence case. But there two stages of

vaporized rate and the vaporized effect is clearly stronger than typical coalescence

case. Because the droplet be stretched, the surface of droplet is bigger than a

coalescence droplet. The Fig. 4.45(b) is the vibrational temperature of atoms of the

largest fragment, we find out the temperature rapidly increased when the droplet pair

occur impact. After the droplet impact the temperature rapidly fall off during 7~10ps.

The Fig. 4.45(c) is the rotational energy of the largest fragment, we find out the

rotational energy rapidly increased, because the initial relative translation contributed

to rotational energy. During the process the rotational energy decreased function of

time, because the largest fragment be stretched. The energy never falls off rapidly,

and value is ten times of coalescence case, it show clear that the droplet is rotating

with out of shape. And the Fig. 4.45(d) is the angular momentum of the largest

fragment in different directions.
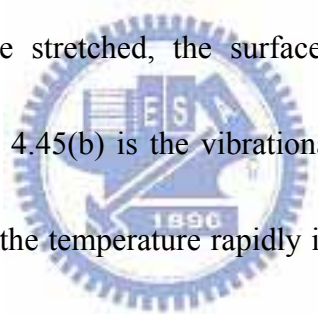
The collision behavior of Fig. 4.25 (b=0.625, V=1000 *m/s*) is be classified in stretching separation regime. In this case, the droplet pair disrupted into 2 droplets and one "satellite" droplets followed short a narrow tail. The Fig. 4.46(a) is the number of atoms of the largest fragment. At the first, the number of atoms became double of one droplet, then the droplet separation in two main droplets. In this case, there is no 2nd separation of largest fragment, because there only one satellite with the other fragment. At final stage the number of fragment is decreasing by evaporation effect. The Fig. 4.46(b) is the vibrational temperature of atoms of the largest fragment, we find out the temperature rapidly increased when the droplet pair occur impact. After the droplet impact the temperature rapidly fall off during 7~10ps, then the temperature raise up until ~50ps, then the temperature rapidly fall off again when separation occurred. The Fig. 4.46(c) is the rotational energy of the largest fragment, we find out the rotational energy rapidly increased, because the initial relative translation contributed to rotational energy. During 15~90ps the rotational energy decreased function of time, because the largest fragment be stretching, then the energy rapidly fall off when separation occur. And the Fig. 4.46(d) is the angular momentum of the largest fragment in different directions.

The Fig. 4.27~Fig. 4.28 is the snapshots of the head-on (b=0) droplet pair collision under high pressurized ambient (~0.55 atm) with very low initial velocity.

These are classified in droplet pair bounce regime. In Fig. 4.27, the relative velocity between droplet is 10 *m/sec*. Form Fig. 4.27(a) to Fig. 4.27(f), we observed the droplet pair to approach each other with very low velocity, and when the distance reach a value the droplet pair stop to approach. At the same time, the vaporized effect occurs .violently and rapidly. The shortest distance between droplet pair is named "gas gap", in previously e.g., [Pan and Law, 2004 and Murad and Law, 1999]. The Fig. 4.28 is the same with Fig. 4.27 with different relative velocity (30 m/sec). The Fig. 4.49 and Fig. 4.50 are the atoms distribution in X direction at various time (time= 25, 250, 500, 750, 1000 and 1250ps) which is mapping Fig. 4.27 and Fig. 4.28. we can find out the time step while the droplet is most close is 750ps. In this analysis, we can to estimate the value of "gas gap". The gas gap of bouncing of droplet pair with 10 m/sec is 4.086 nm. While the relative velocity is 30m/s, the value of gas gap 2.724nm. Therefore, the value of gas gap depends on the magnitude of relative velocity or the magnitude of kinetic energy. We estimated the value of gas gap equal the value of previous studies [Pan and Law, 2004 and Murad and Law, 1999] the value of gas gap is 3~4 nm. The Fig. 4.48(a) is the number of atoms of the largest fragment. During the processes the number of fragment is decreasing by evaporation effect. The Fig. 4.48(b) is the vibrational temperature of atoms of the largest fragment. The Fig. 4.48(c) is the rotational energy of the largest fragment, we find out the
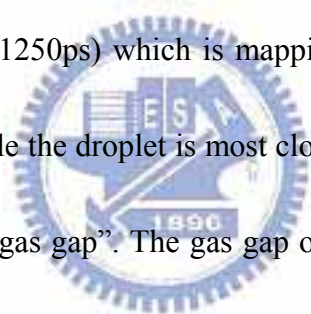
rotational energy is varing in very narrow range. And the Fig. 4.48(d) is the angular

momentum of the largest fragment in different directions. We can find out the angular

momentum occur very strong vibration. Because, the largest droplet impact on the gas

gap.

The Fig. 4.29~Fig. 4.30 is the snapshots of the head-on (b=0) droplet pair

collision under high pressurized ambient (~0.55 atm) but the temperature of ambient

is 324k, which different with Fig. 4.27~Fig. 4.28 (~216 k). These are classified in

droplet pair bounce regime. In Fig. 4.29, the relative velocity between droplet is 10

m/sec. Form Fig. 4.29(a) to Fig. 4.29(f), we observed the droplet pair to approach

each other with very low velocity, and when the distance reach a value the droplet

pair stop to approach. At the same time, the vaporized effect occurs violently and

rapidly. The Fig. 4.30 is the same with Fig. 4.29 with different relative velocity

(30m/sec). The Fig. 4.51 and Fig. 4.52 are the atoms distribution in X direction at

various time (time= 25, 250, 500, 750, 1000 and 1250ps). We can find out the time

step while the droplet is most close is 750ps. The gas gap of bouncing of droplet pair

with 10m/sec is 2.724nm. While the relative velocity is 30m/s, the value of gas gap

4.086 nm. Therefore, the value of gas gap depends on the magnitude of relative

velocity or the magnitude of kinetic energy. We can find out the gas gap distributions

is opposite with Fig. 4.27 and Fig. 4.29. That's because, the higher temperature has
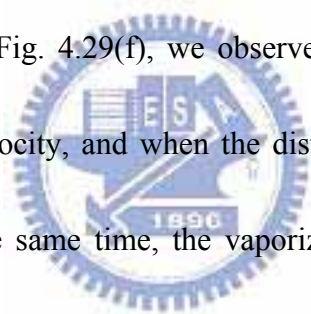
the lower number density value of gas gap and the vaporized atoms is move fast at higher temperature.

4.2.4. Data analysis

Density contour and Size Distribution of head-on cases

We pick the direct coalescence and shattering cases of head-on collision to make Fig. 4.29~Fig. 4.34. Clearly, the fragmentation depends strongly on the collision energy. For coalescence collisions (Fig. 4.29~Fig. 4.31), there is only one large fragment consisting of almost all atoms and some (number <1000) vaporized clusters. For shattering collisions (Fig. 4.32~Fig. 4.34), there are some (over 5) large fragment consisting of hundreds ~ thousands atoms, lot of (number >1000) vaporized clusters and smaller fragments.

Surface tensions variation distribution on the surface of the droplet

We pick the typical cases of direct coalescence, stretching coalescence and droplet bouncing to make Fig. 4.53~Fig. 4.55, which is the surface tension variation distribution on the surface. The Fig. 4.53 is the surface tension variation distribution of direct coalescence case. We can find out the maximum value of the surface tension is occur while the surface film of droplet pair break and then the droplet pair coalescence become a big droplet. We estimate the critical surface tension value of this case is 10.87 dynes/cm. We find out while the droplet occur the shape change the surface tension distribution will varies, too. The Fig. 4.54 and Fig. 4.55 is the surface

tension variation distribution of stretching coalescence and droplet bouncing case. Also, there are very clear surface tensions vary during the collisions.

4.2.5 Distribution map of various regimes

The Fig. 4.1~Fig. 4.3, are the distribution maps of various regimes. The symbols denote coalescences (   ), stretching separations (   ), stretching coalescence (   ) and shattering (   ). Compared Fig. 4.1~Fig. 4.3, we can find out the coalescence region is almost consist under different conditions, in lower relative velocities and bigger impact parameters. And the separation region is distributed in high relative velocities and smaller impact parameter. In pressurized ambient (Fig. 4.2 and Fig. 4.3), we find out a new collisions region between direct coalescence and stretching separation region, named "stretching coalescence". The shattering region is distributed in head-on or a bigger impact parameters, with higher relative velocities which higher than separations cases. Compared Fig. 4.1~Fig. 4.3, we find out the shattering velocity range under vacuum is lowest and the high pressurized ambient is highest. Because, under the high pressurized ambient need more kinetic energy of collisions to shattered the coalescence droplet. We don't mark the bounce regions on these distribution maps, because this is a very narrow region. The relative velocity range of droplet bounce is 10~30m/sec.
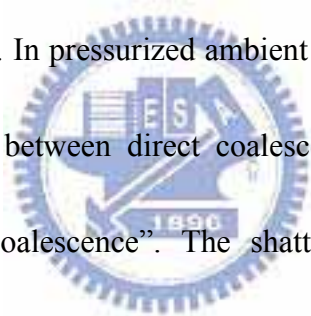
4 .3 Summary

In this chapter, we using the PCMD code to simulated a lot of droplet pair collisions, and make the distribution map of under various conditions, vacuum, low pressurized (~0.055 atm) and high pressurized (~0.55 atm), respectively. We almost capture all collisions behaviors in Fig. 1.2, included, droplet bounce, direct coalescence, stretching separation and shattering. We observed the droplet stretching coalescence behavior for the first time. Then we analysis some typical cases of droplets collisions of various regime by size distribution, density contour, evaporation rate, surface variation rate and energy transfer process. At the last, we make the distribution maps of various regimes under various ambient conditions.
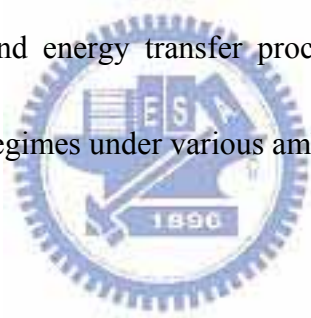
Chapter 5 Concluding Remarks

5.1 Summary

In this thesis, a parallelized cellular molecular dynamics (PCMD) simulation code on memory-distributed parallel machines is developed and verified for its parallel performance. Then, the completed PCMD code is used to study the collision dynamics between two nanoscale droplets under vacuum and pressurized environments. Major findings of these studies can be summarized as follows:

1. Parallel efficiency of the PCMD code is reasonably good for large-scale problems with short-ranged interactions due to dynamic domain decomposition using mutil-level graph-partitioning scheme.

2. Phenomena of nanoscale droplet-droplet collision are very complicated. It can be divided into bouncing, direct coalescence, stretching coalescence, stretching separation and shattering, which strongly depends upon the relative collision velocity, impact parameter and background pressure.

3. Regime maps for various kinds of collision dynamics in the nanoscale are established for the first considering effects of background pressure.

4. Analysis using surface tension on the surfaces between droplets and evolution of cluster energy during collisions has been used in the present thesis and is found very useful in describing the dynamics of the pair droplet

collision in the nanoscale.

5.2 Recommendation for the future work

Based on the studies presented in this thesis, several important future works are
outlined as follows:

1. To study more detailed collision dynamics of the pair droplets considering
   the followings, but not limited to:

   i. Size effects of the two droplets;

   ii. Relative sizes effects of the two droplets;

   iii. Parametric effects of the inter-atomic potential between droplet and
        background gas;

   iv. Rotational effects of the colliding droplets;

   v. More realistic intermolecular potential models such as REBO [Brenner
      et. al., 2002] for hydrocarbon droplets;

2. To study multi-droplet collision dynamics under various kinds of test
   conditions, for example, three-droplet collision;

3. To study the droplet-solid collisions under various kinds of conditions;
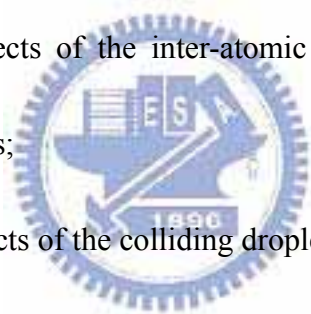
References

1. Ashgriz, N. and Poo, J. Y., Coalescence and separation in binary collisions of liquid drops. Journal of Fluid Mechanics, vol.221, pp.183-204, 1990.

2. Bertagnolli. M., Marchese. M., Jacuci. G., St. Doltsinis. I. and Noelting. S., Thermo-mechanical simulation of the splashing of ceramic droplets on a rigid substract., Journal of Computational Physics, vol.133, pp.205, 1997.

3. Blisten-Barojas. E, and Zachariah. M.R., Molecular-dynamics study of cluster growth by cluster-cluster collisions, Physics Review B., vol.45, pp.4403, .1992.

4. Boghosian. B. M., Computational Physics on The Connection Machine, Comp. In Phys. Jan/Feb, 1990.

5. Brenner. D. W., Shenderova. O. A., Harrison. J. A., Stuart. S. J., Ni. B. and Sinnott. S. B., A second-generation reactive empirical bond order (REBO) potential energy expression for hydrocarbons, Journal of Physics: Condensed Matter, vol.14, pp.783-802, 2002.

6. Bussmann. M., Mostaghimi. J. and Chandra. S., On a three-dimemsional volume tracking model of droplet impact., Physics Fluids, vol.11, pp.1406-1417, 1999.

7. Chen. C. C., Paithankear. D.Y., Talbot. J., and Andres. R. P., Molecular-dynamics study of Au cluster collisions, Z. Physics D., vol.26, S165,1993.

8. Fox. G. C., Johnson. M. A., Lyzenga. G. A., Otto. S. W., Salmon. J. K. and Walker. D. W., Solving Problems on Concurrent Processors: Volume 1., Prentice Hall, Englewood Cliffs, NJ, 1988.

9. Fukai. J., Shiiba. Y., Yamamoto. T., Miyatake. O., Poulikakos. D., Megaridis. C. M. and Zhao. Z., Wetting effects on the spreading of a liquid droplet colliding with a flat surface: experiment and modeling., Physics Fluids, vol.7, pp.236-247, 1995.

10. Gay. J. G. and Berne. B. J., Energy accommodation in collisions of small particles ,Journal of Colloid interface Science, vol.109, pp.90-100, 1986.

11. Greenspan. D. and Heath. L. F., Supercomputer simulation of the modes of colliding microdrops of water, Journal of Physics D, vol.24, pp.2121-2123, 1991.

12. Harlow. F. H. and Shannon. J. P., The splash of a liquid droplet, Journal of Applied Physics, vol.38, pp.3855, 1967.

13. Hu, Z. L., Bruintjes, R. T. and Betterton, E.A., Sensitivity of cloud droplet growth to collision and coalescence efficiencies in a parcel model. Journal of Atmospheric Sciences, vol.15, pp.2502-2515, 1998.

14. Inamuro. T., Ogatat. T., Tajimas. S., Konoshi. N., A lattice Boltzmann method for incompressible two-phase flows with large density difference, Journal of

Computational Physics, vol.198, pp.628–644, 2004.

15. J.-S. Wu and K.-C. Tseng, Concurrent DSMC Method Using Dynamic Domain Decomposition, The 23rd International Symposium on Rarefied Gas Dynamics, Whistler Conference Centre Whistler, British Columbia, July, pp.20-25, 2002.

16. Jellinek, J. and D. H. Li., Separation of the energy of overall rotation in any N-body system. Physical Review Letters, vol.62, pp.241-244, 1989.

17. Karypi. G. s, Schloegel. K. and Kumar. V., ParMetis, University of Minnesota, Department of computer Science, September, 1998.

18. Lennard-Jones J. E., The determination of molecular fields. I. from the variation of the viscosity of gas with temperature., Proc. Roy. Soc. (Lond), vol.106A, pp.441, 1924.

19. Low, T. B. and List, R., Collision, coalescence and breakup of raindrops. Part I: experimentally established coalescence efficiencies and fragment size distributions in breakup. Journal of Atmospheric Sciences, vol.39, pp.1591-1606, 1982.

20. Mackay, G. D. M. and Mason, S. G., The gravity approach and coalescence of fluid droplets and liquid interfaces. Canadian Journal of Chemical Engineering, vol.41, pp.203, 1963.

21. Murad, S. and Law, C. K., Molecular simulation of droplet collision in the presence of ambient. Molecular Physics, vol.96, pp.81-85, 1999.

22. Nicol. D. M. and J. Saltz. H. et al., Dynamic Remapping of Parallel Computations with Varying Resource Demands, IEEE Transactions on Computer, vol.37, pp.1073-1087, 1988.

23. Pan, K. L. and Law, C. K., On the dynamics of head-on droplet collision: experiment and simulation. *The 42nd AIAA Aerospace Sciences Meeting & Exhibit*, Reno, USA, Paper Number 1159 (January, 2004).

24. Pan, K. L. and Law, C. K., Dynamics of droplet-film collision. *The 43rd AIAA Aerospace Sciences Meeting & Exhibit*, Reno, USA, Paper Number AIAA-2005-0352 (January, 2005).

25. Pasandideh-Fard. M., Chandra. S. and Mostaghimi. J., A three-dimensional model of droplet impact and solidification, Internal Journal of Heat and Mass Transfer, vol.45, pp.2229-2242, 2002.

26. Plimpton. S., Fast Parallel Algorithms for Short-Range Molecular Dynamics, J. of Computational Physics, vol.117, pp.1-19, 1995.

27. Stillinger. F. H., Rigorous basis of the Frenkel-Band theory of association Equilibrium , The Journal of Chemical Physics, vol.38, pp.1486-1494, 1963.

28. Succi, S., The lattice Boltzmann equation for fluid dynamics and beyond. Oxford University Press, 2001.

29. Svanberg, M., Pettersson, J.B.C. and et.al., Collision dynamic of large argon clusters. Journal of Physics and Chemistry, vol.101, pp.4011-4018, 1997.

30. Svanberg, M., Pettersson, J.B.C. and et.al., Collision dynamic of large water clusters. Journal of Chemical Physics, vol.108, pp.5888-5897, 1998.

31. Tabor. D., Gases, Liquids, Solids: and other states of matter., Cambridge University Press, New York, NY, 1991.

32. Trapaga. G. and Szekely. J., Mathematical modeling of the isothermal impingment of liquid droplets in spraying processes., Metall. Trans. B, vol.22, pp.901, 1991.

33. Tsurutani. K. , Yao. M., Senda. J. and Fujimoto. H., Numerical analysis of the deformation process of a droplet impinging upon a wall., , JSME Int. Ser., pp.555, 1990.

34. Waldvogel. J. M. and Poulikakos. D., Solidification phenomena in picoleter size solder droplet deposition on a composite substrate., Internal Journal of Heat and Mass Transfer, vol.40, pp.295-309, 1997.

35. Zhao. Z., Poulikakos. D. and Fukai. J., Heat transfer and fluid dynamics during the collision of a lquid droplet on a substrate-I. Modeling., Internal Journal of Heat and Mass Transfer, vol.39, pp.2771-2789, 1996.
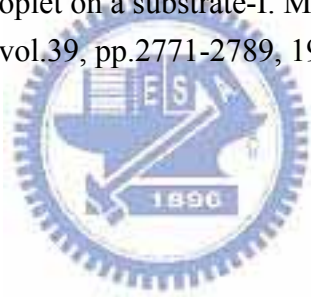
Tables

* System of Units Used in Soft-Sphere Molecular Dynamics Programs *

Fundamental Quantities:

Mass m =   mass of one atom

Length σ

Energy ε

Time $\sigma\sqrt{m/\varepsilon}$

Derived Quantities:

Adiabatic compressibility	$k_s^* = k_s \varepsilon / \sigma^3$
Configurational internal energy	$U_c^* = U_c / N_\varepsilon = \langle u^* \rangle = \langle u / N_\varepsilon \rangle$
Density	$\rho^* = N\sigma^3 / V$
Force	$F^* = F\sigma / \varepsilon$
Heat capacity	$C_v^* = C_v / Nk$
Radial position	$r^* = r / \sigma$
Pressure	$P^* = P\sigma^3 / \varepsilon$
Temperature	$T^* = kT / \varepsilon$
Thermal pressure coefficient	$\gamma_v^* = \gamma_v \sigma^3 / k$
Total energy	$E^* = E / N\varepsilon$
Velocity	$\upsilon^* = \upsilon\sqrt{m/\varepsilon}$

Table. 1 nondimensionalize

	Temp.(T^*)	Density (ρ^*)	No. of Link-cells
condensed	0.7	0.7	75*75*75
vaporized	1.1	0.7	75*75*75
supercritical	0.7	0.7	39*39*39

Table. 2　Simulation conditions for three different cases via PCMD code (condensed, vaporized and supercritical states).

Figures
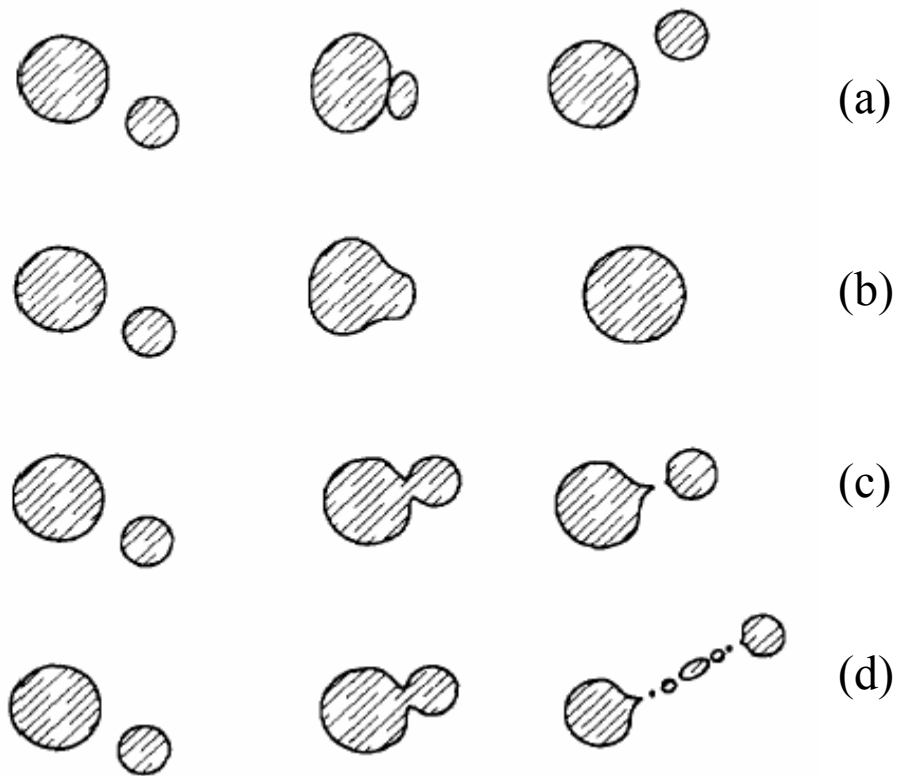
Fig. 1. 1 Terminology of possible droplet-droplet collision outcome, (a) bounce, (b) coalescence, (c) disruption and (d) fragmentation.
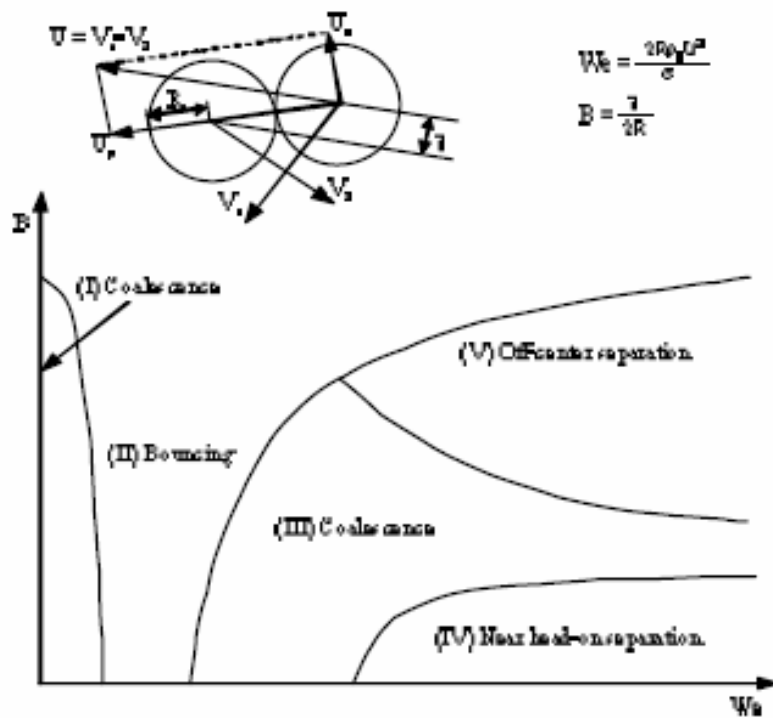
Fig. 1. 2   Schematic of different droplet collision regimes as function of Weber number (**We**) and impact number (**b**).
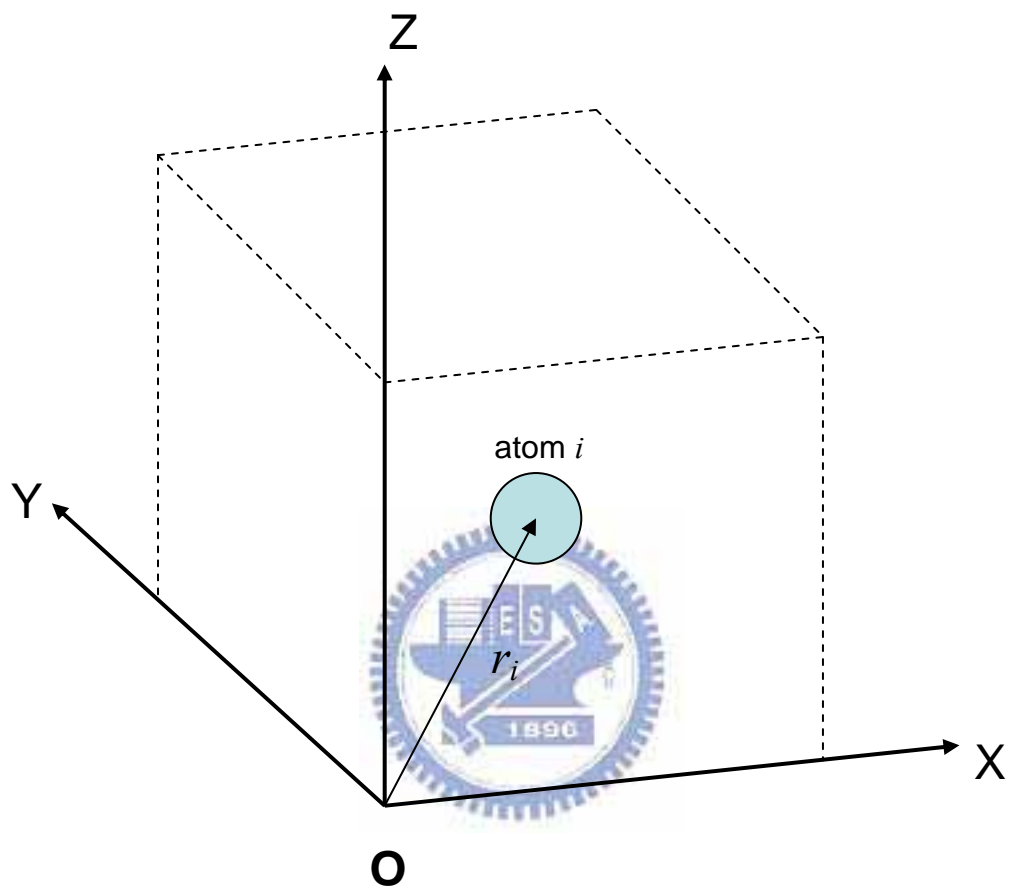
Fig. 2. 1 Cartesian frame
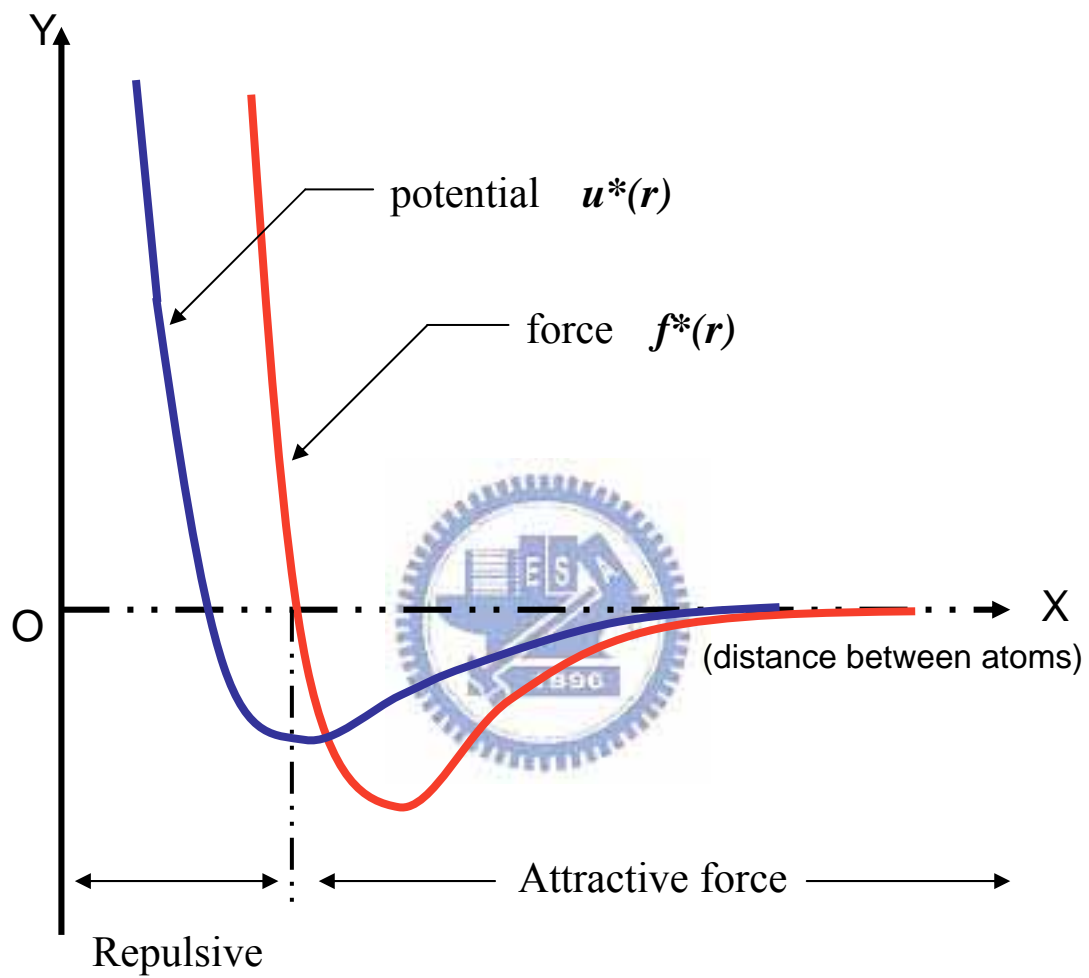
Fig. 2. 2   Lennard-Jones (LJ) pairwise intermolecular potential
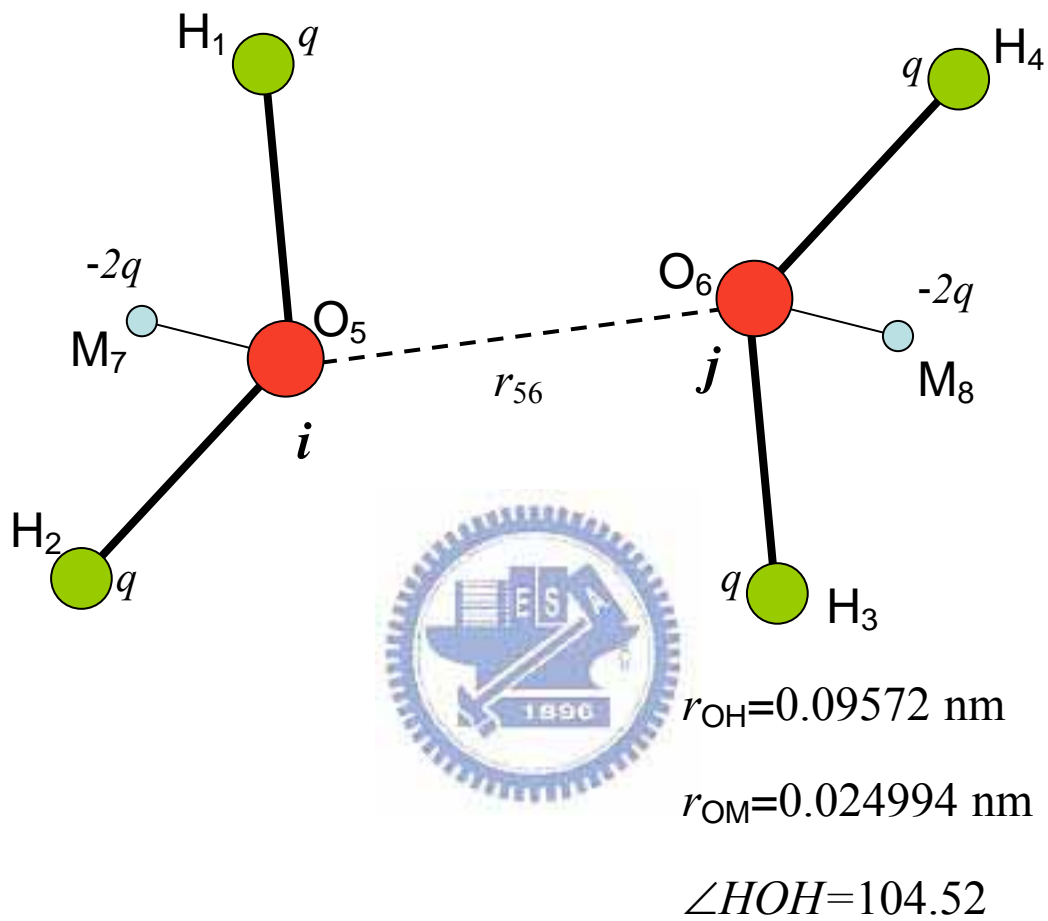
Fig. 2. 3　Water molecules *i* and *j*.
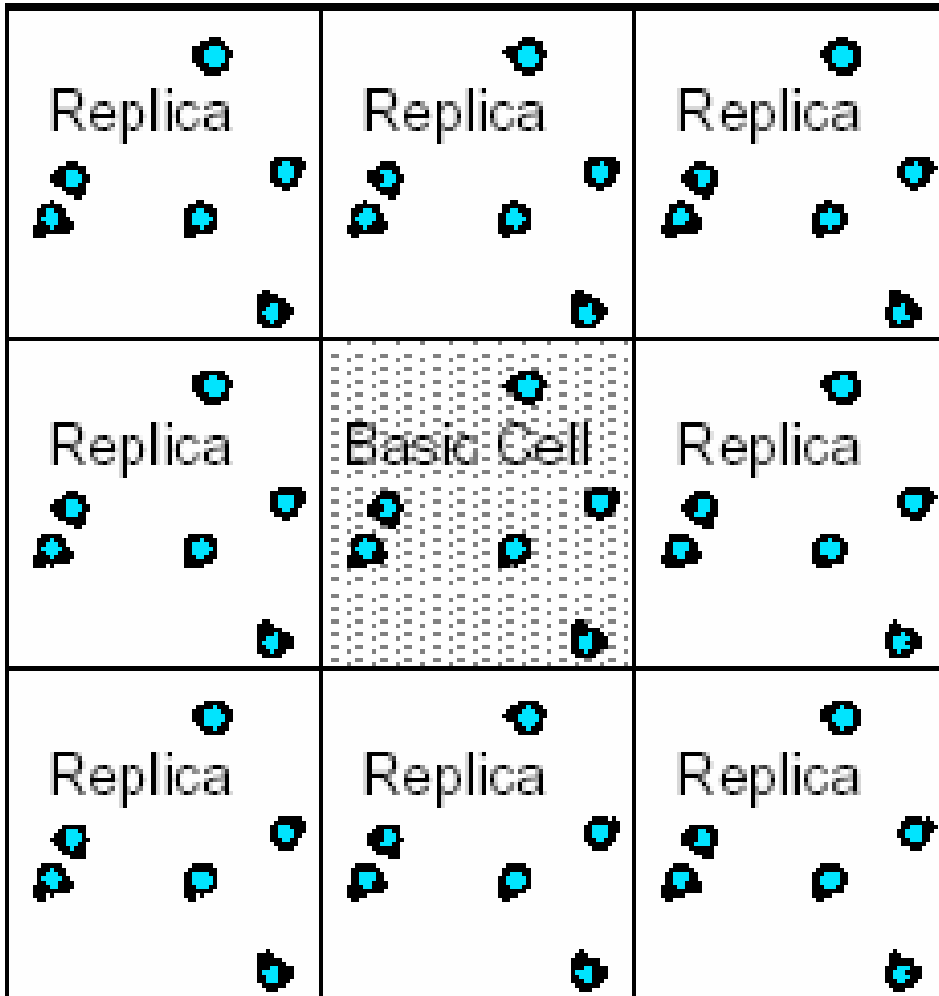
Fig. 2. 4   periodic boundary conditions
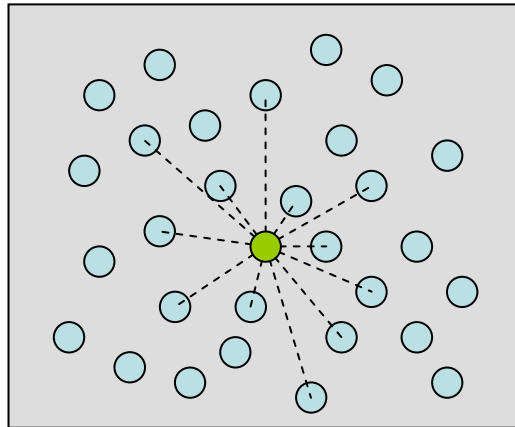
(a)
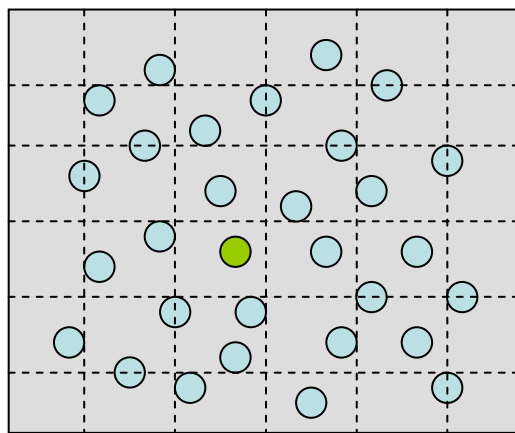
(b)
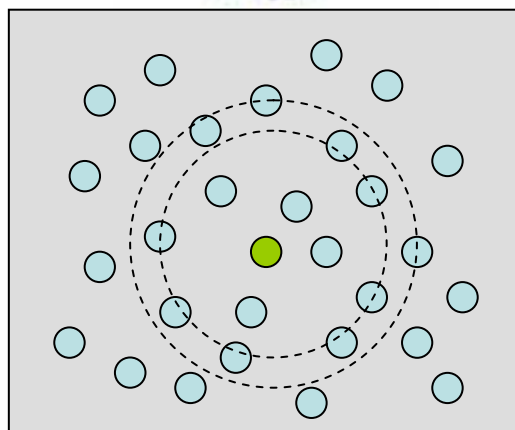
(c)

Fig. 2. 5   (a.)all pair, (b)cell link, and (c)Verlet list methods
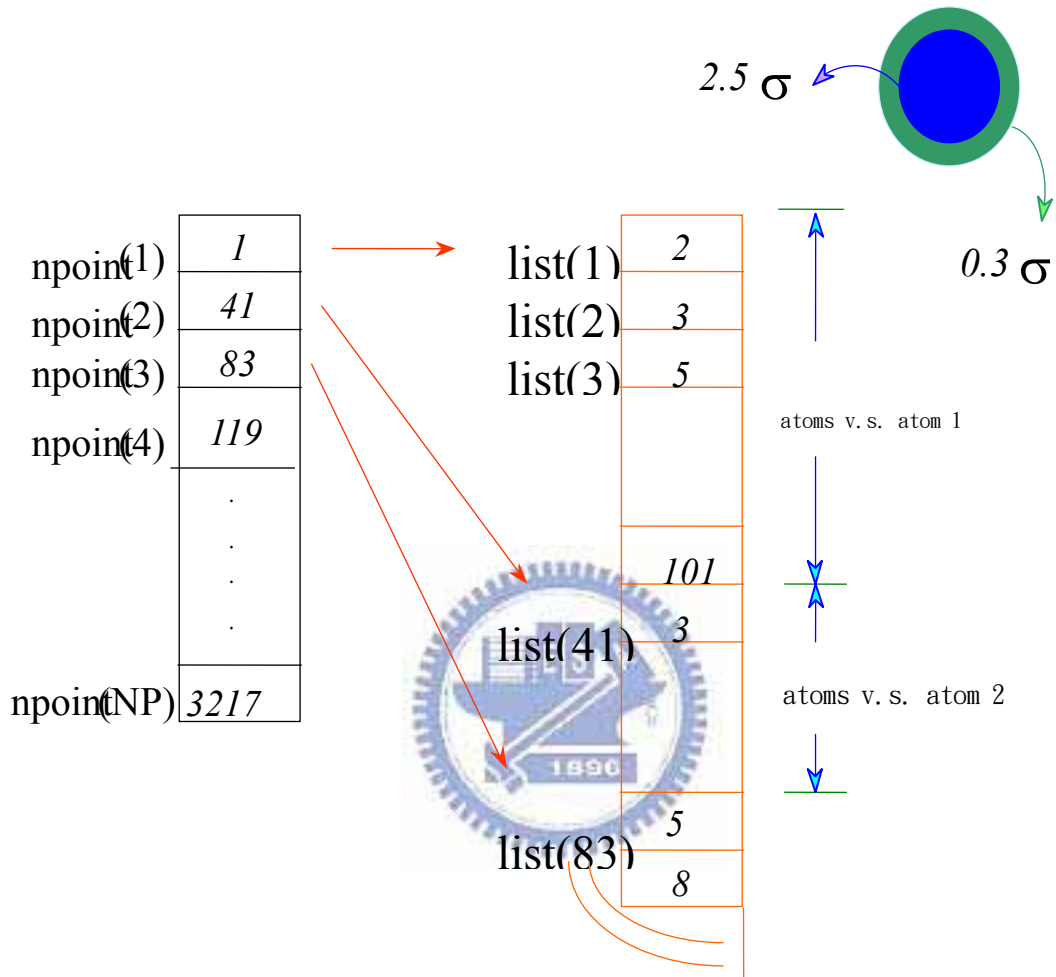
Fig. 2. 6　Verlet list
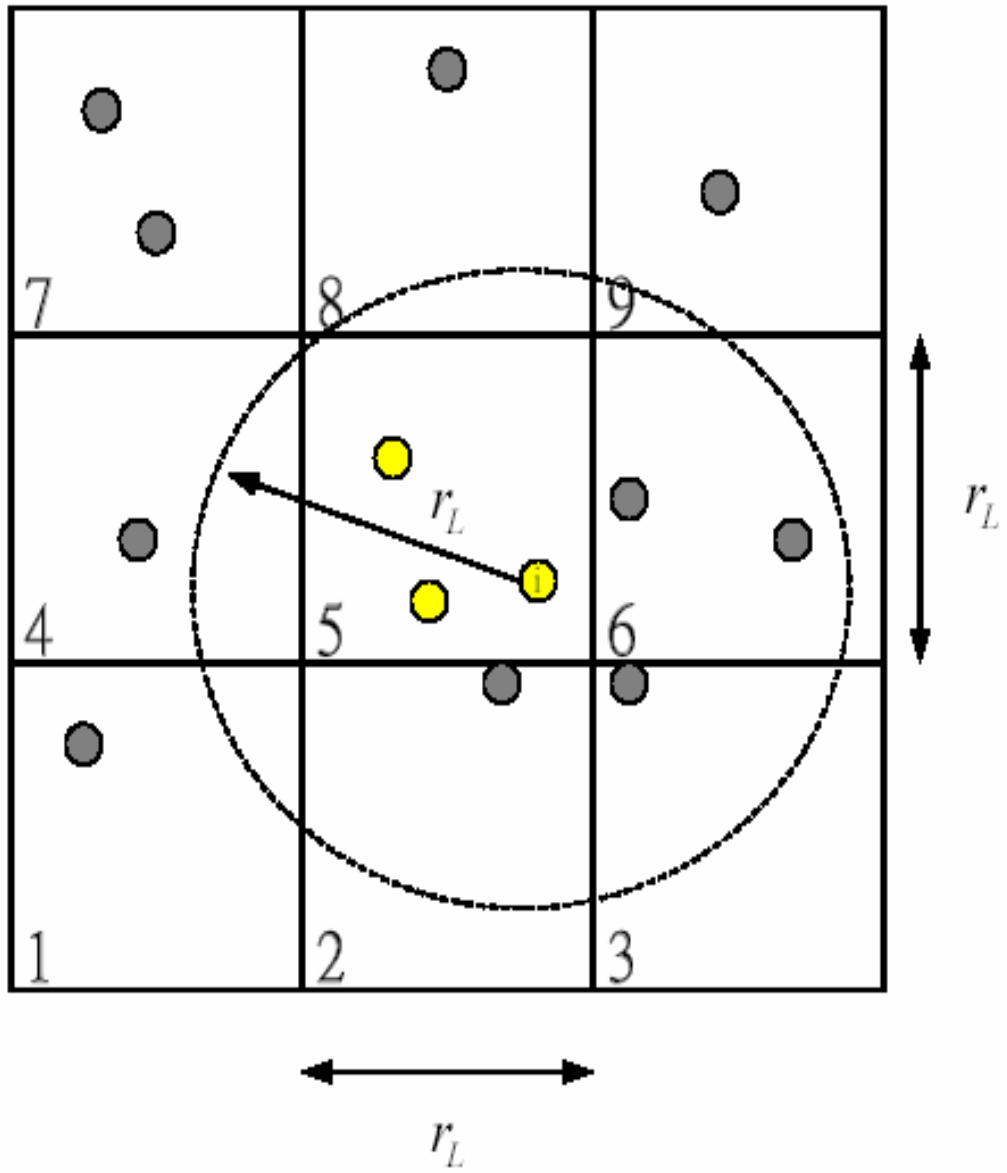
Fig. 2. 7 Verlet +Cell link
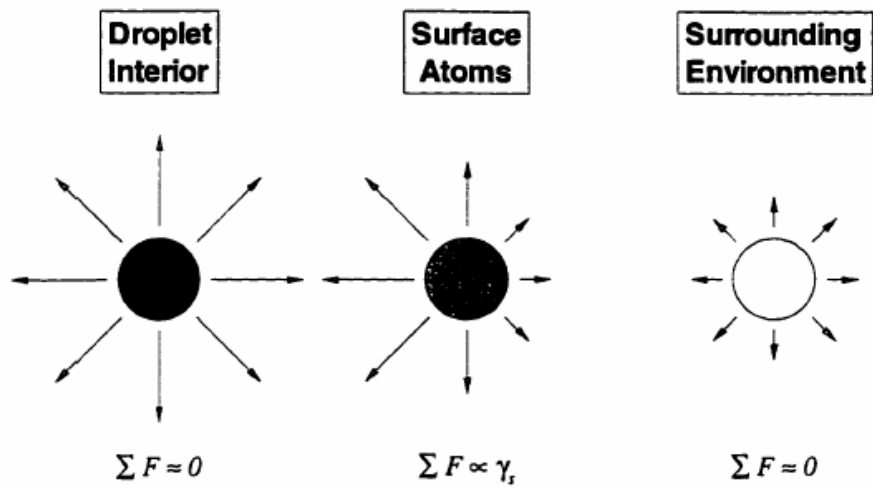
Fig. 2. 8   Surface tension concept by Tabor [1991]
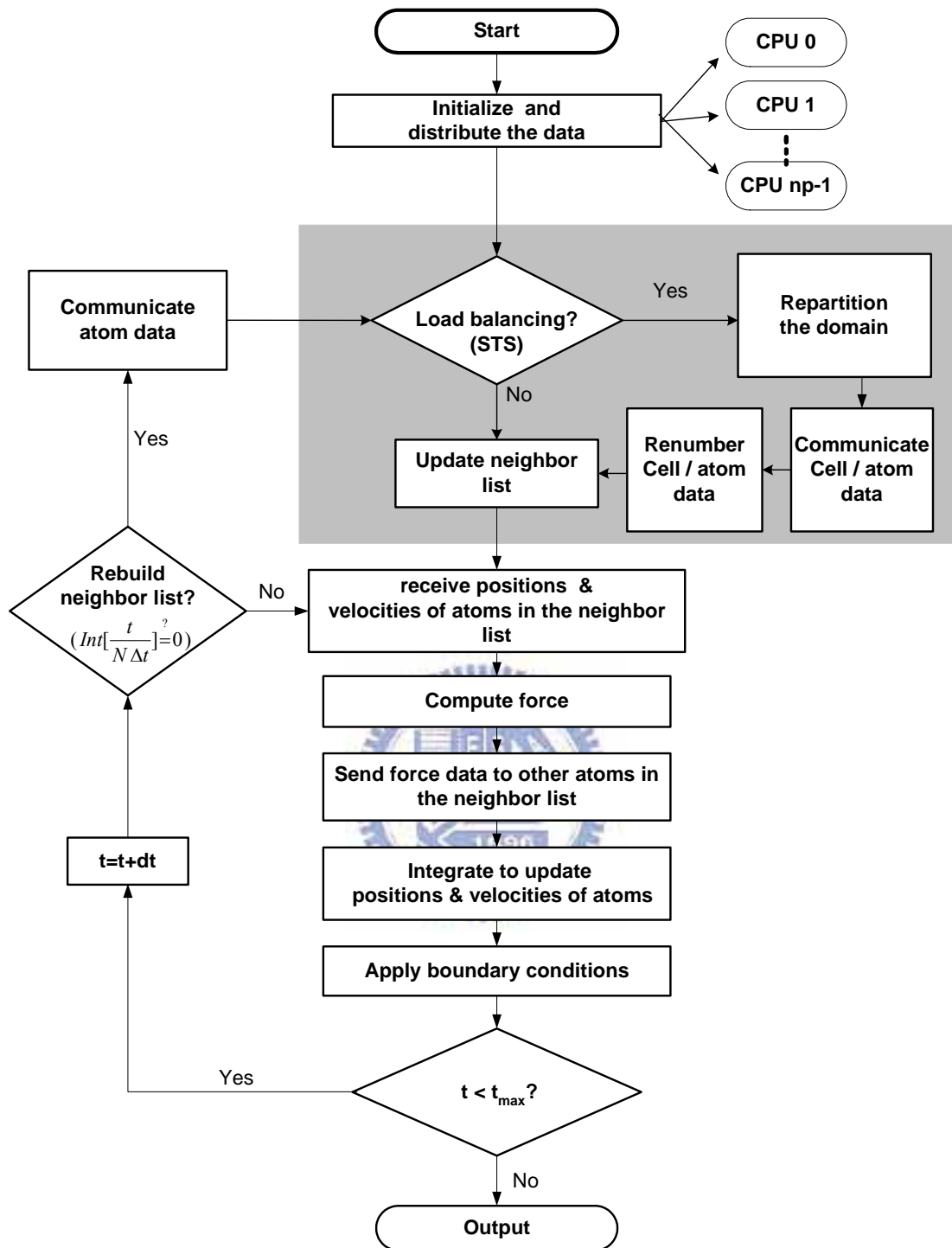
Fig.3. 1 Proposed flow chart for parallel molecular dynamics simulation using dynamic domain decomposition.
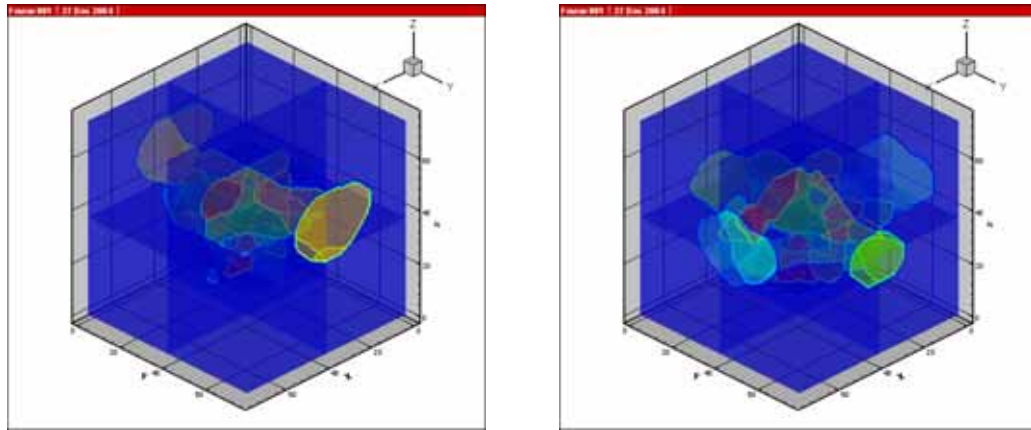
(a)
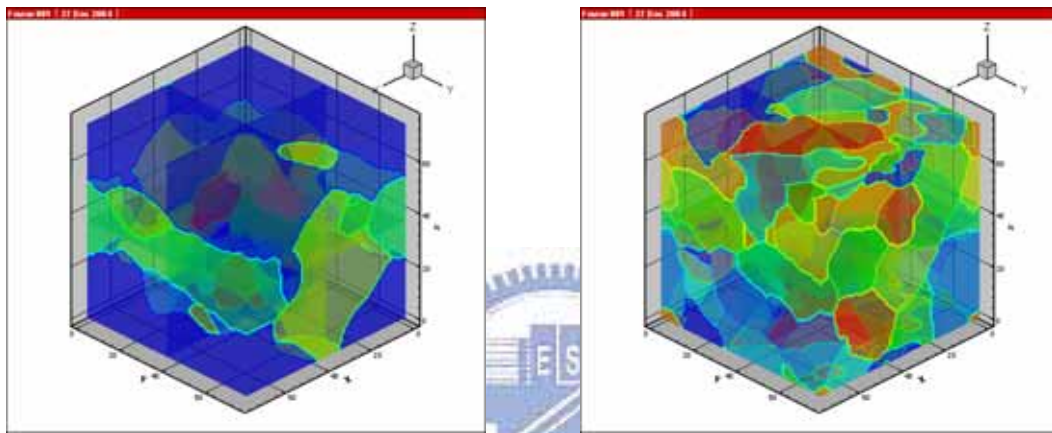
(b)
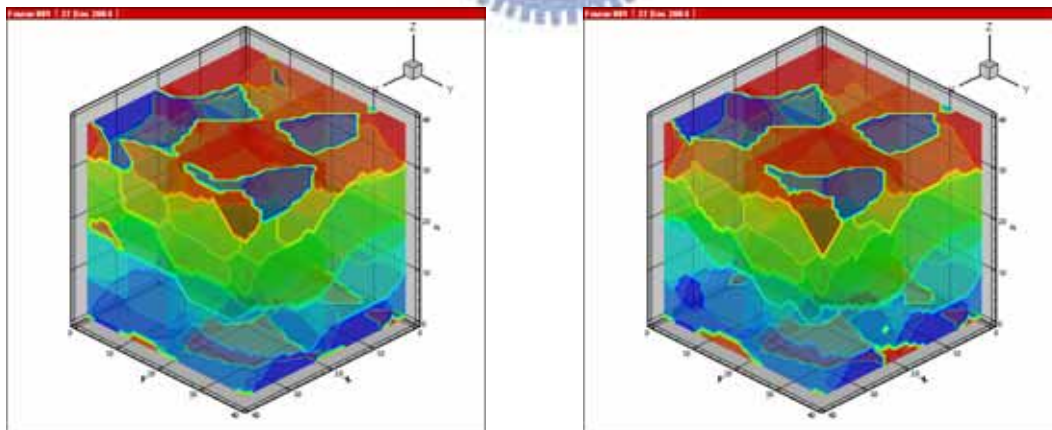
(c)

Fig. 3. 1   Evolution of domain decomposition for large problem size using 25 processors at start and final. (a) condensed state; (b) vaporized state; (c) supercritical state.
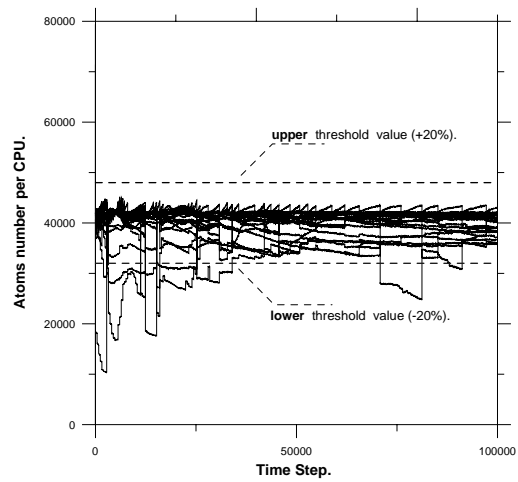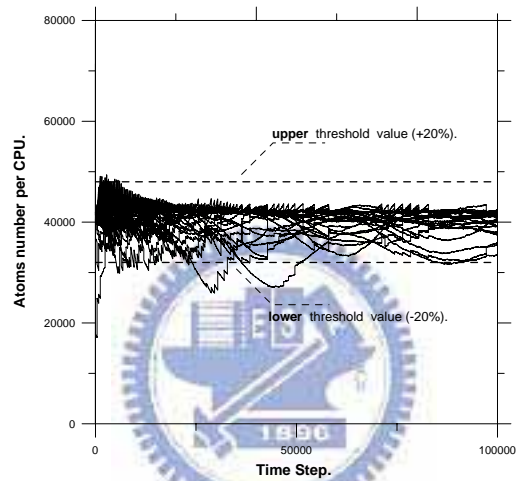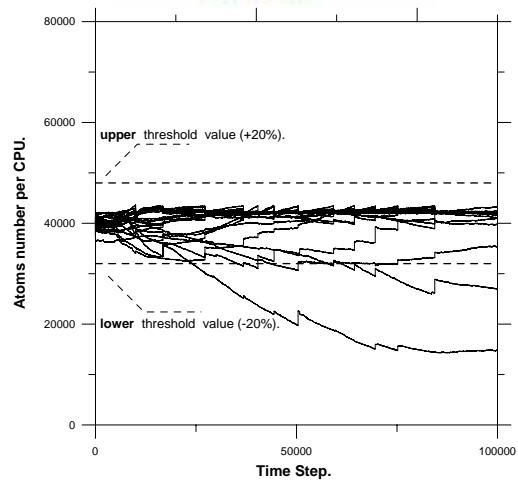
Fig.3.3 Distribution of the number of atoms in each processor as a function of simulation time steps (25 processors). (a) condensed state; (b) vaporized state; (c) supercritical state.
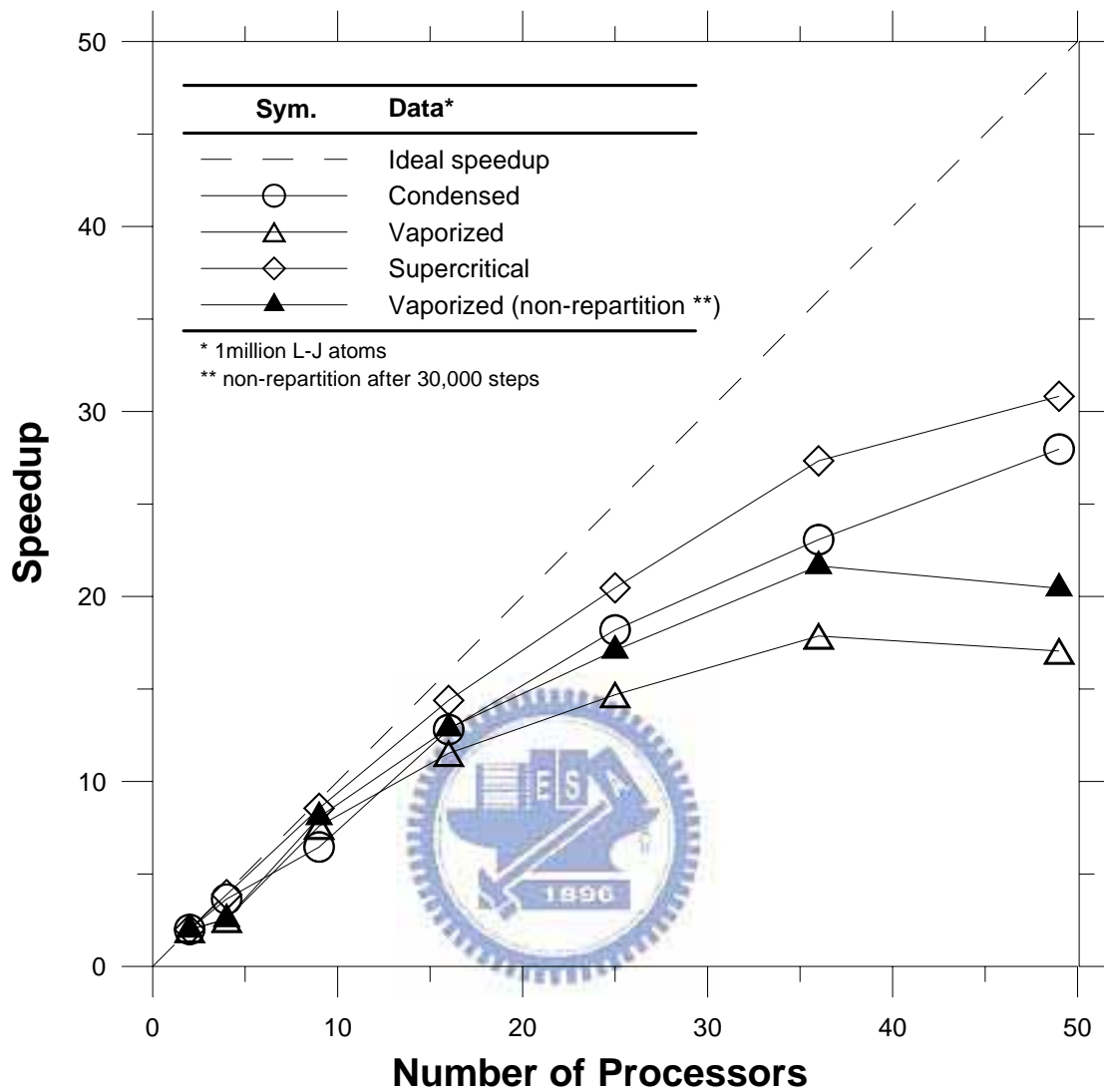
Fig.3.4　Parallel speedup as a function of the number of processors for three different test cases (condensed, vaporized and supercritical states).
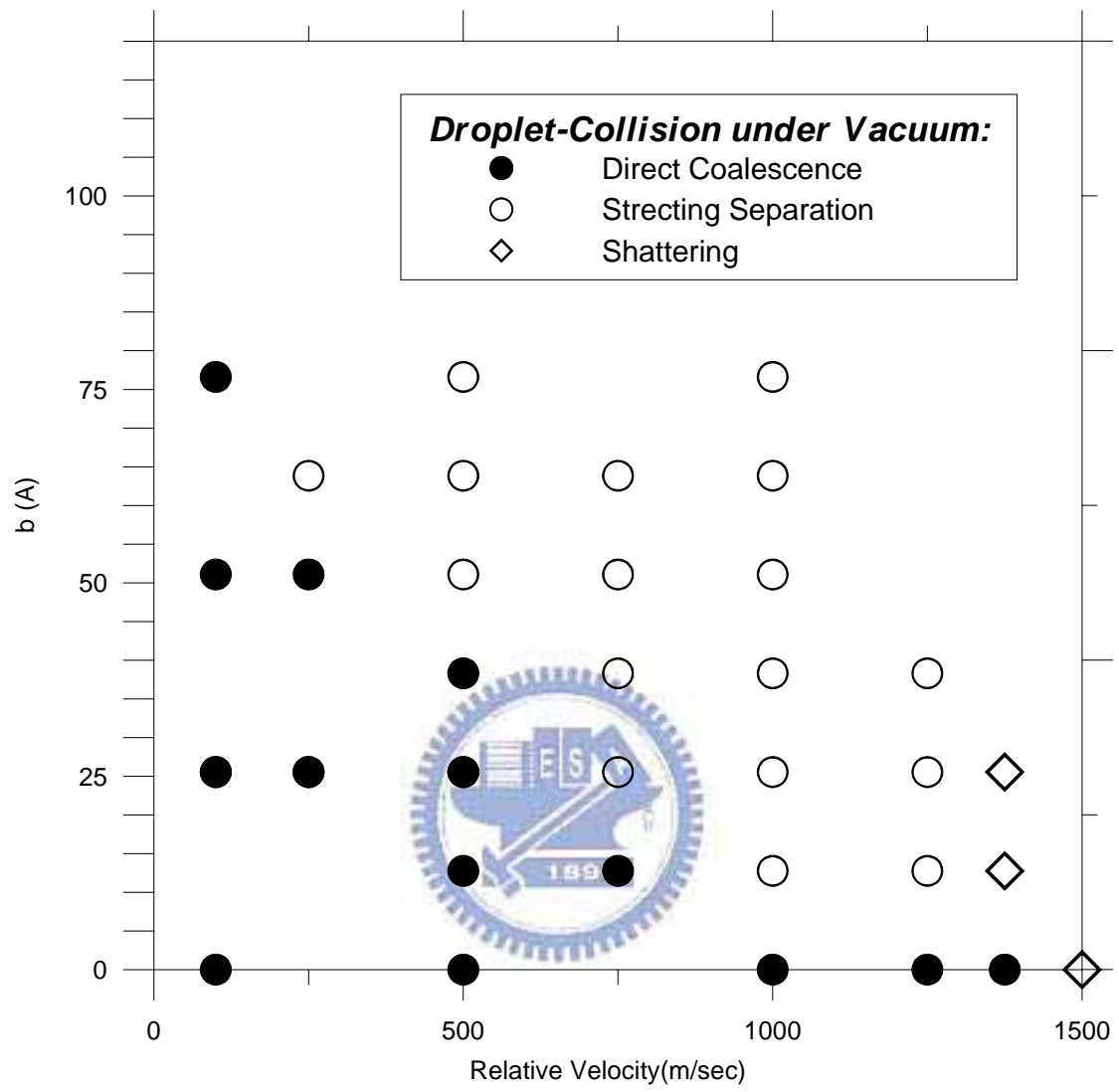
Fig. 4. 1　Distribution map of various regimes under **vacuum ambient**.
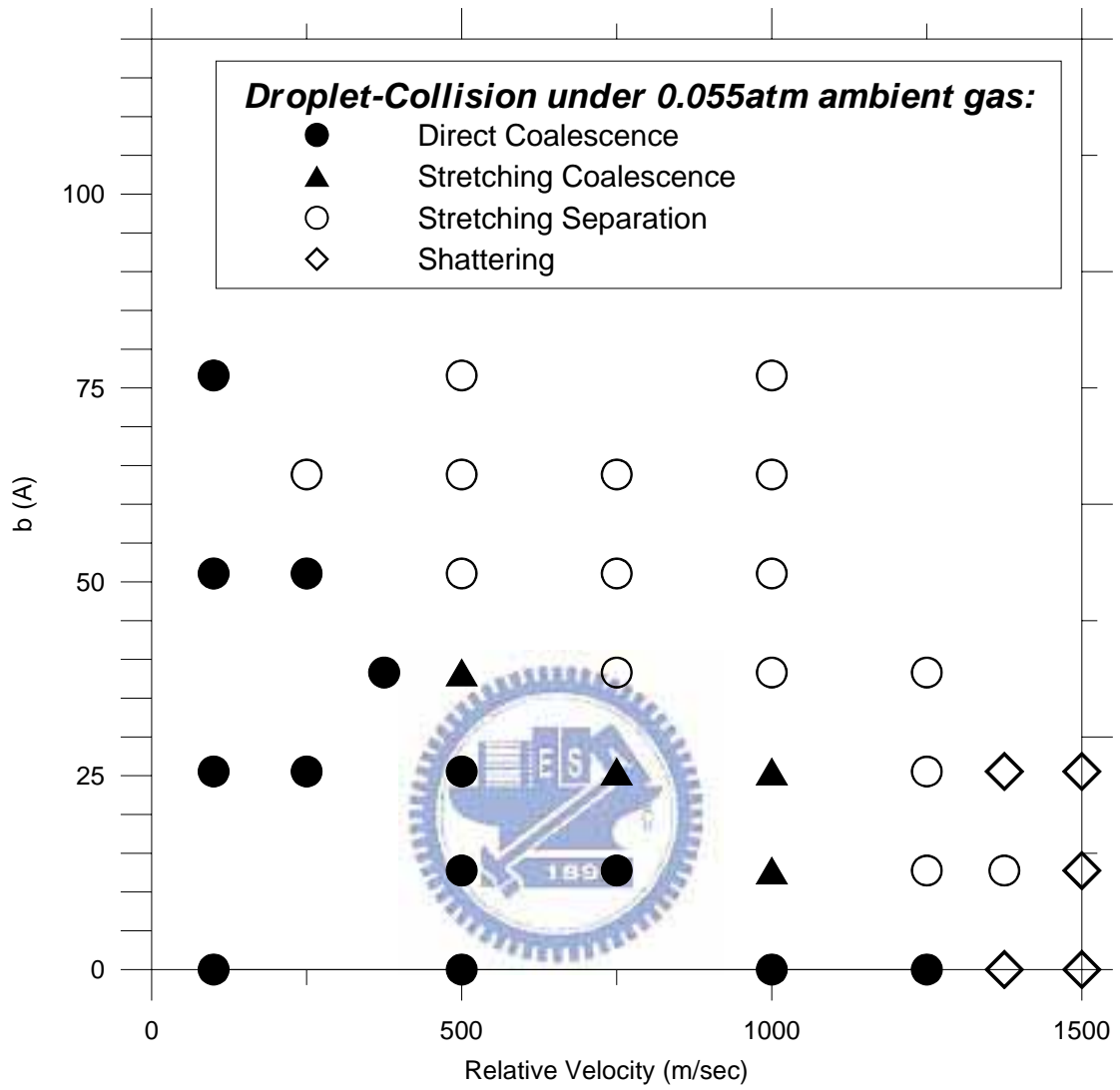
Fig. 4. 2   Distribution map of various regimes under **low pressurized ambient (~0.055 atm)**.
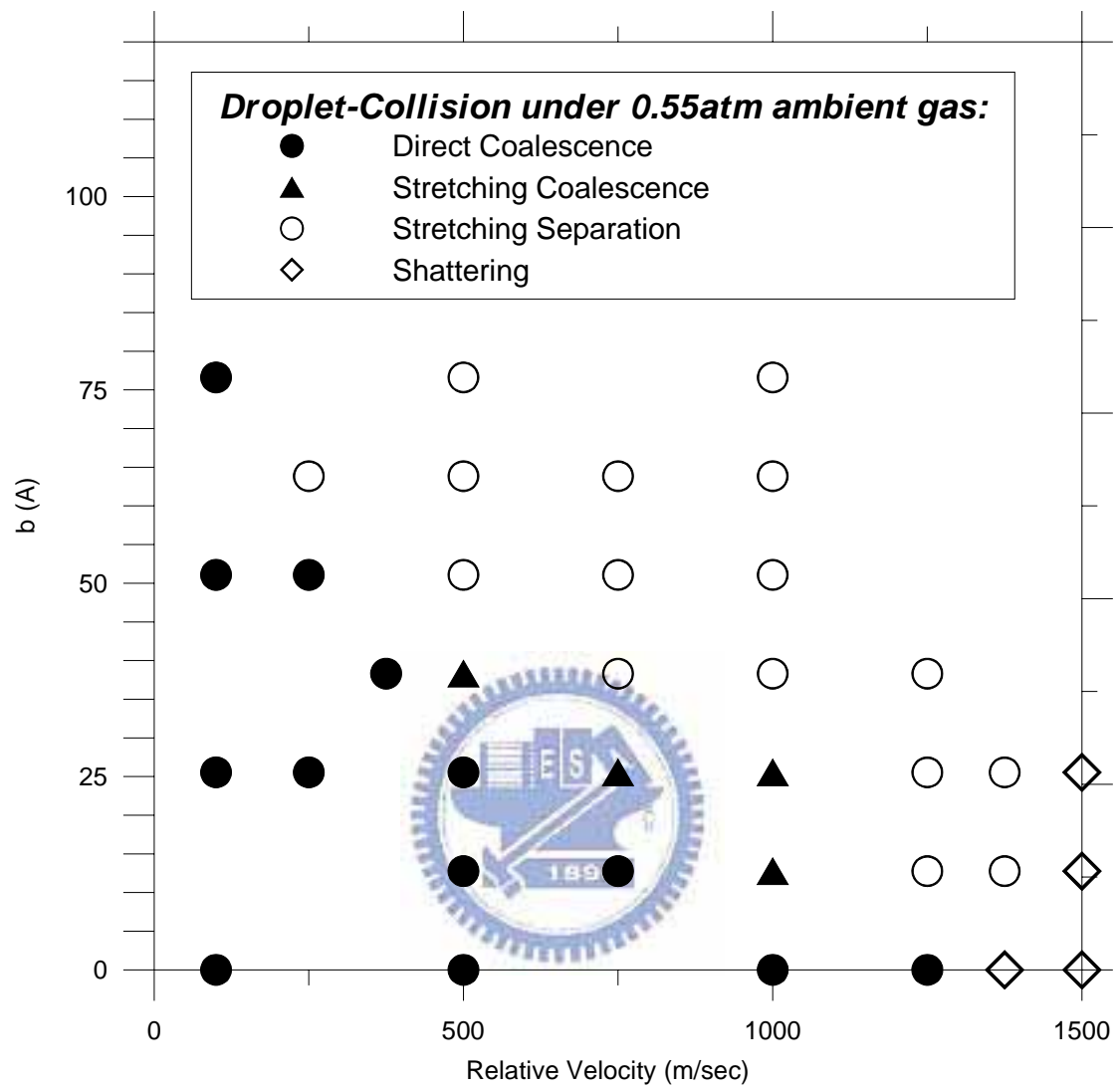
Fig. 4. 3   Distribution map of various regimes under **high pressurized ambient (~0.55 atm)**.
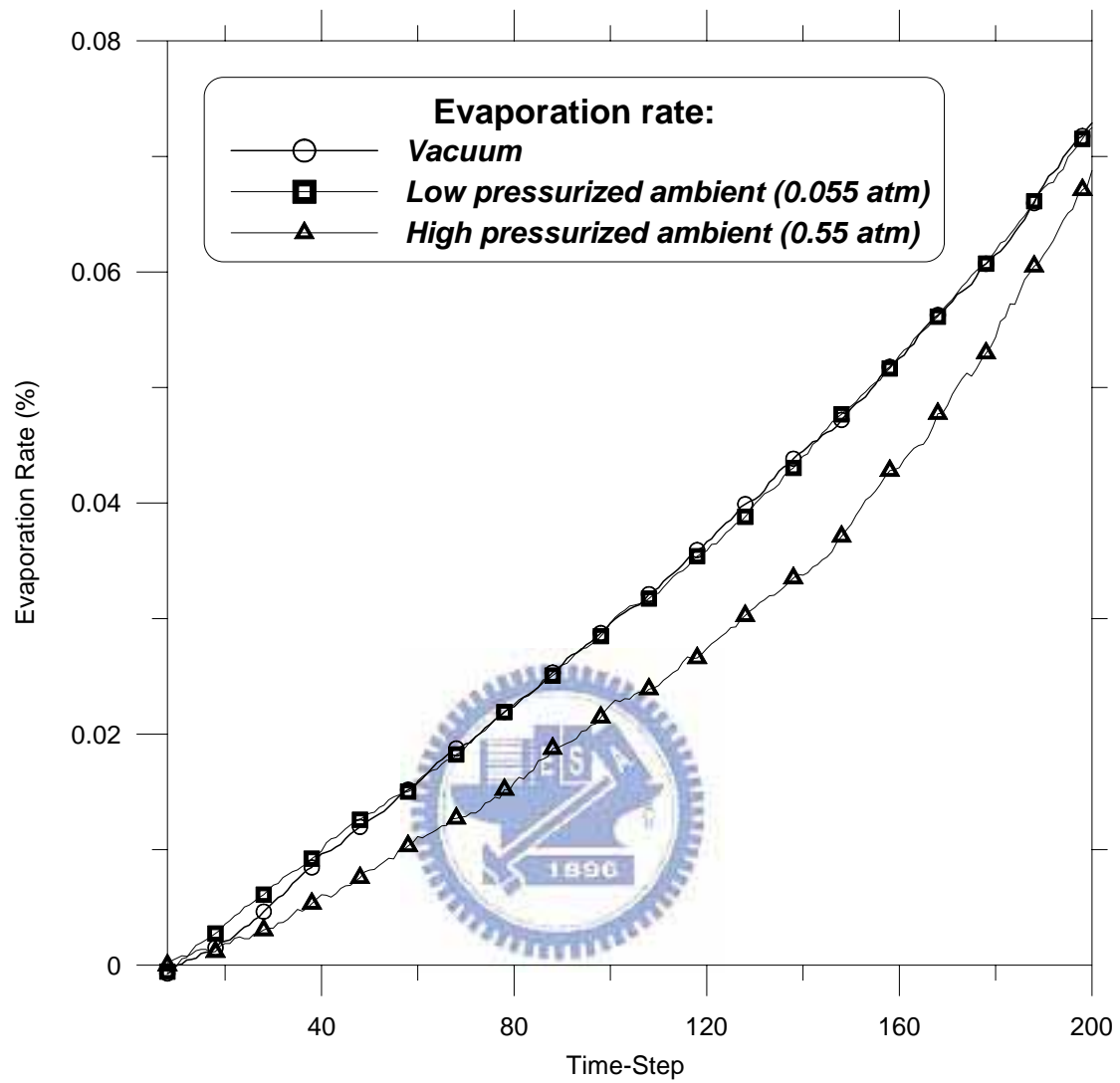
Fig. 4. 4 The evaporation rate of simulation case which b=0.25 V=250 *m/s*, under
vacuum, **low pressurized ambient** and **high pressurized ambient**, respectively.

91
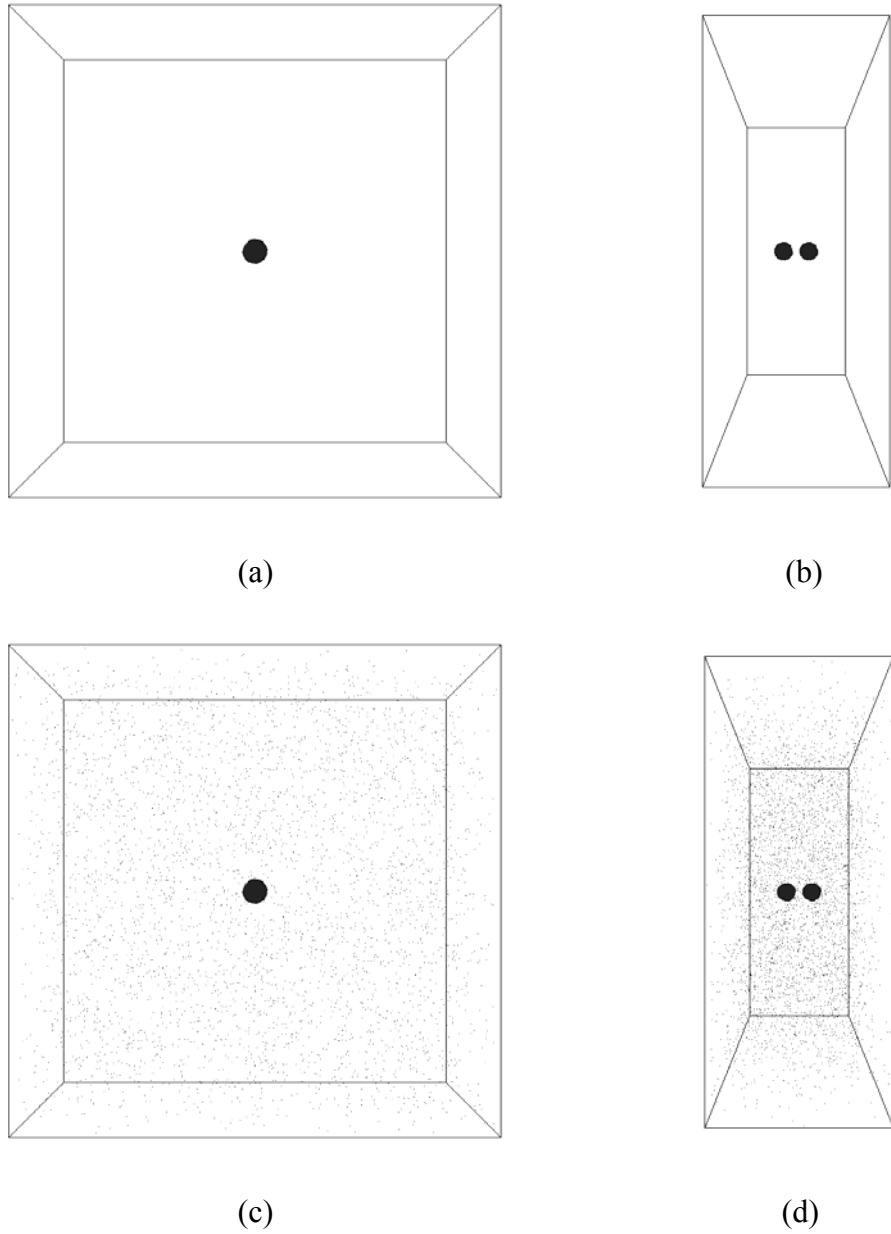
Fig. 4.5　Head-on (b= 0) droplets pair collision initial setup, (a) y-z plane without vapor ambient, (b) x-z plane without vapor ambient, (c) y-z plane under vapor ambient, (d) x-z plane under vapor ambient
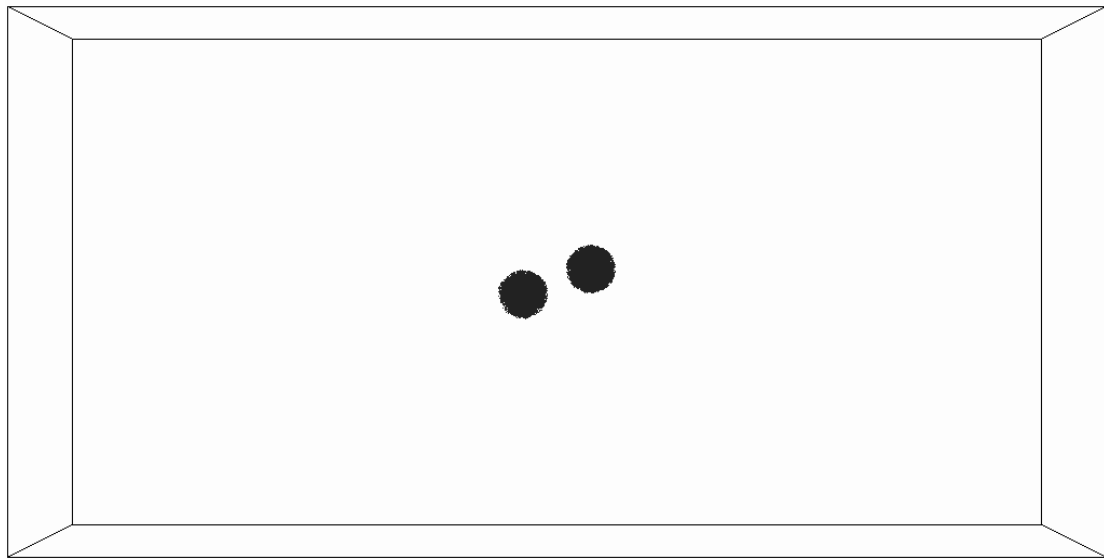
(a)
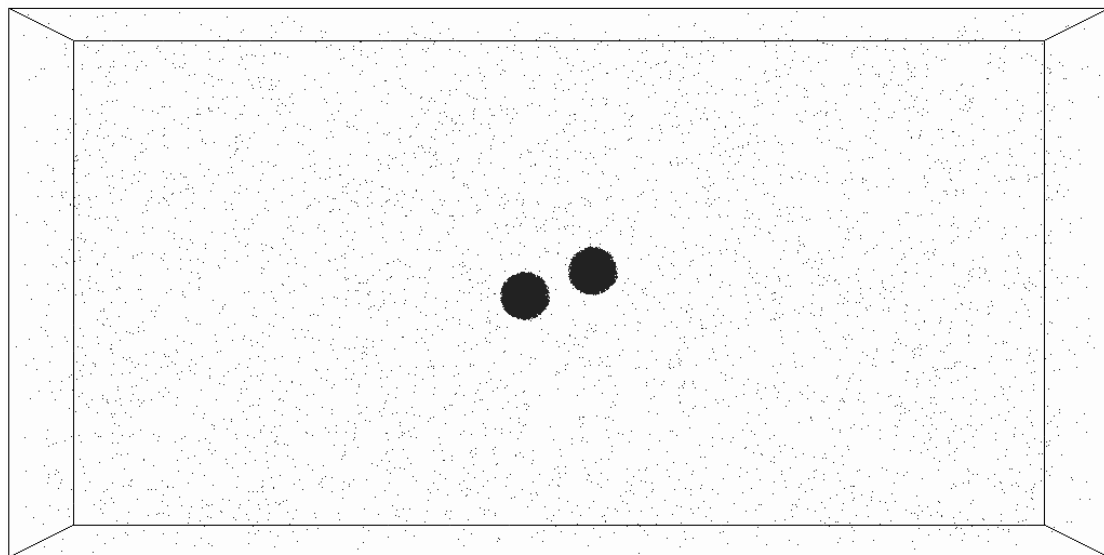
(b)

Fig. 4.6　Non-head-on (ex; b= 0.5) droplets pair collision initial setup, (a) x-y plane without vapor ambient, (b) x-y plane under vapor ambient.

(a)

(b)

(c)

(d)

(e)

(f)
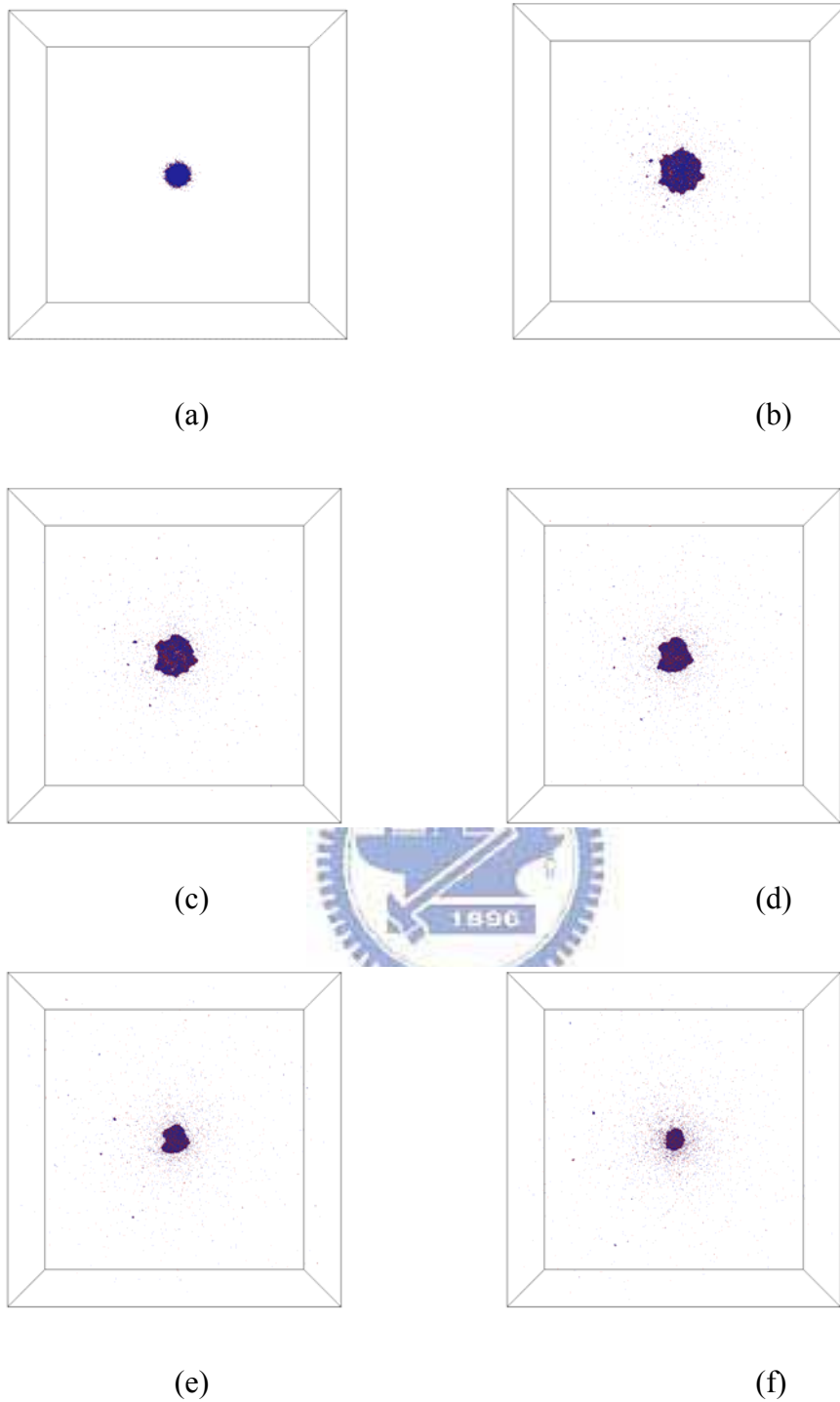
Fig. 4.7   Snapshot of droplet pair collision **under vacuum** b=0 V=1250 *m/s*, at
(a)10ps, (b)50ps, (c)75ps, (d)100ps, (e)125ps, (f)175ps.

94

(a)

(b)

(c)

(d)

(e)

(f)
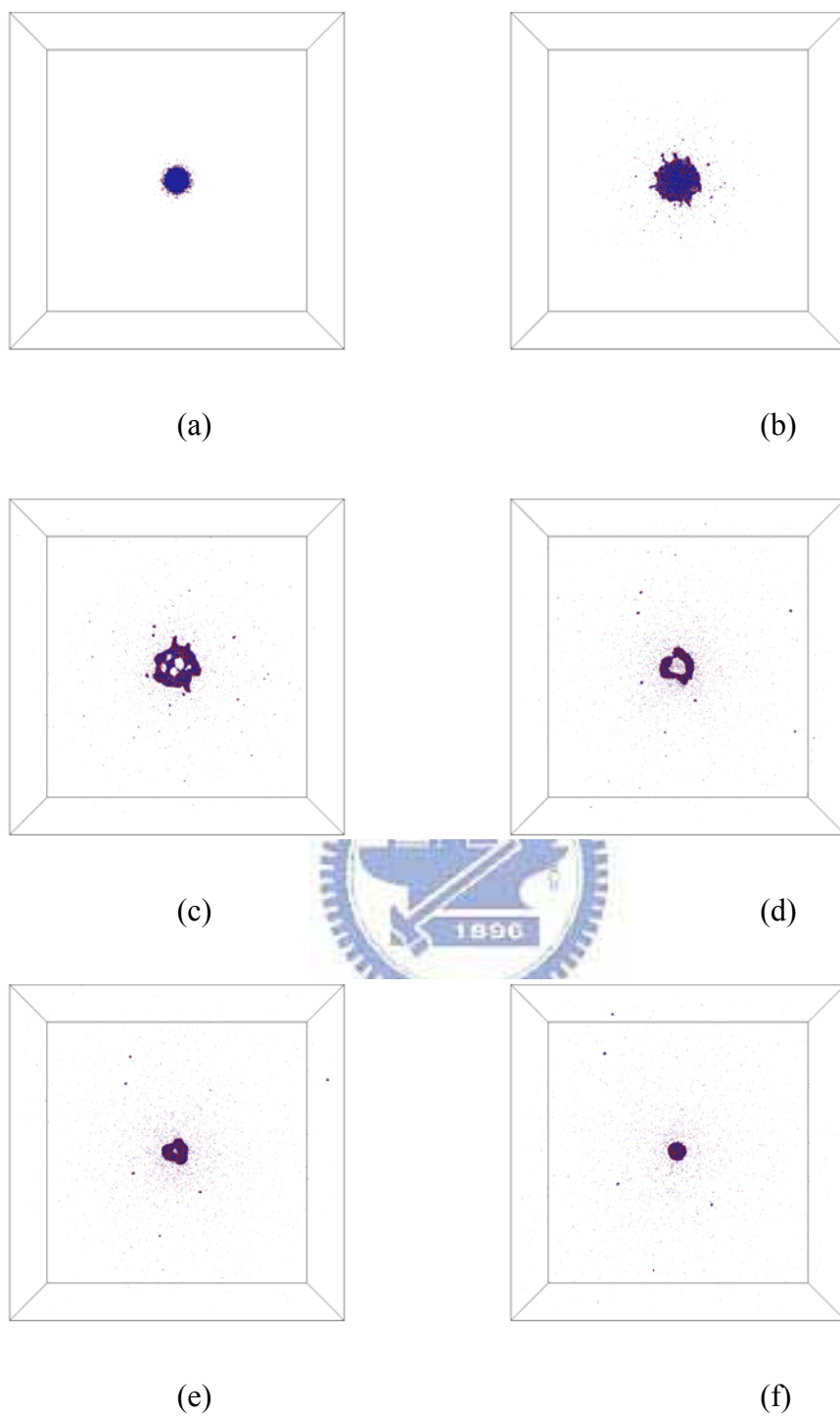
Fig. 4.8 Snapshot of droplet pair collision **under vacuum**, b=0, V=1375 *m/s*, at (a)10ps, (b)40ps, (c)75ps, (d)150ps, (e)200ps, (f)300ps.

(a)   (b)

(c)   (d)

(e)   (f)
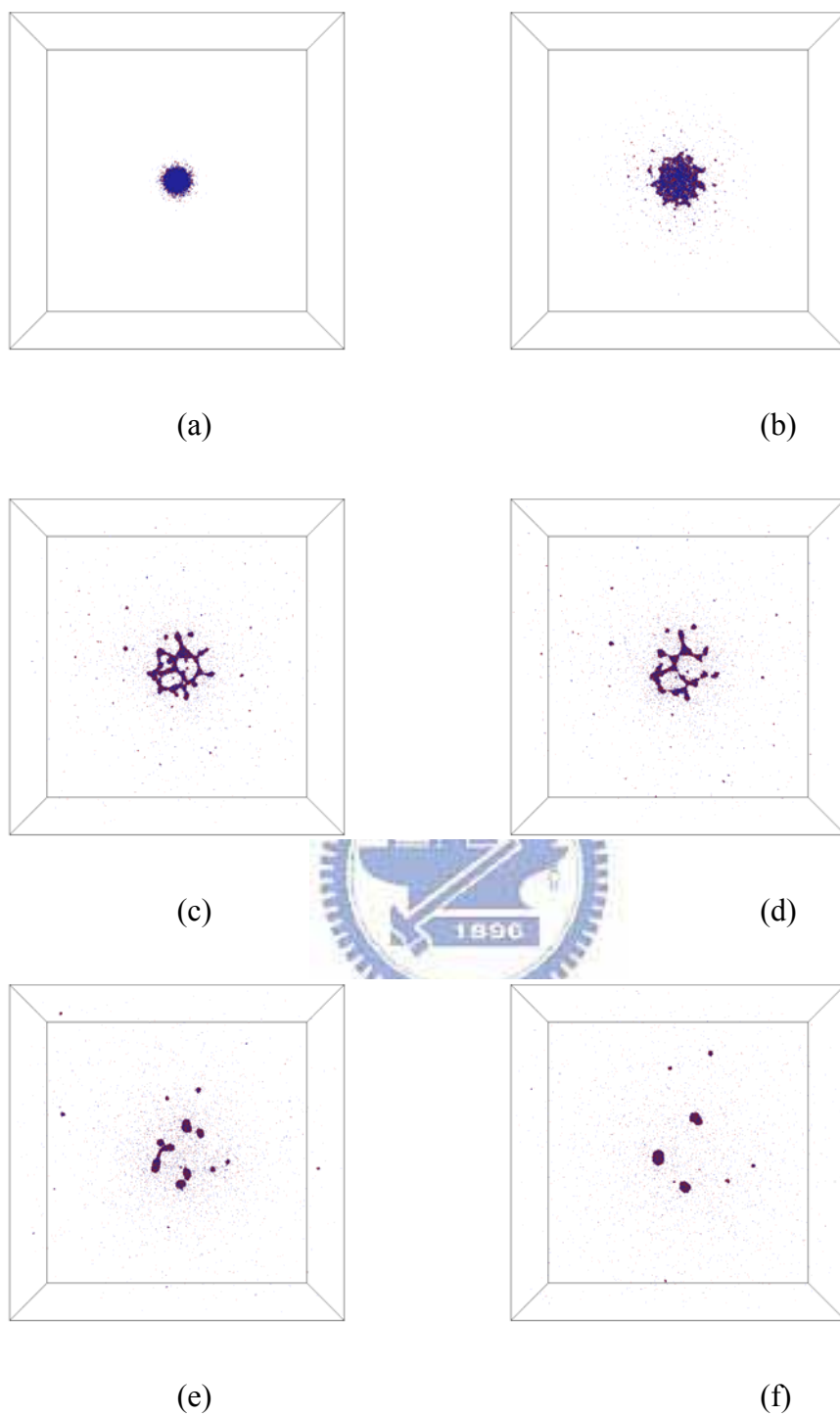
Fig. 4.9   Snapshot of droplet pair collision **under vacuum**, b=0, V=1500 *m/s*, at
(a)10ps, (b)30ps, (c)75ps, (d)100ps, (e)175ps, (f)300ps.

(a) (b)

(c) (d)

(e) (f)
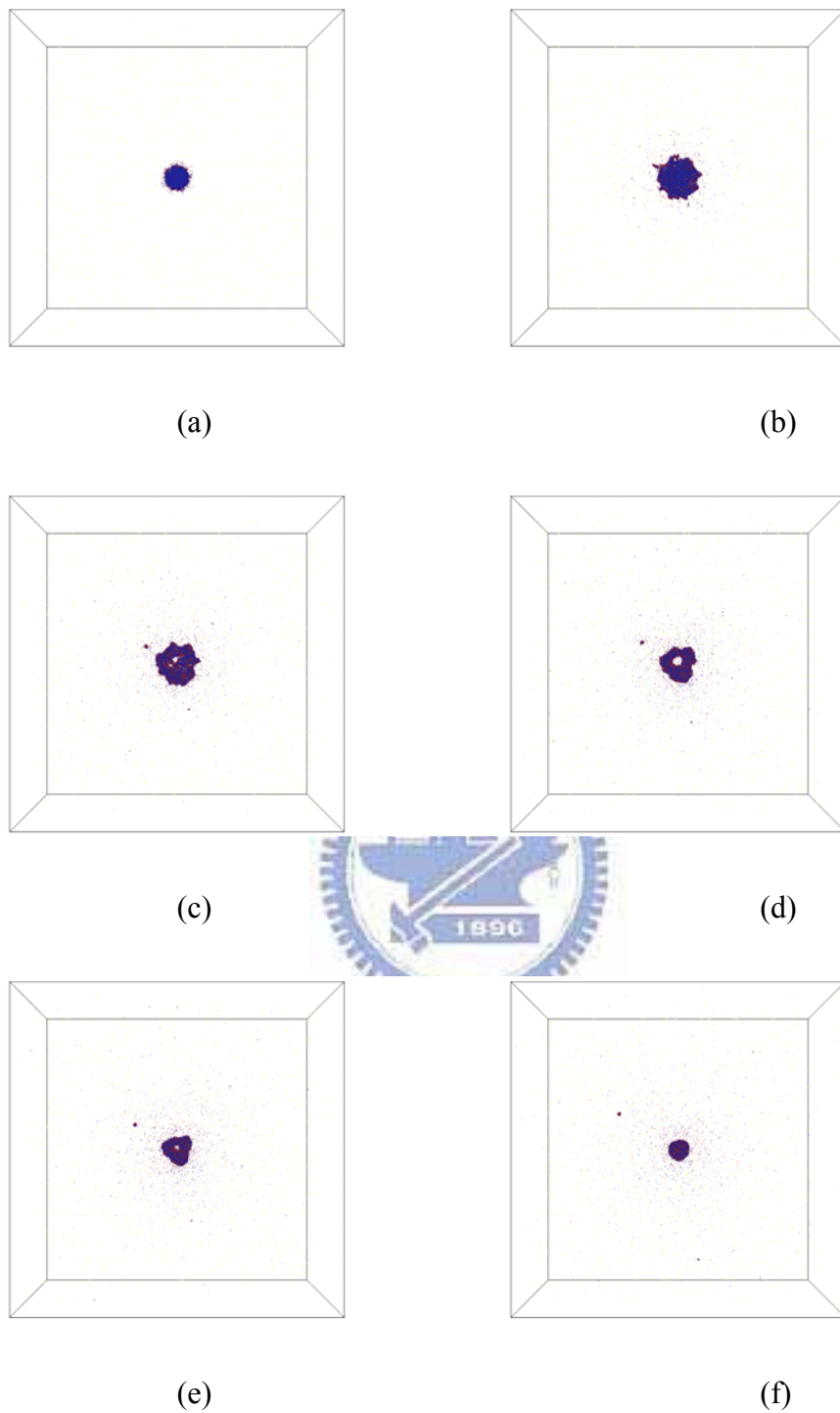
Fig. 4.10   Snapshot of droplet pair collision **under low pressurized ambient (~0.055 atm)**, b=0, V=1250 *m/s*, at (a)10ps, (b)40ps, (c)75ps, (d)100ps, (e)125ps, (f)200ps.

(a)　　　　　　　　　　　　　　　　(b)

(c)　　　　　　　　　　　　　　　　(d)

(e)　　　　　　　　　　　　　　　　(f)
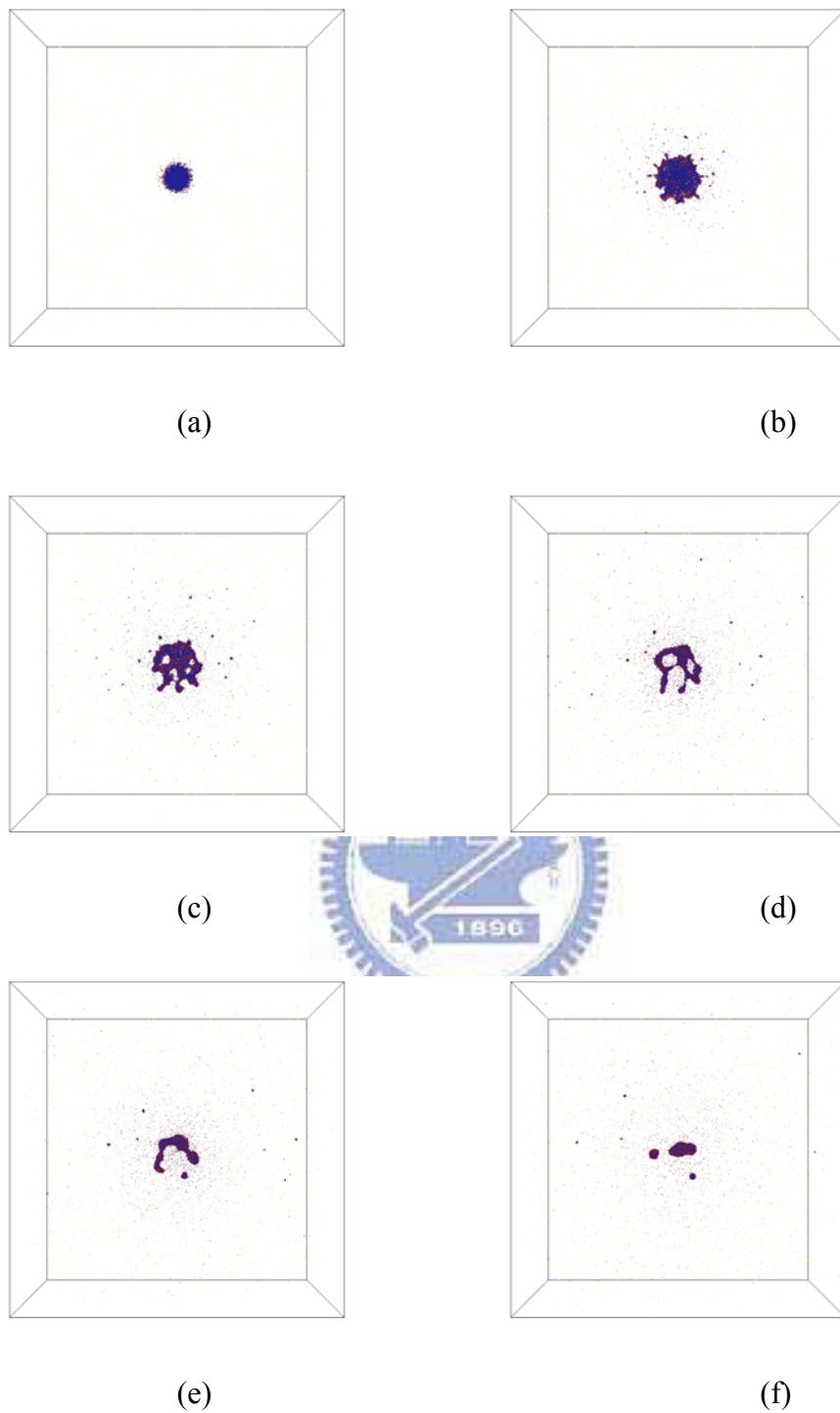
Fig. 4.11　Snapshot of droplet pair collision **under low pressurized ambient (~0.055 atm)**, b=0, V=1375 *m/s*, at (a)10ps, (b)40ps, (c)75ps, (d)100ps, (e)150ps, (f)250ps.
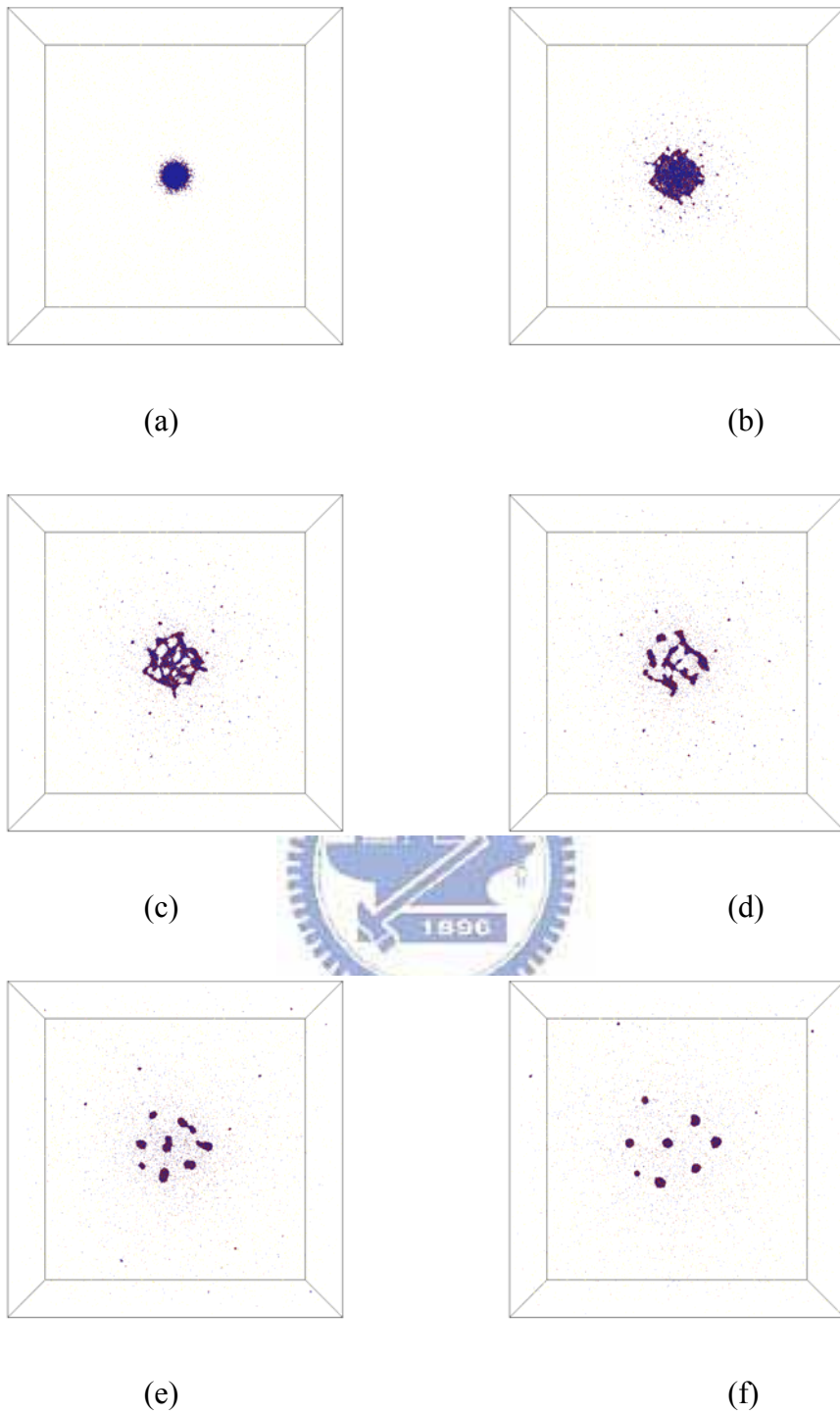
Fig. 4.12   Snapshot of droplet pair collision **under low vapor ambient**, b=0,
V=1500 *m/s*, at (a)10ps, (b)40ps, (c)60ps, (d)90ps, (e)150ps, (f)250ps.

(a)   (b)

(c)   (d)

(e)   (f)
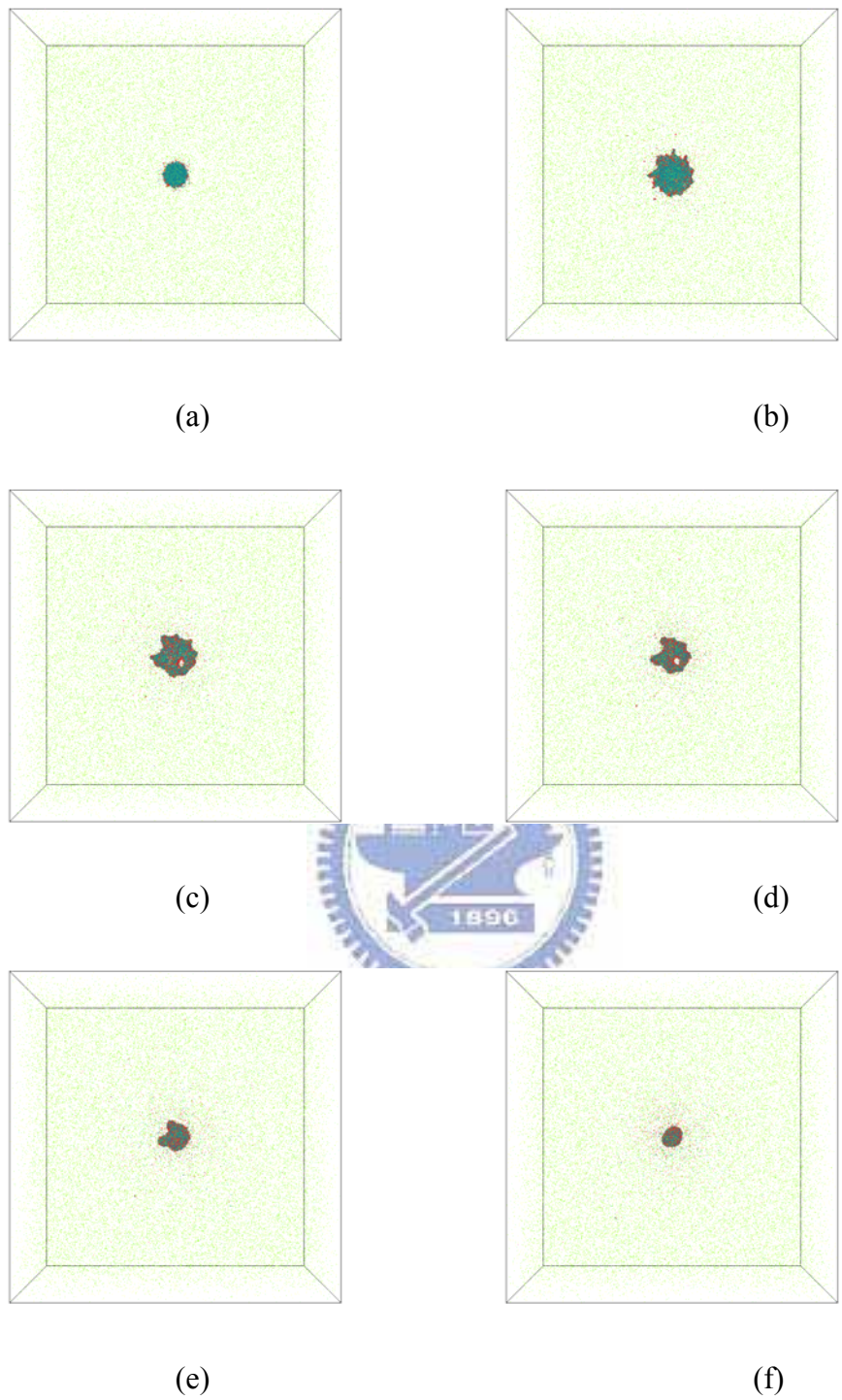
Fig. 4.13   Snapshot of droplet pair collision **under high vapor ambient**, b=0, V=1250 *m/s*, at (a)10ps, (b)40ps, (c)75ps, (d)100ps, (e)125ps, (f)200ps.

(a)   (b)

(c)   (d)

(e)   (f)
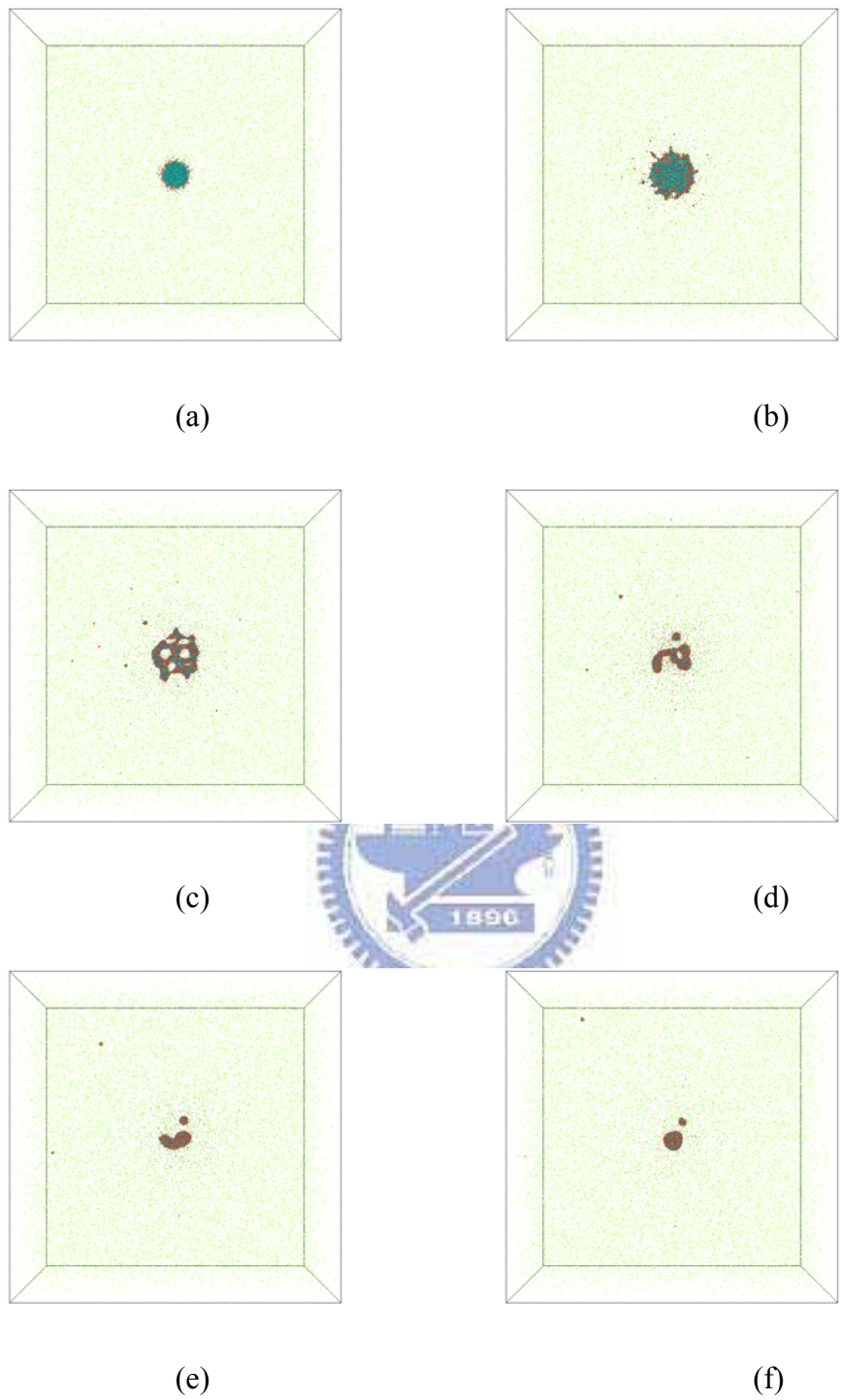
Fig. 4.14   Snapshot of droplet pair collision **under high vapor ambient**, b=0,
V=1375 *m/s*, at (a)10ps, (b)40ps, (c)75ps, (d)100ps, (e)250ps, (f)325ps.

(a)   (b)

(c)   (d)

(e)   (f)
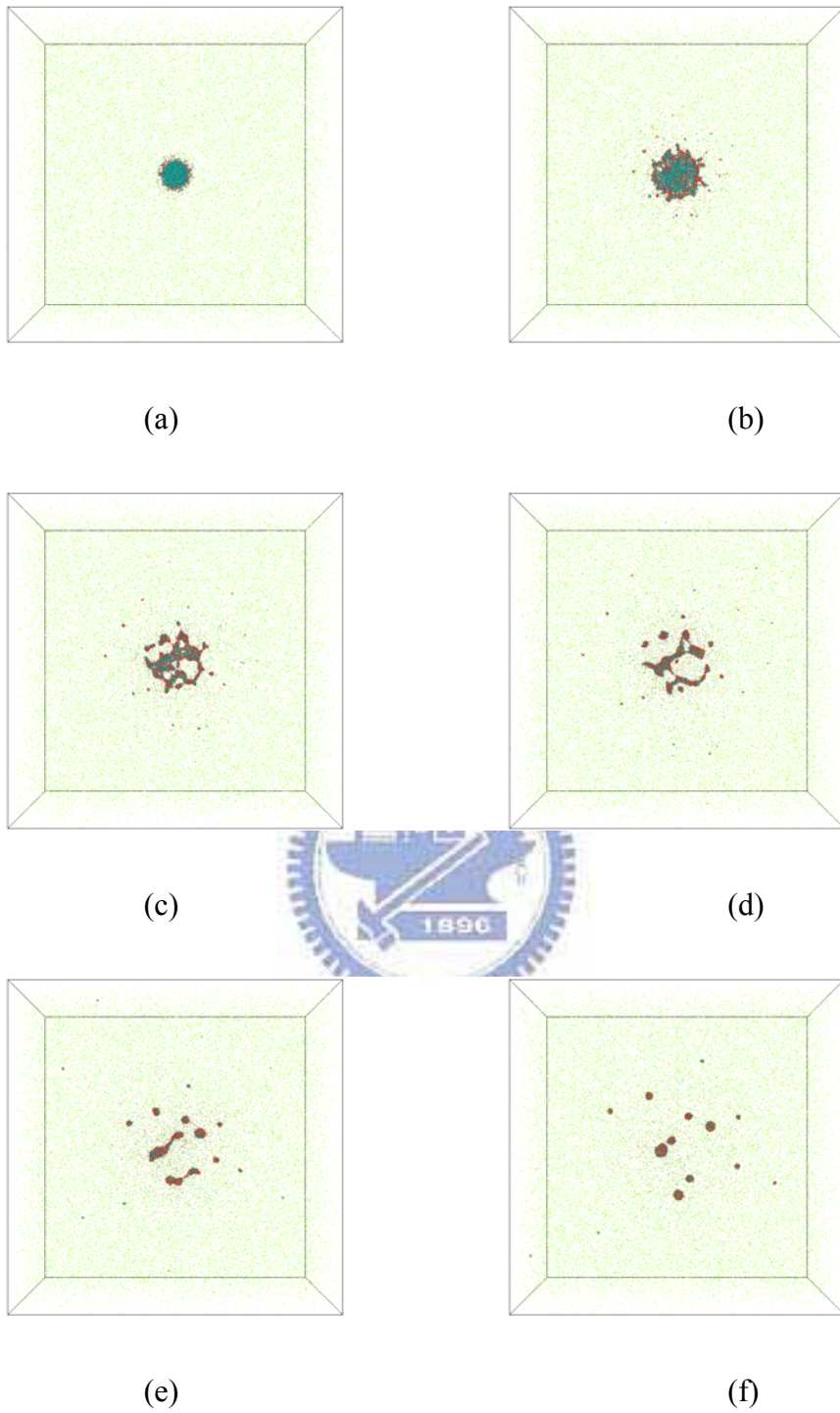
Fig. 4.15   Snapshot of droplet pair collision **under high vapor ambient**, b=0, V=1500 *m/s*, at (a)10ps, (b)40ps, (c)60ps, (d)90ps, (e)150ps, (f)250ps.
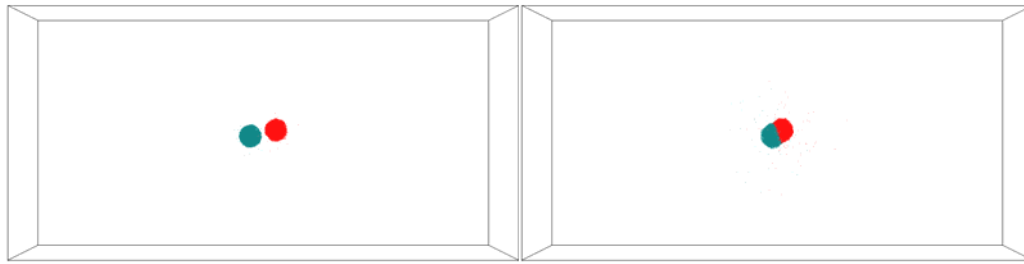
(a)   (b)
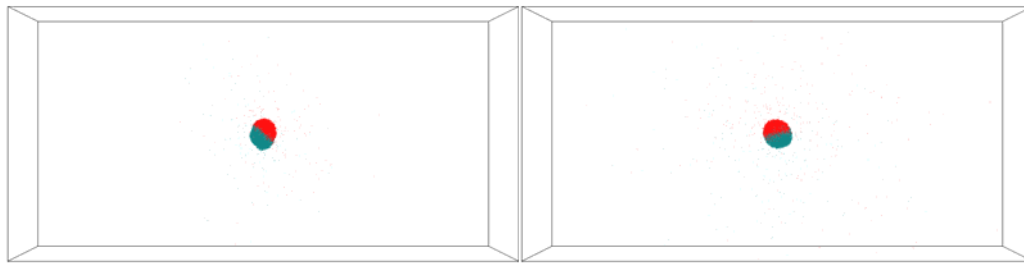
(c)   (d)
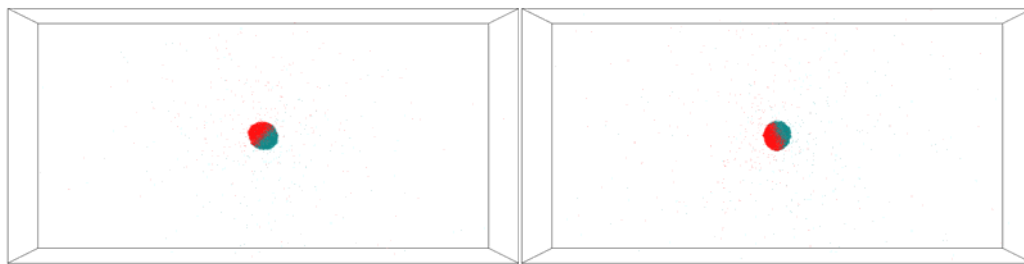
(e)   (f)

Fig. 4.2   Snapshot of droplet pair collision **under vacuum**, b=0.25, V=250 *m/s*, at
(a)10ps, (b)50ps, (c)100ps, (d)200ps, (e)250ps, (f)375ps. This case is classified in
Coalescence regime.

(a)   (b)

(c)   (d)

(e)   (f)
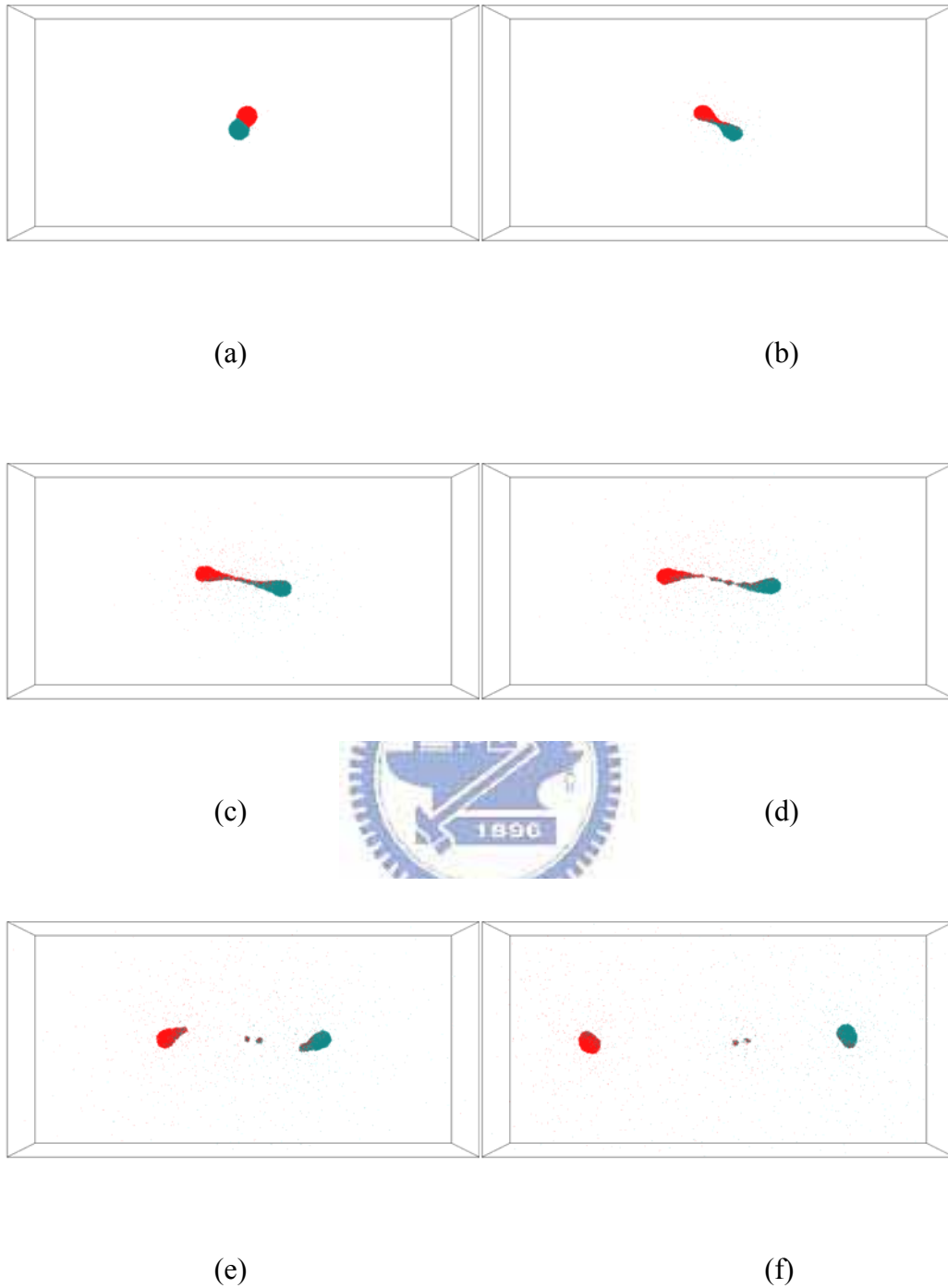
Fig. 4.3 Snapshot of droplet pair collision **under vacuum**, b=0.625, V=1000 *m/s*, at (a)10ps, (b)40ps, (c)75ps, (d)100ps, (e)150ps, (f)250ps. This case is classified in **Stretching Separation** regime.
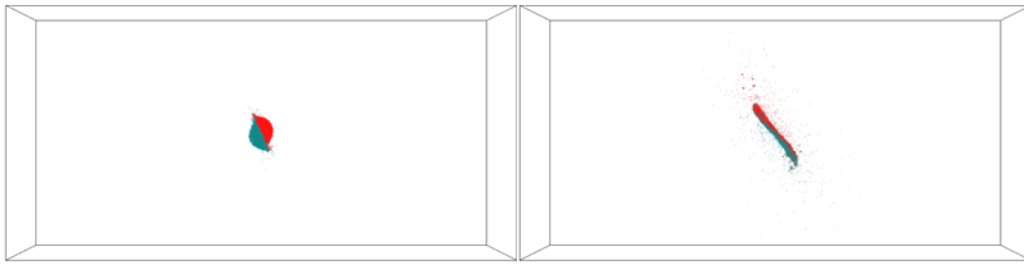
(a)

(b)
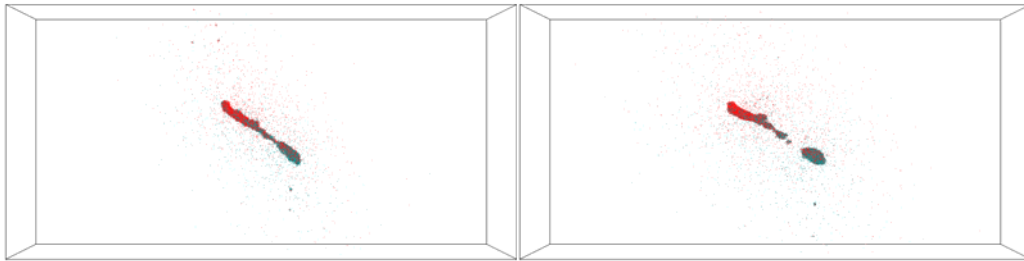
(c)

(d)
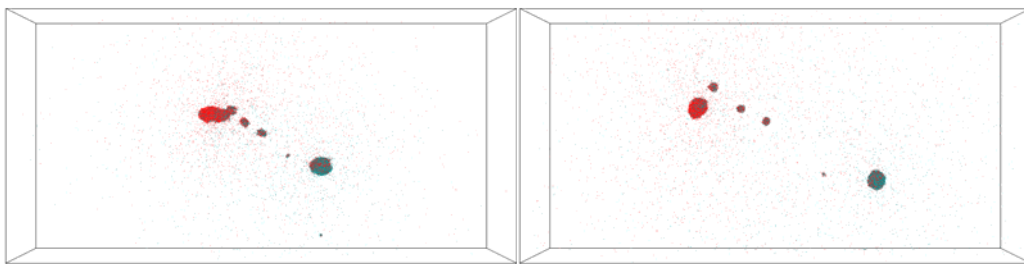
(e)

(f)

Fig. 4.4   Snapshot of droplet pair collision **under vacuum** b=0.25, V=1375 *m/s*, at (a)10ps, (b)40ps, (c)75ps, (d)100ps, (e)150ps, (f)250ps. This case is classified in **Shattering** regime.

(a)   (b)

(c)   (d)

(e)   (f)
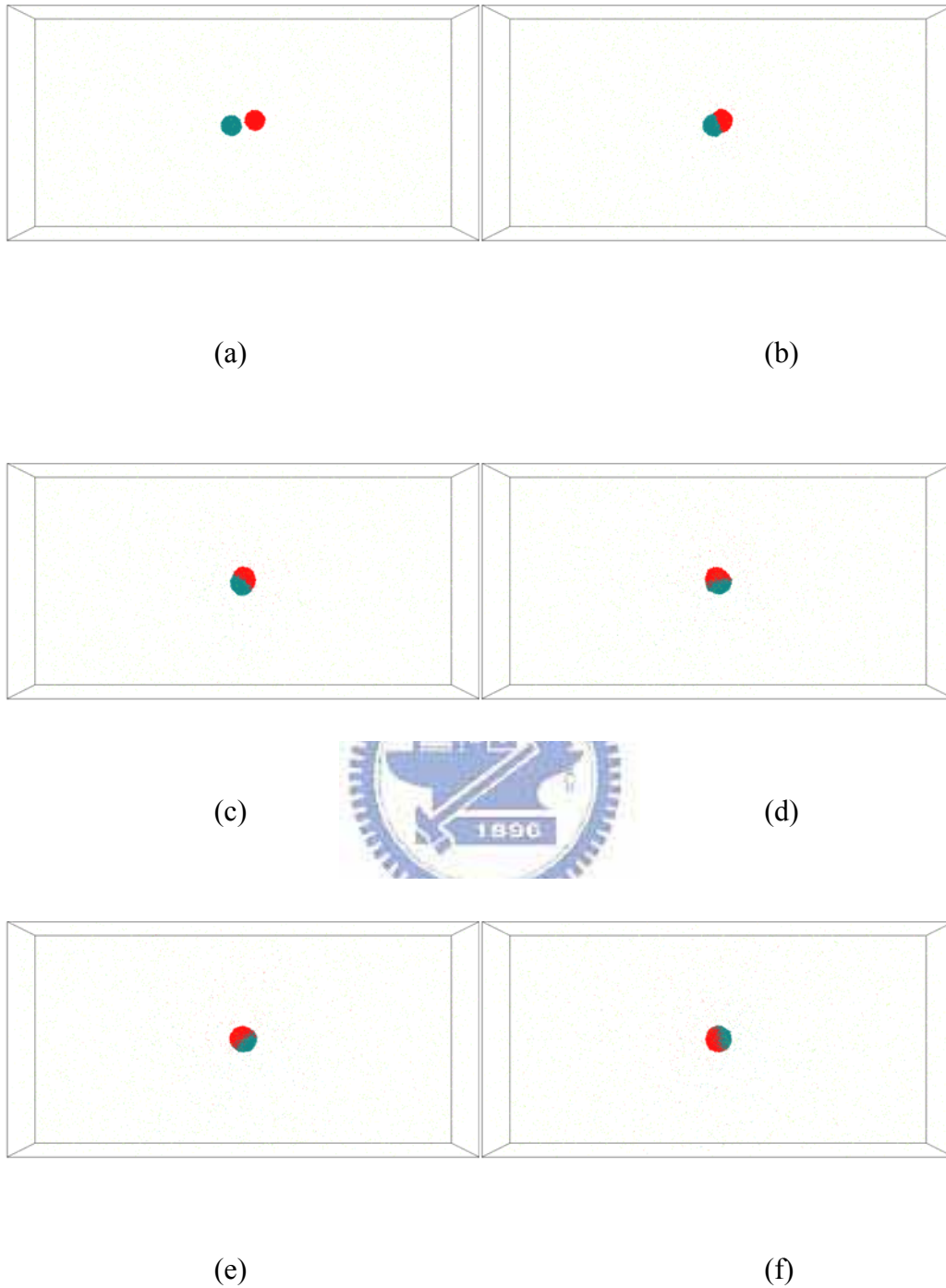
Fig. 4.5   Snapshot of droplet pair collision **under low pressurized ambient**,
b=0.25, V=250 *m/s*, at (a)10ps, (b)50ps, (c)100ps, (d)200ps, (e)250ps, (f)375ps. This
case is classified in **Coalescence** regime.

(a)   (b)

(c)   (d)

(e)   (f)
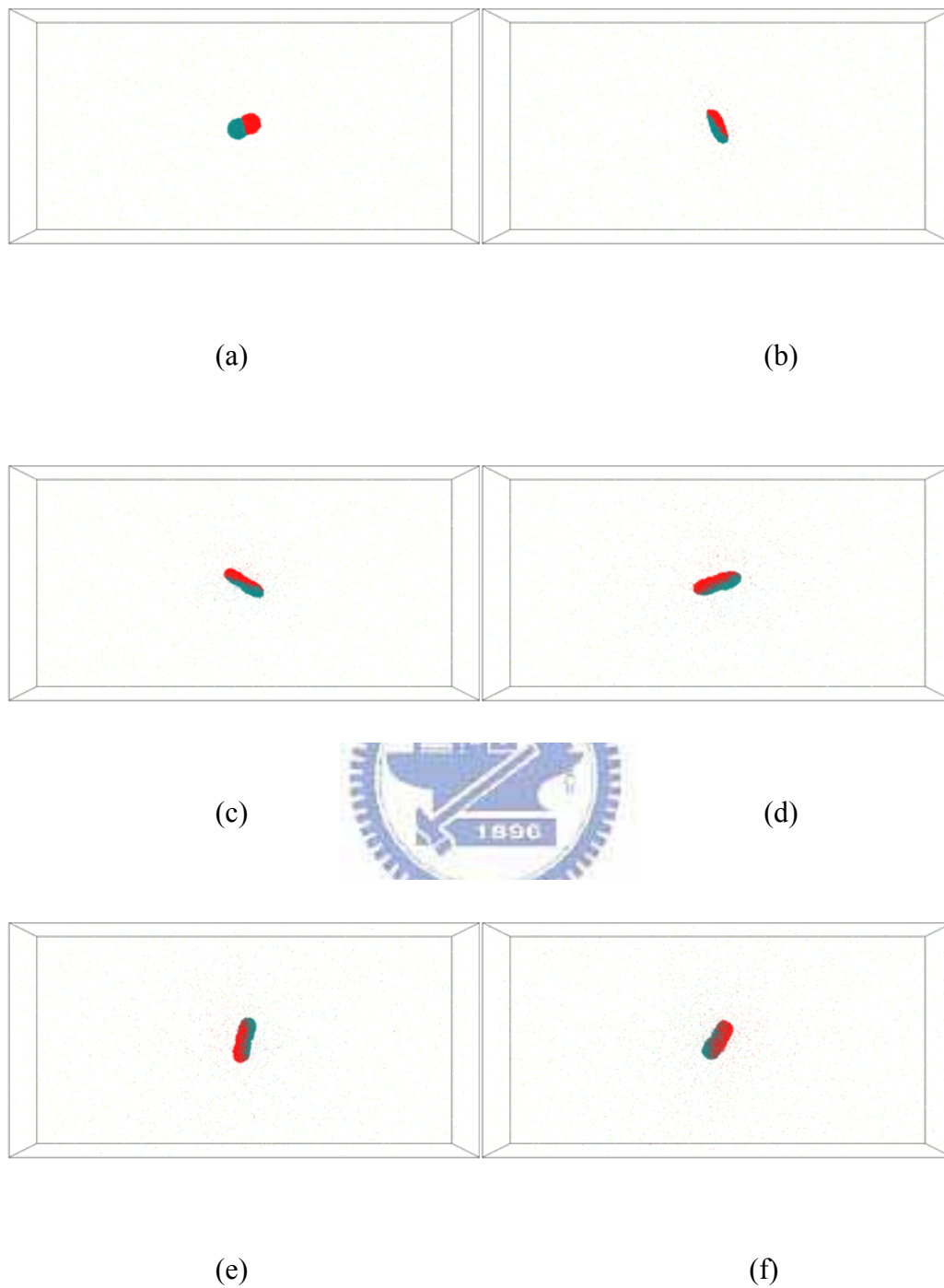
Fig. 4.20   Snapshot of droplet pair collision **under low pressurized ambient**, b=0.25, V=750 *m/s*, at (a)10ps, (b)40ps, (c)75ps, (d)150ps, (e)250ps, (f)500ps. This case is classified in **Stretching Coalescence** regime.

(a)   (b)

(c)   (d)

(e)   (f)
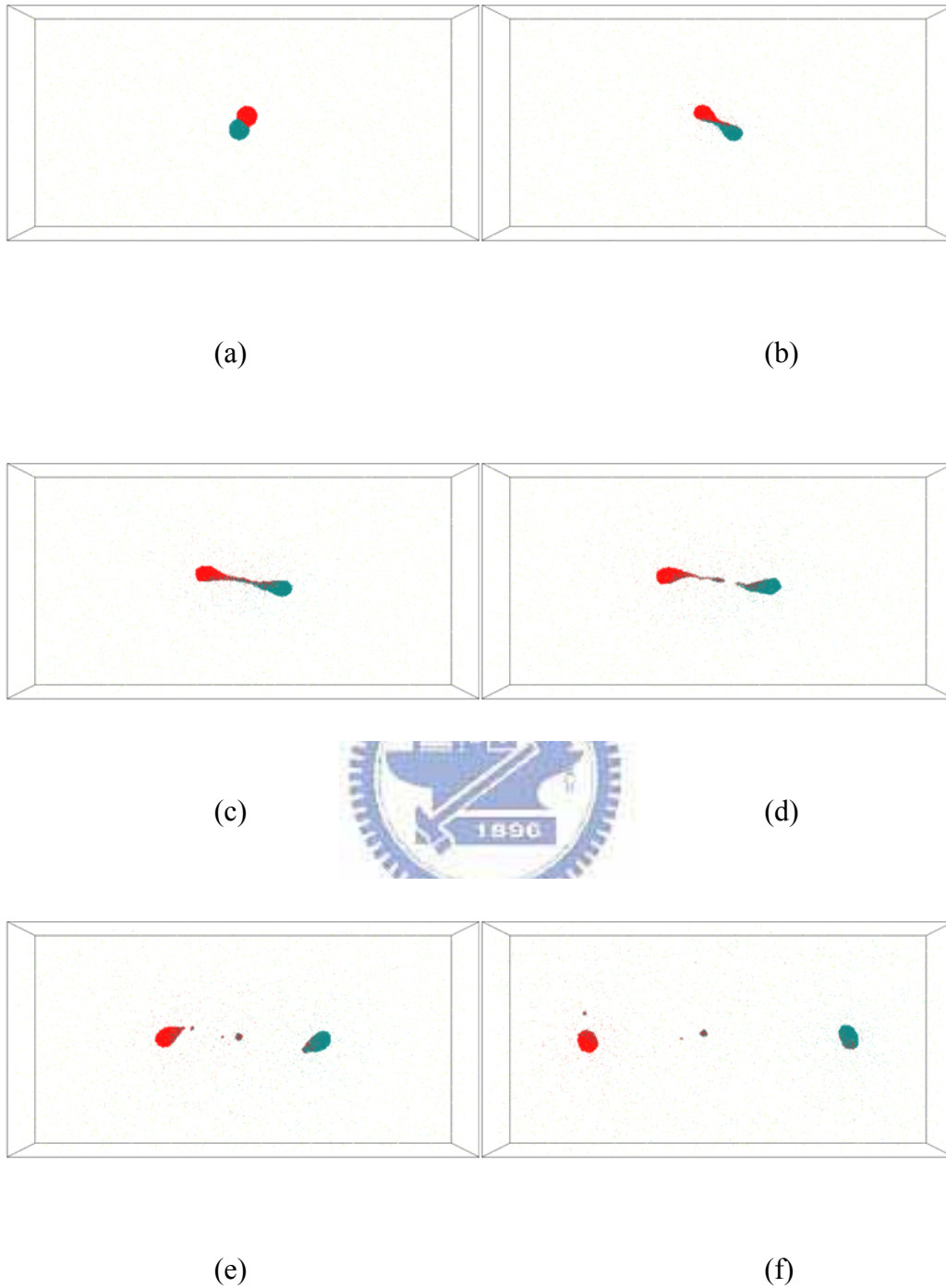
Fig. 4.21 Snapshot of droplet pair collision **under low pressurized ambient**, b=0.625, V=1000*m/s*, at (a)10ps, (b)40ps, (c)75ps, (d)100ps, (e)150ps, (f)250ps. This case is classified in **Stretching Separation** regime.

(a)   (b)

(c)   (d)

(e)   (f)
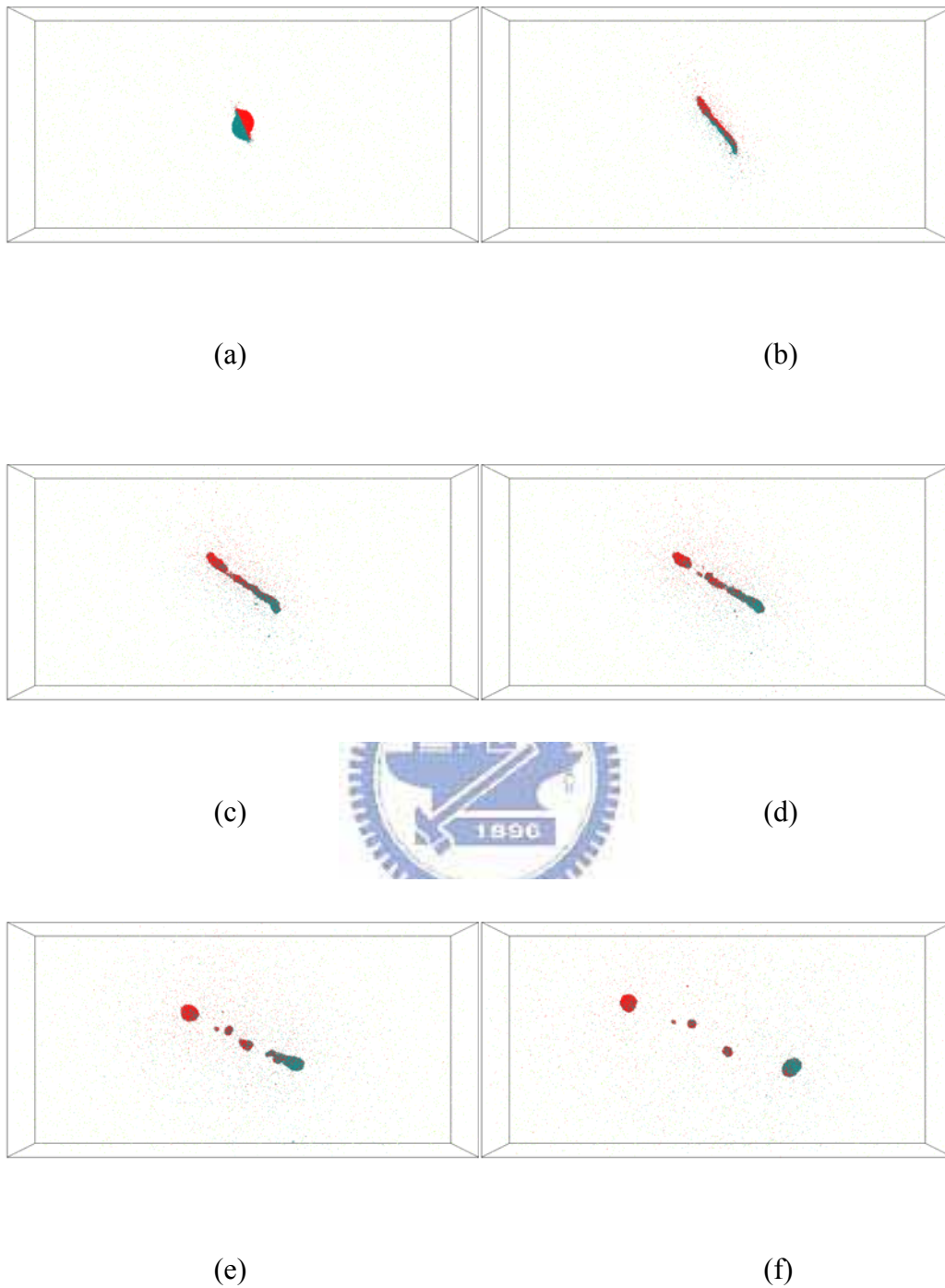
Fig. 4.22   Snapshot of droplet pair collision **under low pressurized ambient**, b=0.
25, V=1375*m/s*, at (a)10ps, (b)40ps, (c)75ps, (d)100ps, (e)150ps, (f)250ps. This case
is classified in **Shattering** regime.

(a)   (b)

(c)   (d)

(e)   (f)
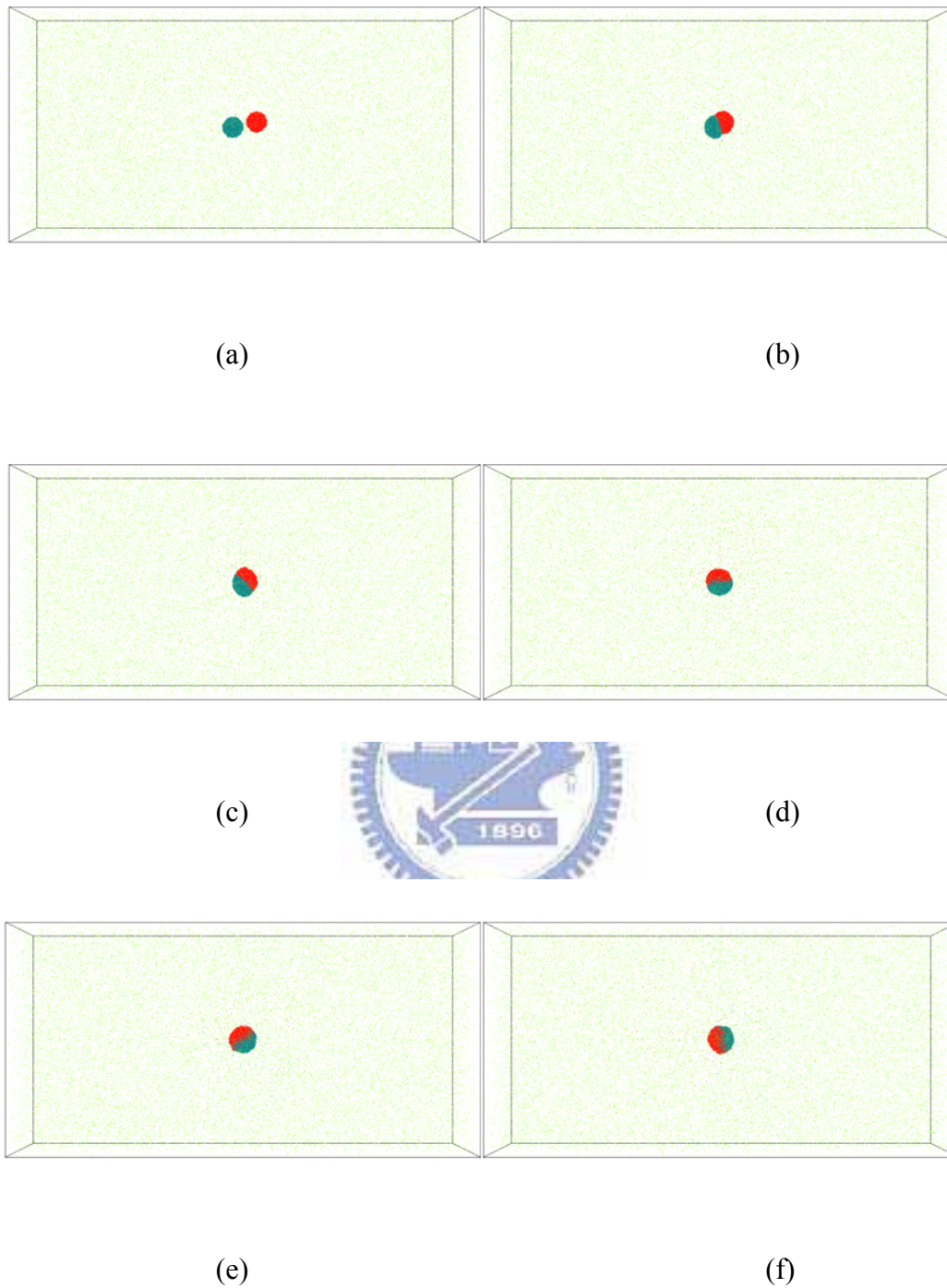
Fig. 4.23　Snapshot of droplet pair collision **under high pressurized ambient**, b=0.25, V=250 *m/s*, at (a)10ps, (b)50ps, (c)100ps, (d)200ps, (e)250ps, (f)375ps. This case is classified in **Coalescence** regime.

(a)   (b)

(c)   (d)

(e)   (f)
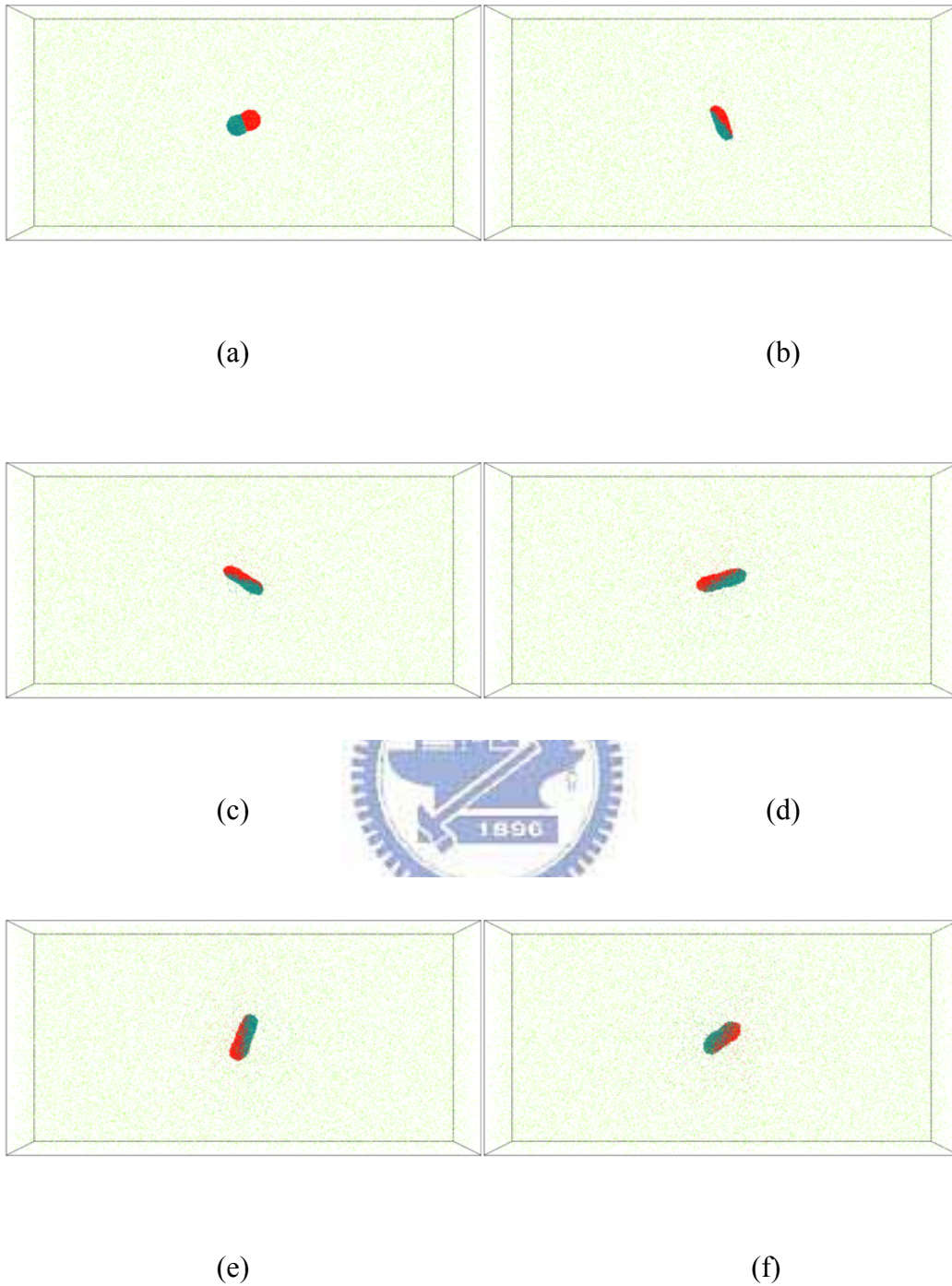
Fig. 4.24   Snapshot of droplet pair collision **under high pressurized ambient**, b=0.25, V=750 *m/s*, at (a)10ps, (b)40ps, (c)75ps, (d)150ps, (e)250ps, (f)500ps. This case is classified in **Stretching Coalescence** regime.
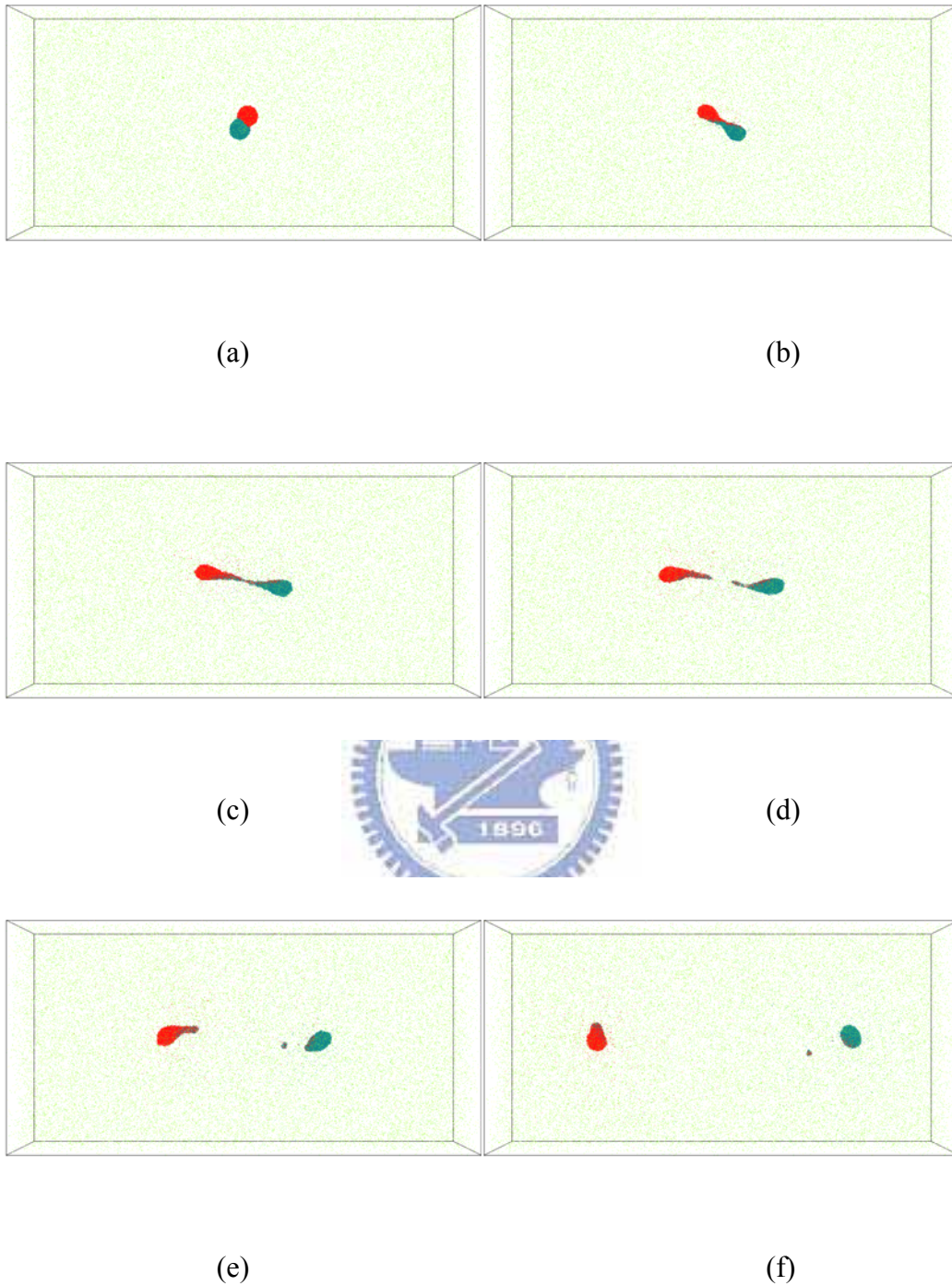
Fig. 4.25　Snapshot of droplet pair collision **under high pressurized ambient**, b=0.625, V=1000*m/s*, at (a)10ps, (b)40ps, (c)75ps, (d)100ps, (e)150ps, (f)250ps. This case is classified in **Stretching Separation** regime.
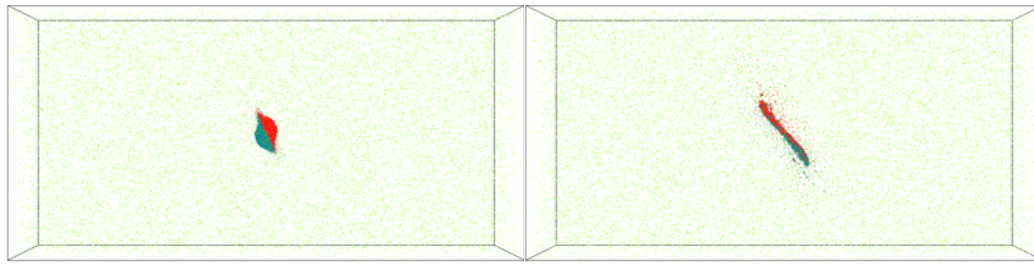
(a)

(b)
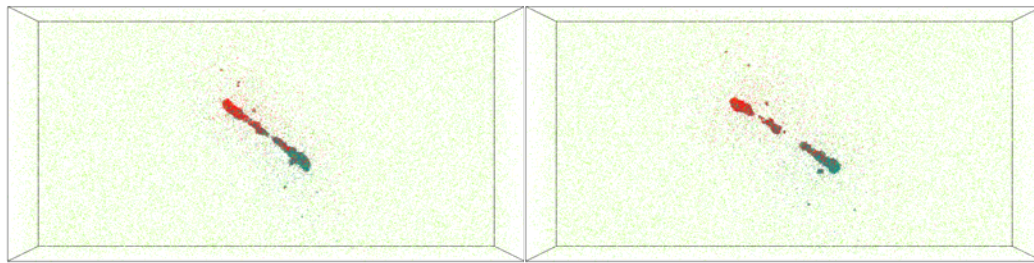
(c)

(d)
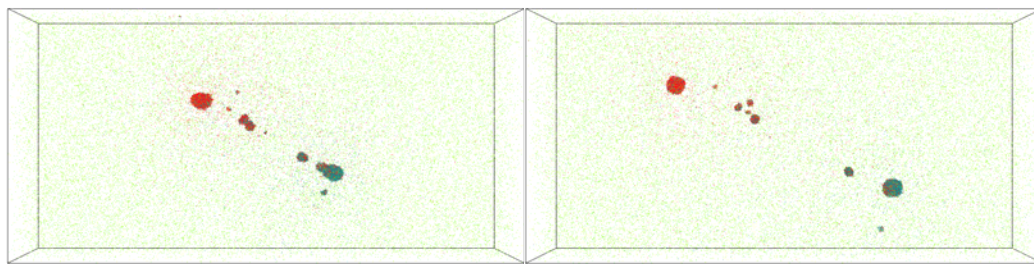
(e)

(f)

Fig. 4.26 Snapshot of droplet pair collision **under high pressurized ambient**, b=0.25, V=1500*m/s*, at (a)10ps, (b)40ps, (c)75ps, (d)100ps, (e)150ps, (f)250ps. This case is classified in **Shattering** regime.
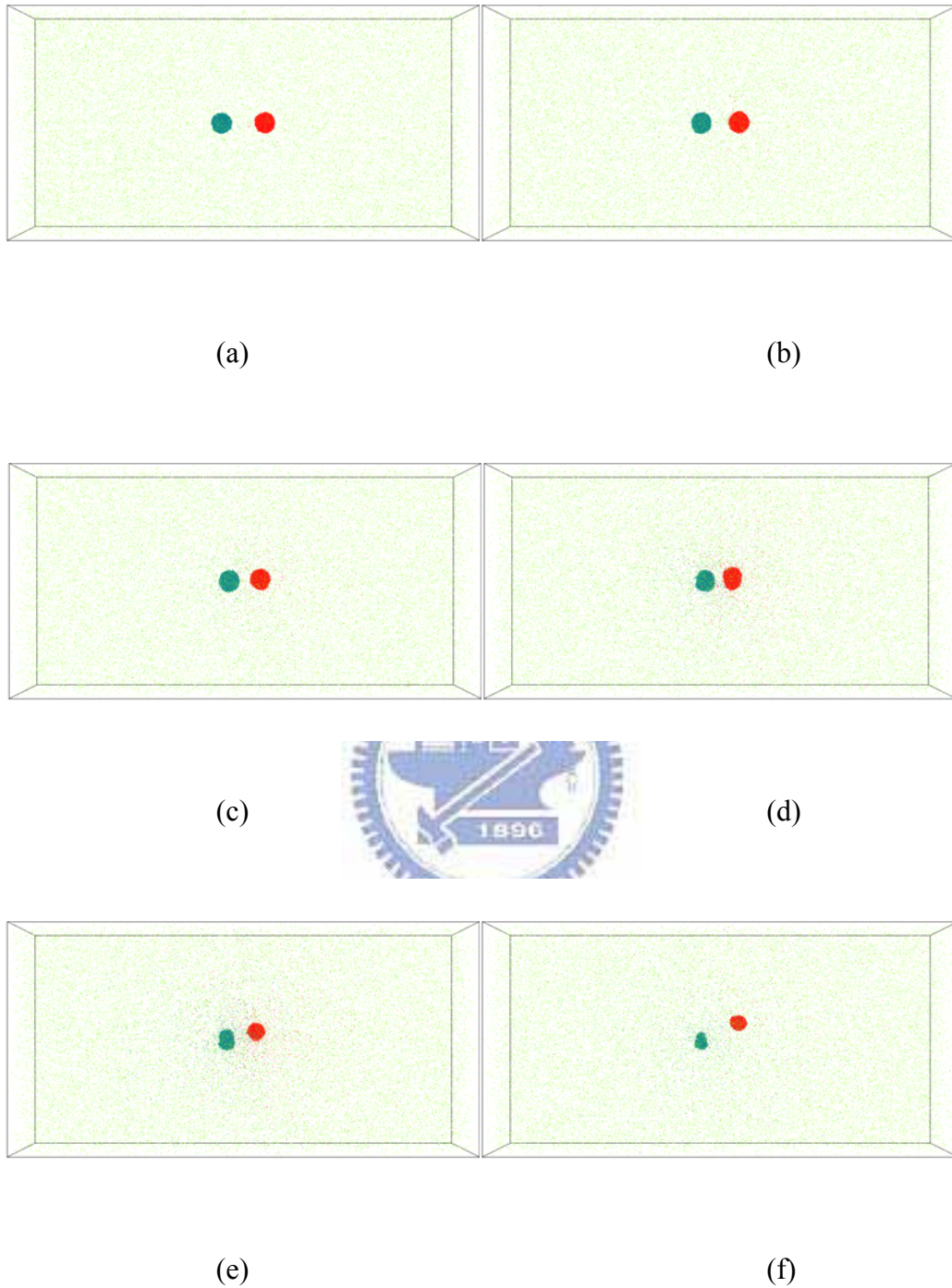
Fig. 4.27　Snapshot of droplet pair collision **under high pressurized ambient**, b=0, V=10 *m/s*, at (a)25ps, (b)250ps, (c)500ps, (d)750ps, (e)1000ps, (f)1250ps. This case is classified in **Bounce** regime.
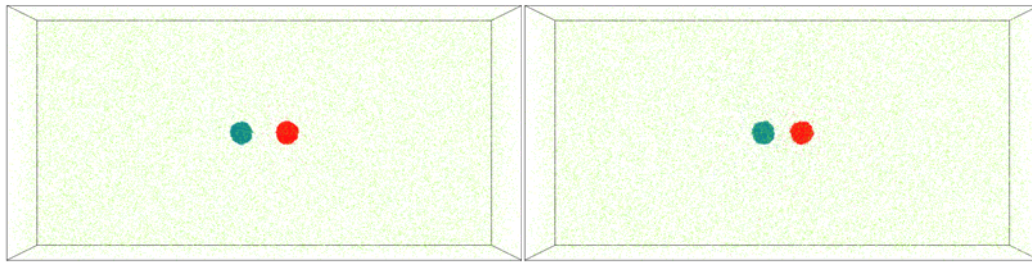
(a)   (b)
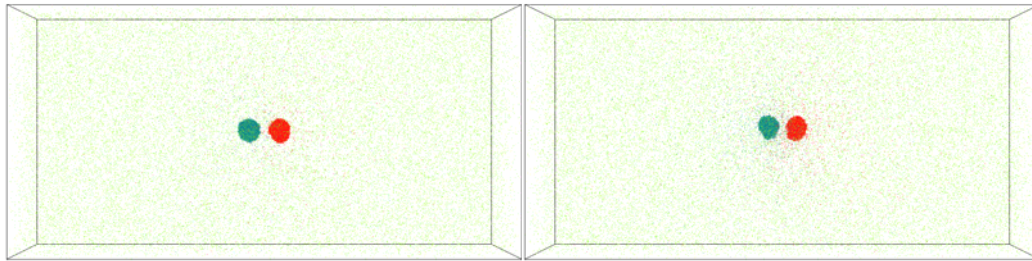
(c)   (d)
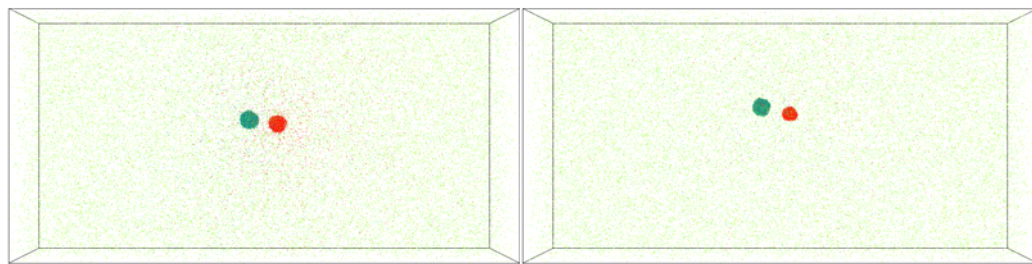
(e)   (f)

Fig. 4.28   Snapshot of droplet pair collision **under high pressurized ambient**, b=0, V=30 *m/s*, at (a)25ps, (b)250ps, (c)500ps, (d)750ps, (e)1000ps, (f)1250ps. This case is classified in **Bounce** regime.

(a)　　　　　　　　　　　　　　　　(b)

(c)　　　　　　　　　　　　　　　　(d)

(e)　　　　　　　　　　　　　　　　(f)
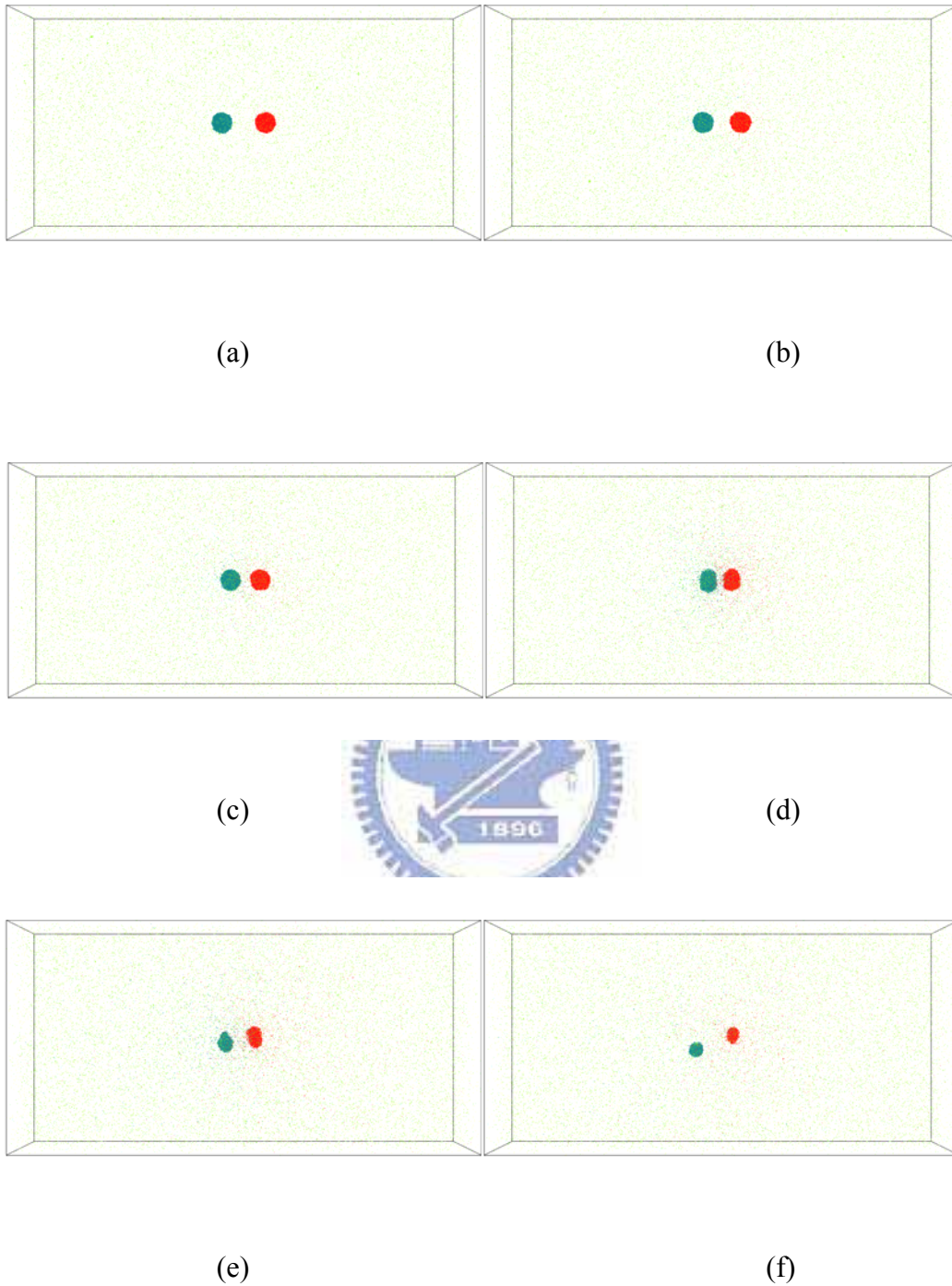
Fig. 4.29　Snapshot of droplet pair collision **under high pressurized ambient** (0.55 atm, **T=324K**), b=0, V=10 *m/s*, at (a)25ps, (b)250ps, (c)500ps, (d)750ps, (e)1000ps, (f)1200ps. This case is classified in **Bounce** regime.

(a)   (b)

(c)   (d)

(e)   (f)
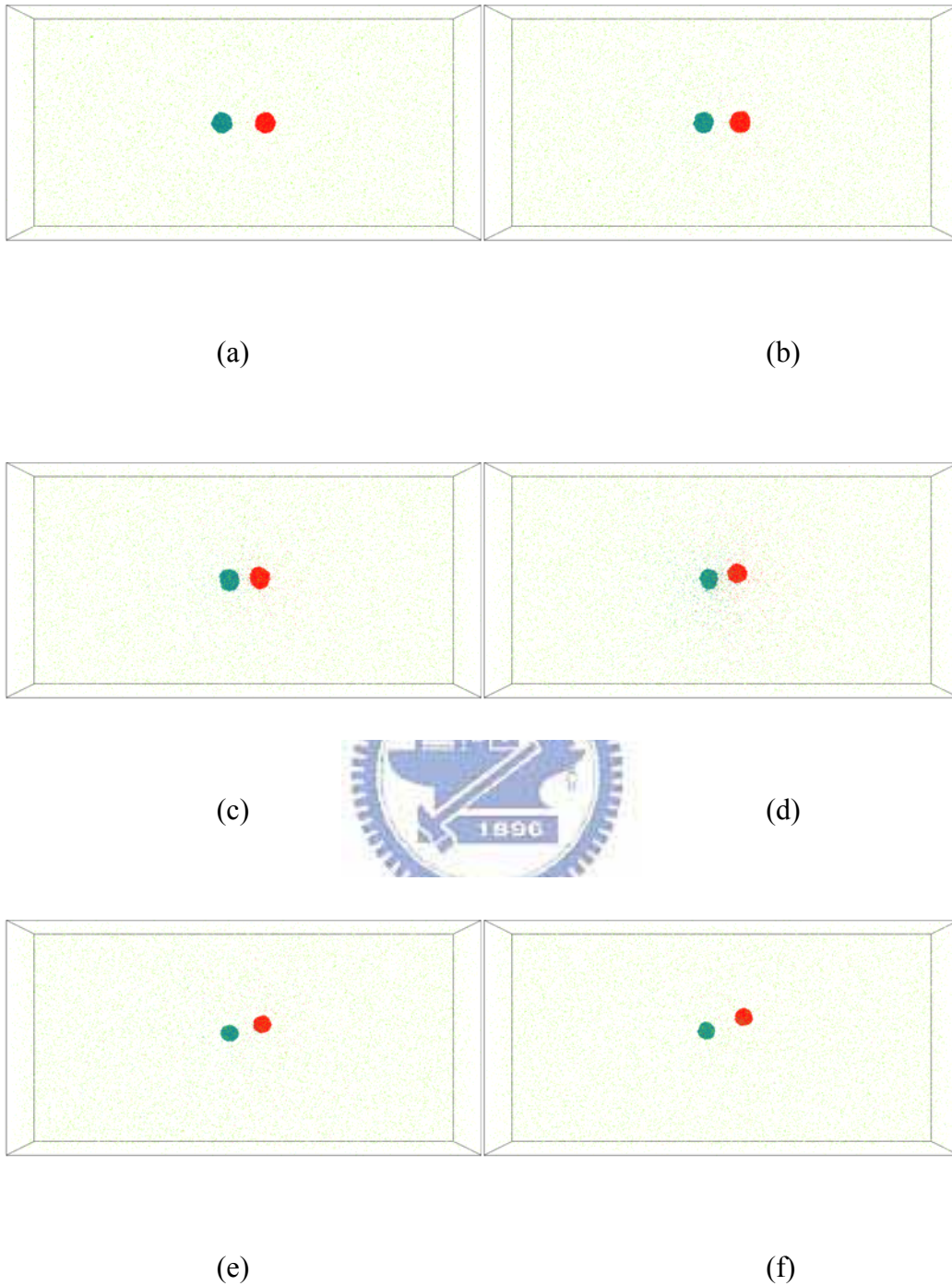
Fig. 4.30   Snapshot of droplet pair collision **under high pressurized ambient** (0.55 atm, **T=324K**), b=0, V=30 *m/s*, at (a)25ps, (b)250ps, (c)500ps, (d)750ps, (e)1000ps, (f)1250ps. This case is classified in **Bounce** regime.
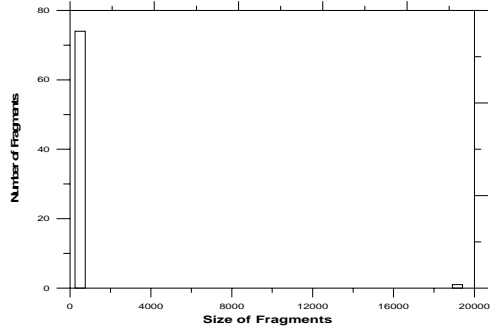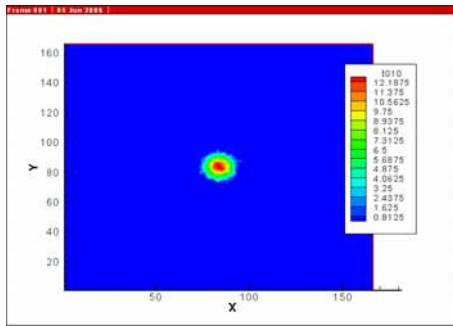
(a)
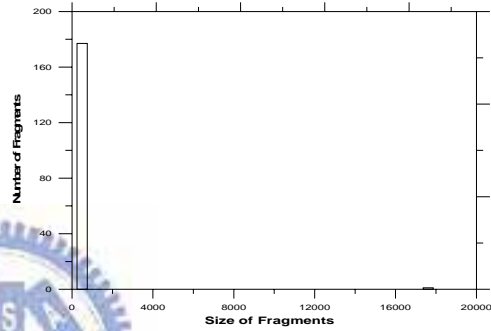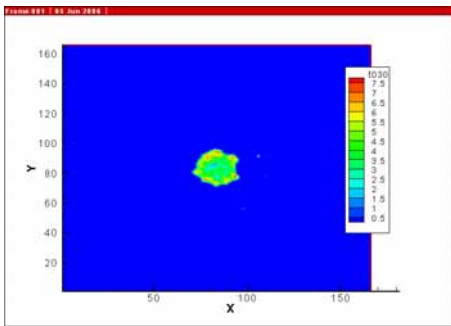
(b)
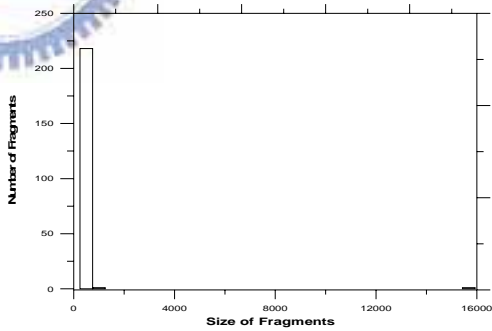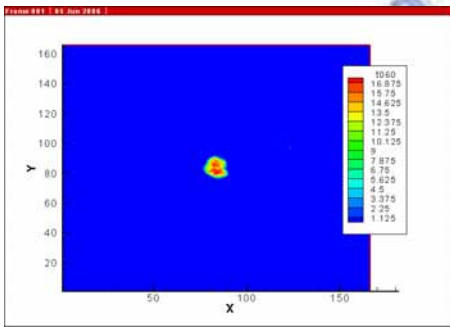
(c)

Fig. 4.31　Snapshot of density contour and clusters size distribution **under vacuum**, b=0, V=1250 *m/s*, at (a)25ps, (b)75ps, (b)150ps. This case is classified in **Stretching Coalescence** regime.
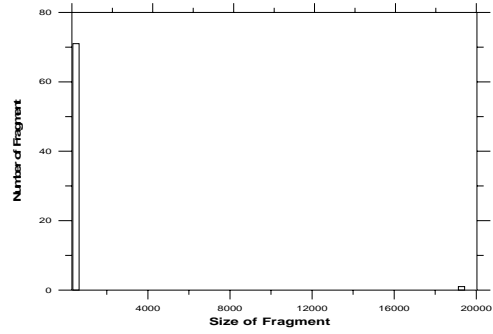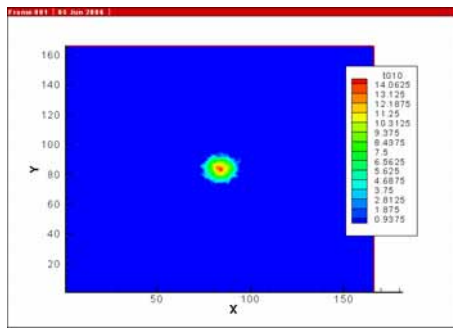
(a)
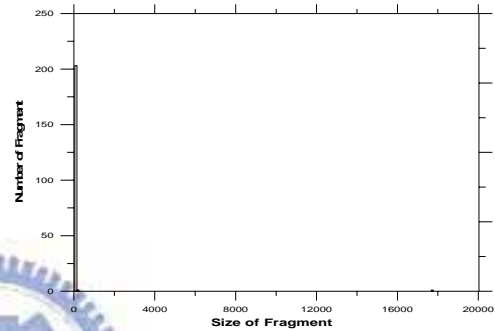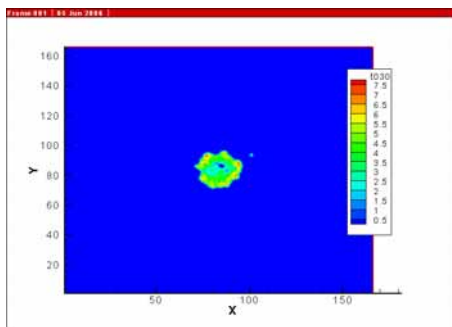
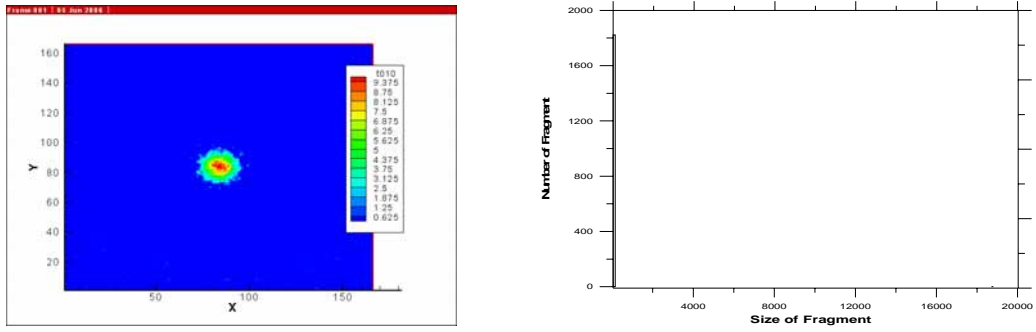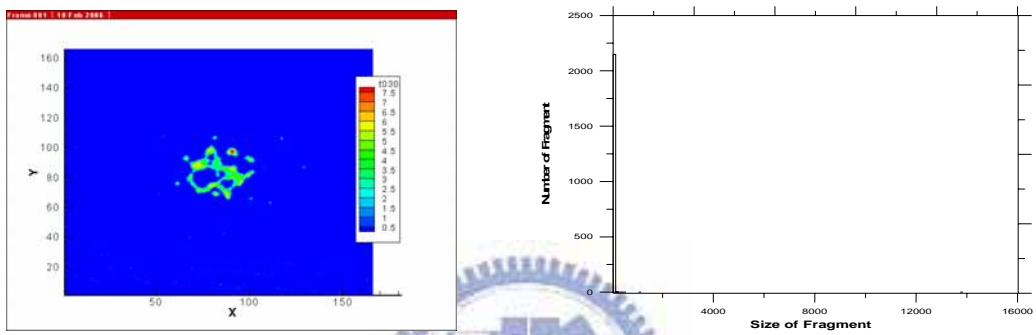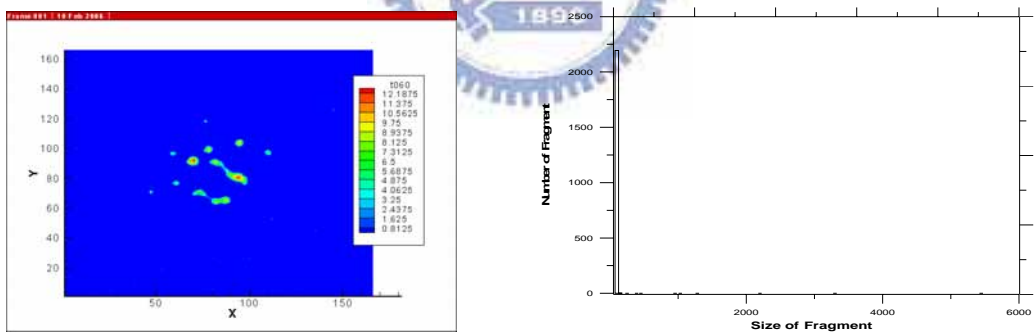

(b)
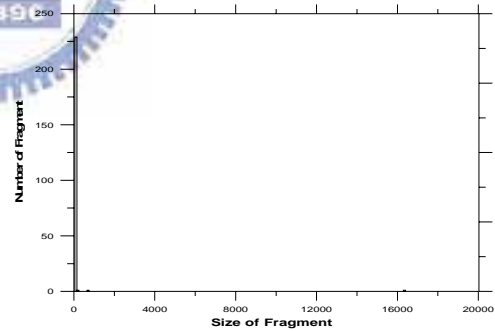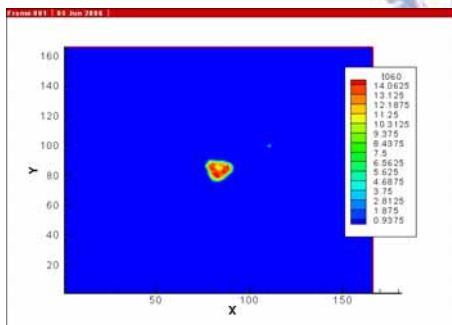
(c)

Fig. 4.32   Snapshot of density contour and clusters size distribution **under low pressurized ambient**, b=0, V=1250 *m/s*, at (a)25ps, (b)75ps, (b)150ps. This case is classified in **Stretching Coalescence** regime.
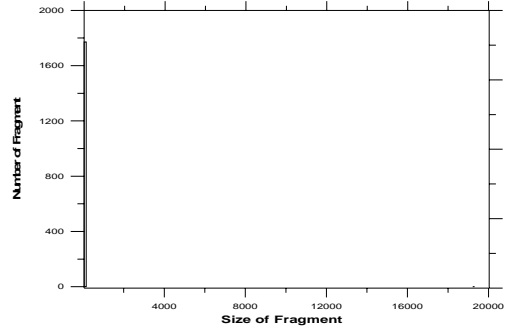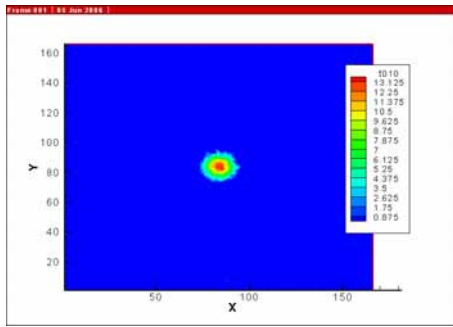
(a)
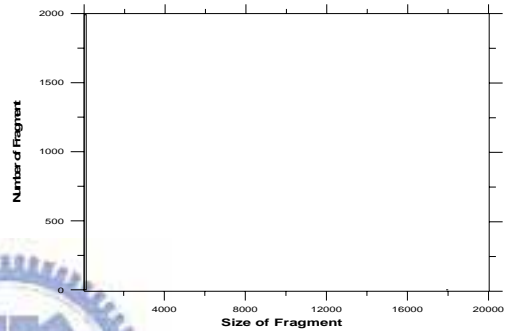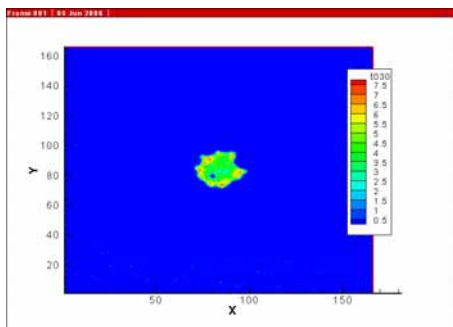
(b)
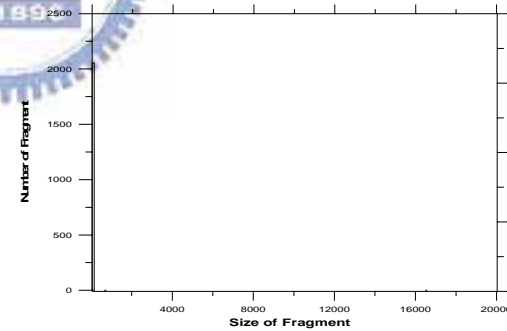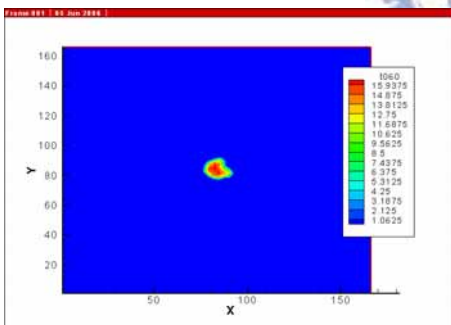
(c)

Fig. 4.33   Snapshot of density contour and clusters size distribution **under high pressurized ambient**, b=0, V=1250 *m/s*, at (a)25ps, (b)75ps, (b)150ps. This case is classified in **Stretching Coalescence** regime.
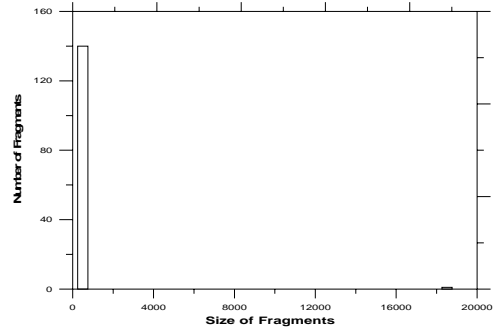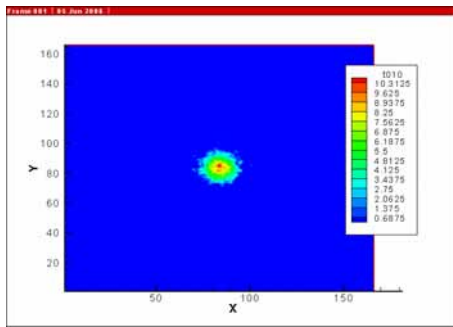
(a)
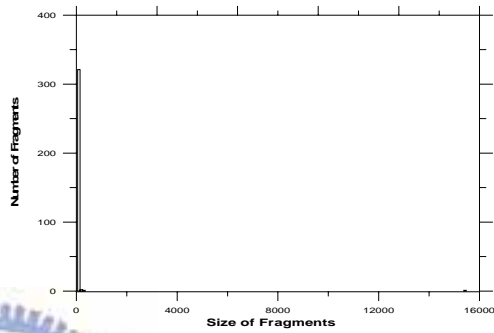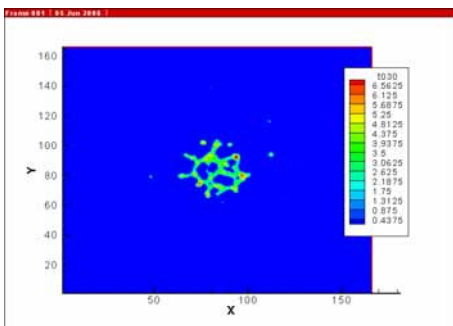
(b)
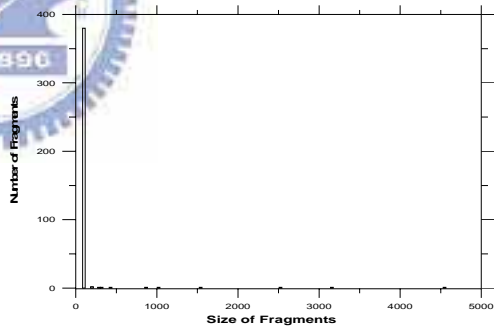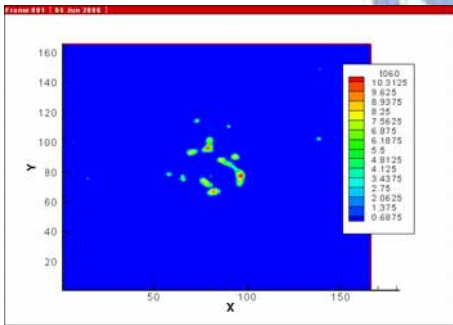
(c)

Fig. 4.34   Snapshot of density contour and clusters size distribution **under vacuum**, b=0, V=1500 *m/s*, at (a)25ps, (b)75ps, (b)150ps. This case is classified in **Shattering** regime.

121
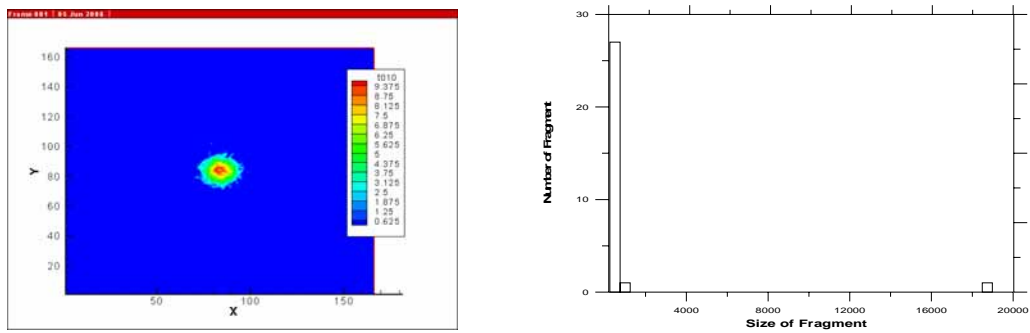
(a)
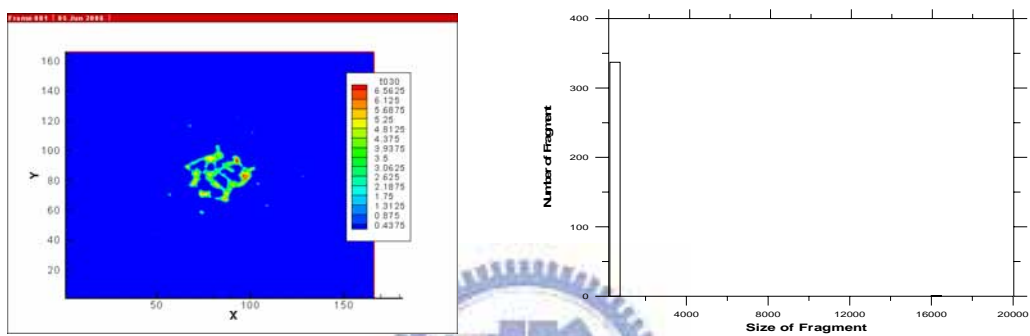
(b)
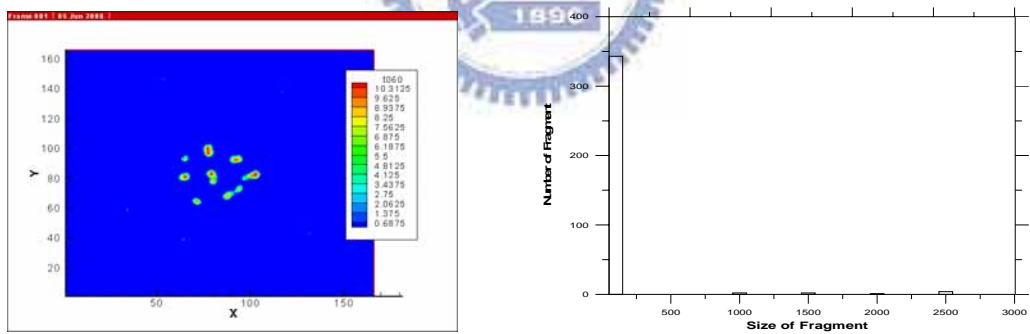
(c)

Fig. 4.35 Snapshot of density contour and clusters size distribution **under low pressurized ambient**, b=0, V=1500 *m/s*, at (a)25ps, (b)75ps, (b)150ps. This case is classified in **Shattering** regime.
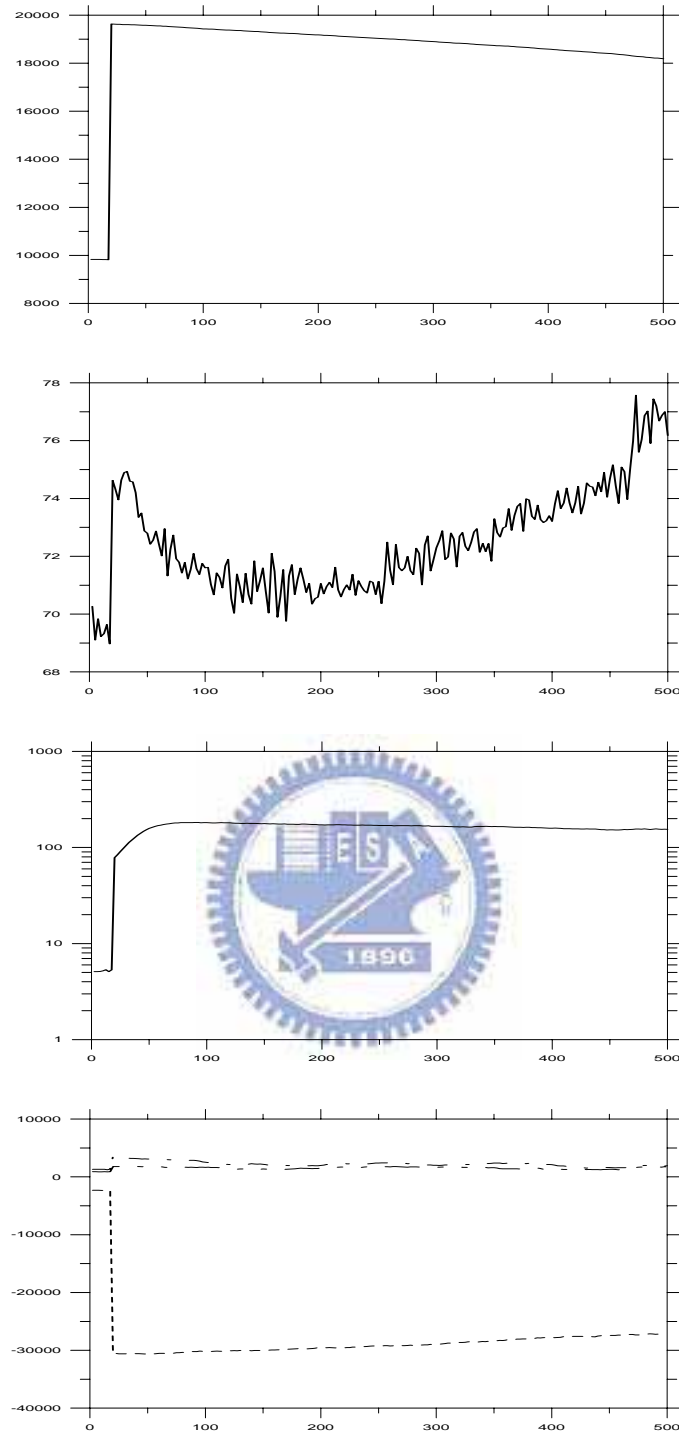
(a)

(b)

(c)

Fig. 4.36   Snapshot of density contour and clusters size distribution **under high pressurized ambient**, b=0, V=1500 *m/s*, at (a)25ps, (b)75ps, (b)150ps. This case is classified in **Shattering** regime.
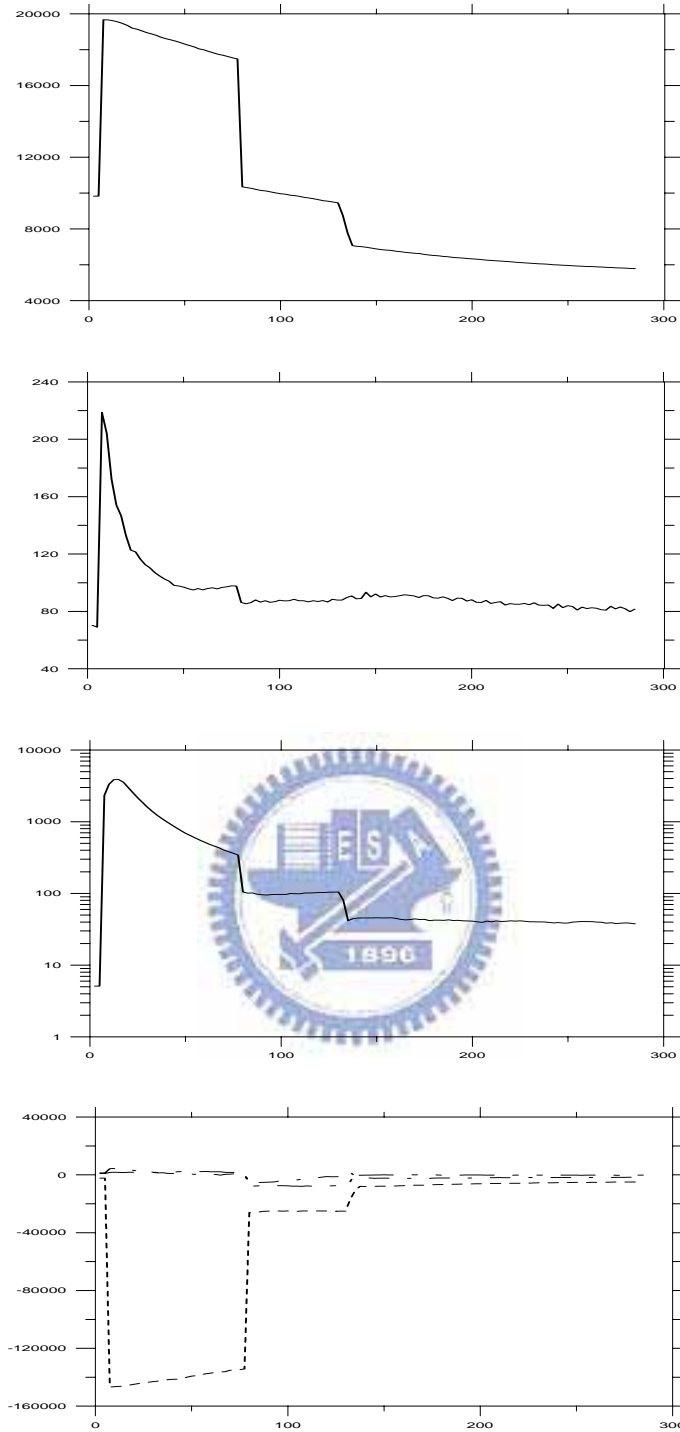
Fig. 4.37   Measurements of largest fragment of droplet pair collision **under vacuum**, b=0.25, V=250 *m/s*, (a)Number of atoms, (b)Vibrational temperature (k), (c)Rotational energy, (d)Angular momentum, respectively. This case is classified in **Coalescence** regime.
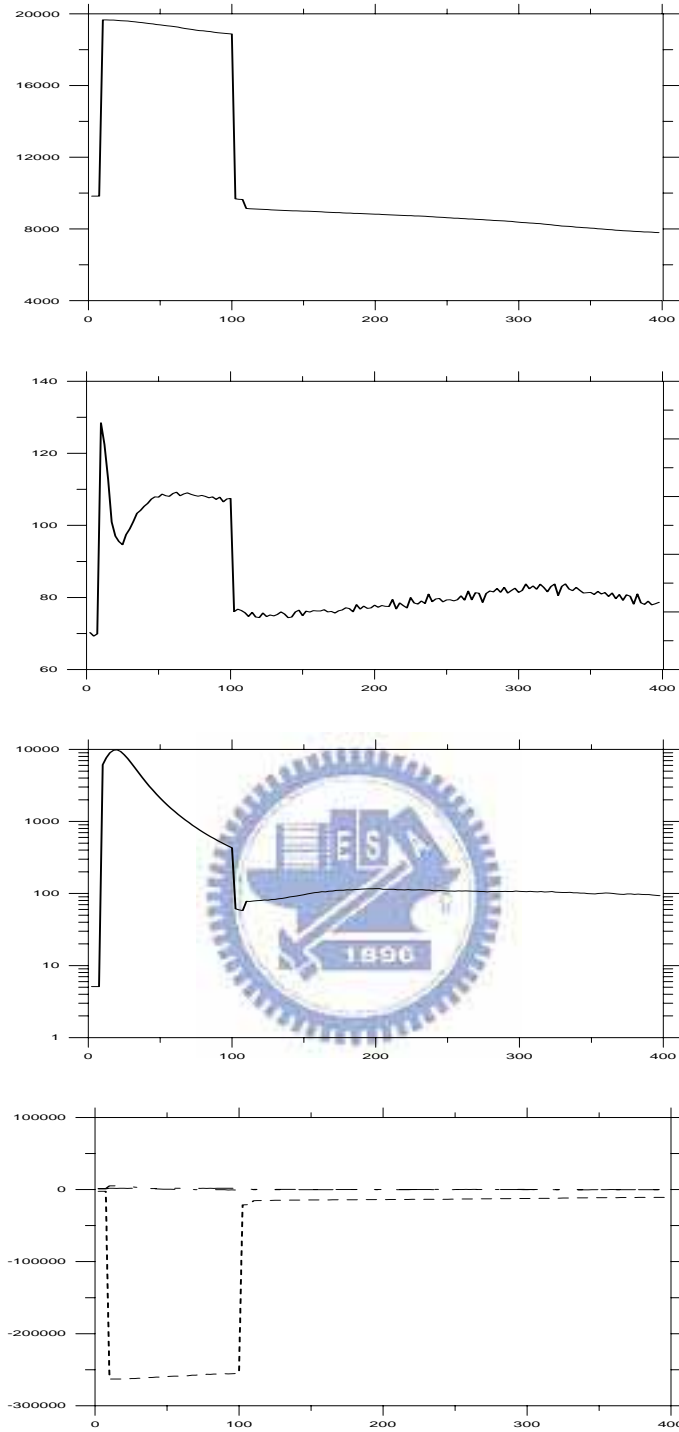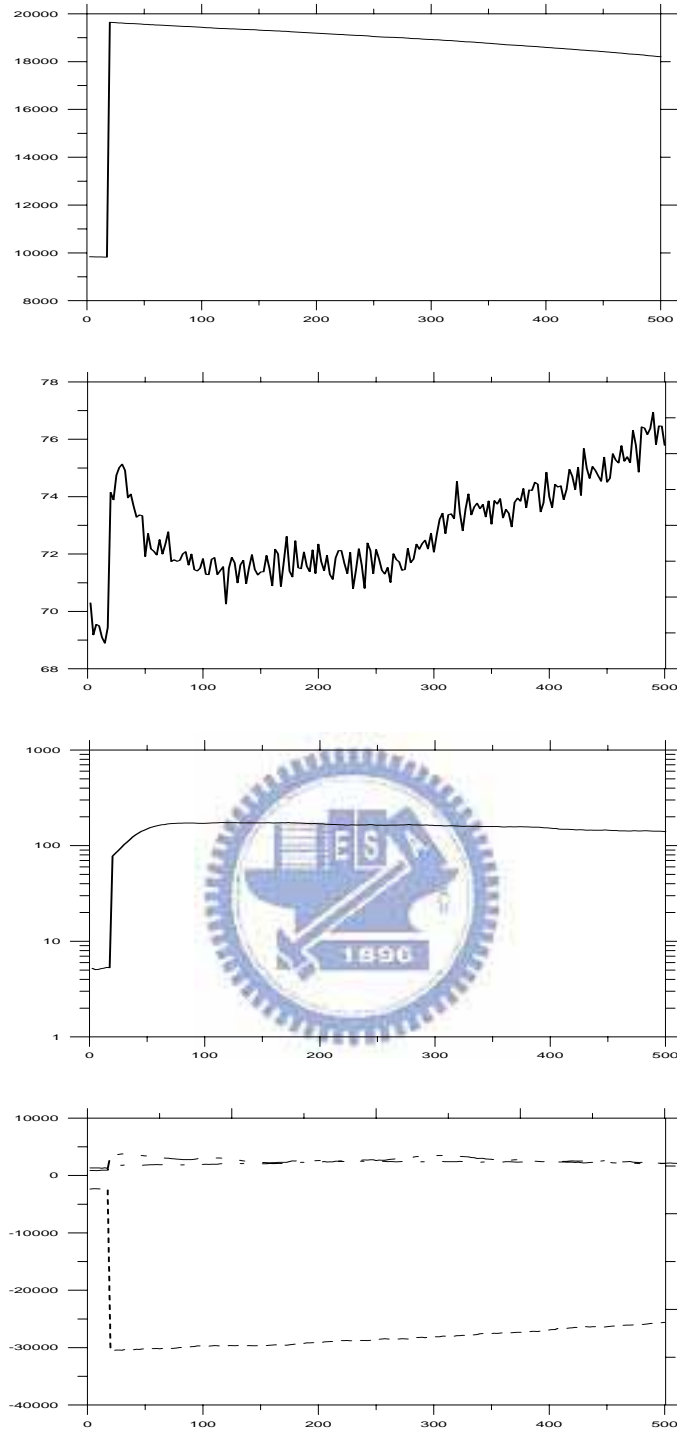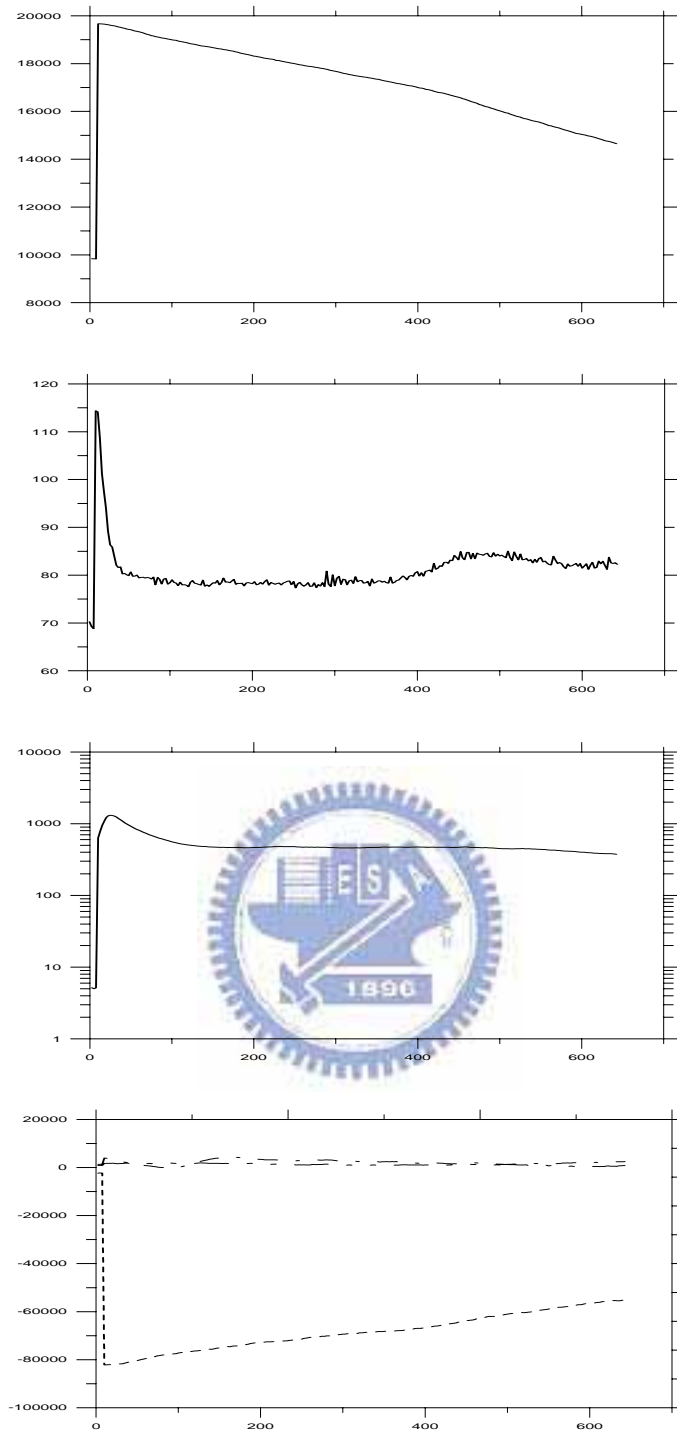
Fig. 4.38   Measurements of largest fragment of droplet pair collision **under vacuum**, b=0.625, V=1000 *m/s*, (a)Number of atoms, (b)Vibrational temperature (k), (c)Rotational energy, (d)Angular momentum, respectively. This case is classified in **Stretching Separation** regime.

Fig. 4.39   Measurements of largest fragment of droplet pair collision **under vacuum**, b=0.25, V=1375 *m/s*, (a)Number of atoms, (b)Vibrational temperature (k), (c)Rotational energy, (d)Angular momentum, respectively. This case is classified in **Shattering** regime.

126

Fig. 4.40   Measurements of largest fragment of droplet pair collision **under low pressurized ambient**, b=0.25, V=250 *m/s*, (a)Number of atoms, (b)Vibrational temperature (k), (c)Rotational energy, (d)Angular momentum, respectively. This case is classified in **Coalescence** regime.

Fig. 4.41   Measurements of largest fragment of droplet pair collision **under low pressurized ambient**, b=0.25, V=750 *m/s*, (a)Number of atoms, (b)Vibrational temperature (k), (c)Rotational energy, (d)Angular momentum, respectively. This case is classified in **Stretching Coalescence** regime.
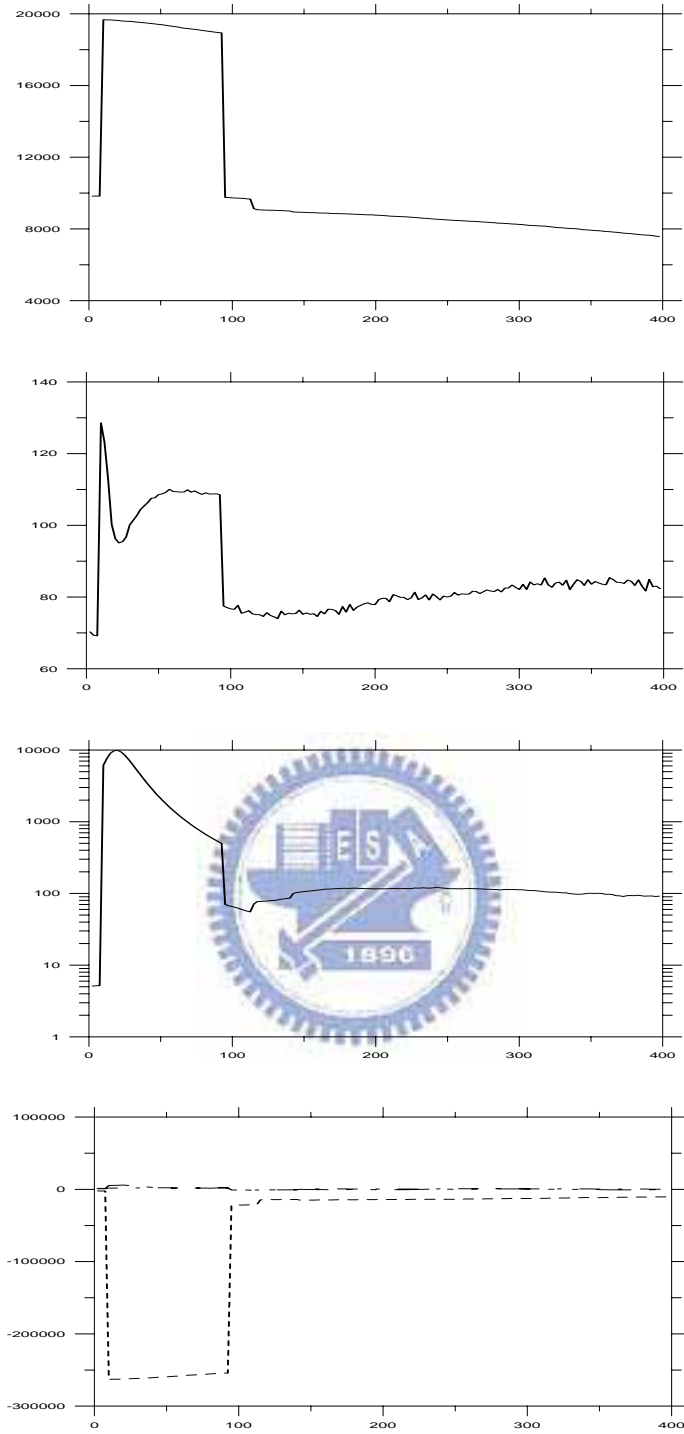
128

Fig. 4.42   Measurements of largest fragment of droplet pair collision **under low pressurized ambient**, b=0.625, V=1000*m/s*, (a)Number of atoms, (b)Vibrational temperature (k), (c)Rotational energy, (d)Angular momentum, respectively. This case is classified in **Stretching Separation** regime.
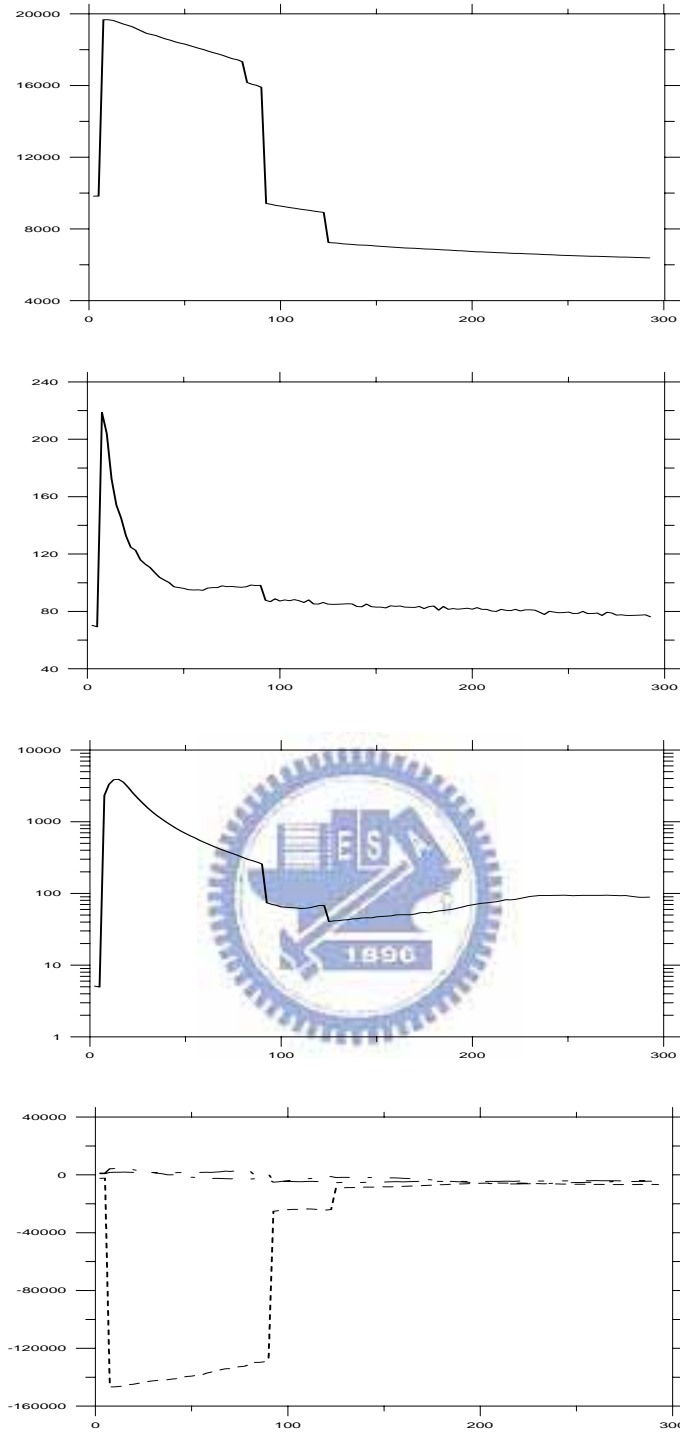
129

Fig. 4.43   Measurements of largest fragment of droplet pair collision **under low pressurized ambient**, b=0.25, V=1375*m/s*, (a)Number of atoms, (b)Vibrational temperature, (c)Rotational energy, (d)Angular momentum, respectively. This case is classified in **Shattering** regime.
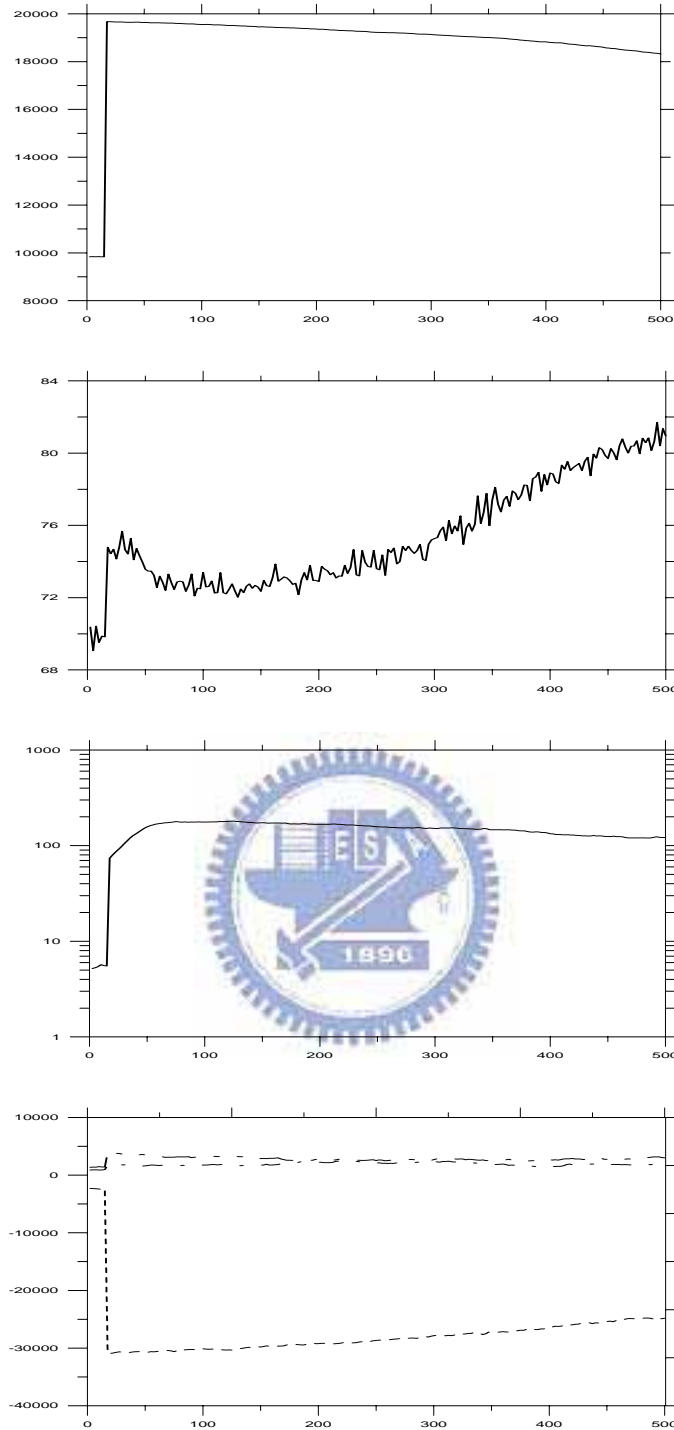
Fig. 4.44   Measurements of largest fragment of droplet pair collision **under high pressurized ambient**, b=0.25, V=250 *m/s*, (a)Number of atoms, (b)Vibrational temperature (k), (c)Rotational energy, (d)Angular momentum, respectively. This case is classified in **Coalescence** regime.
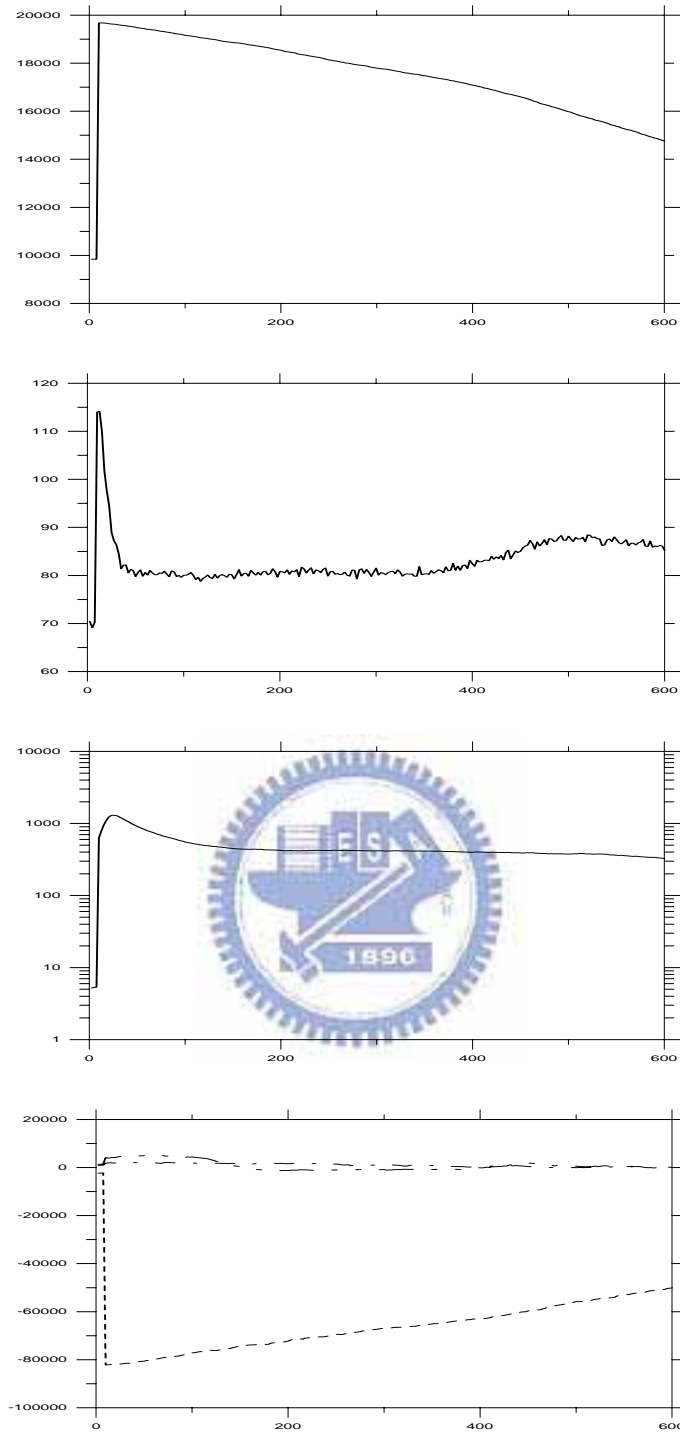
131

Fig. 4.45 Measurements of largest fragment of droplet pair collision **under high pressurized ambient**, b=0.25, V=750 *m/s*, (a)Number of atoms, (b)Vibrational temperature (k), (c)Rotational energy, (d)Angular momentum, respectively. This case is classified in **Stretching Coalescence** regime.
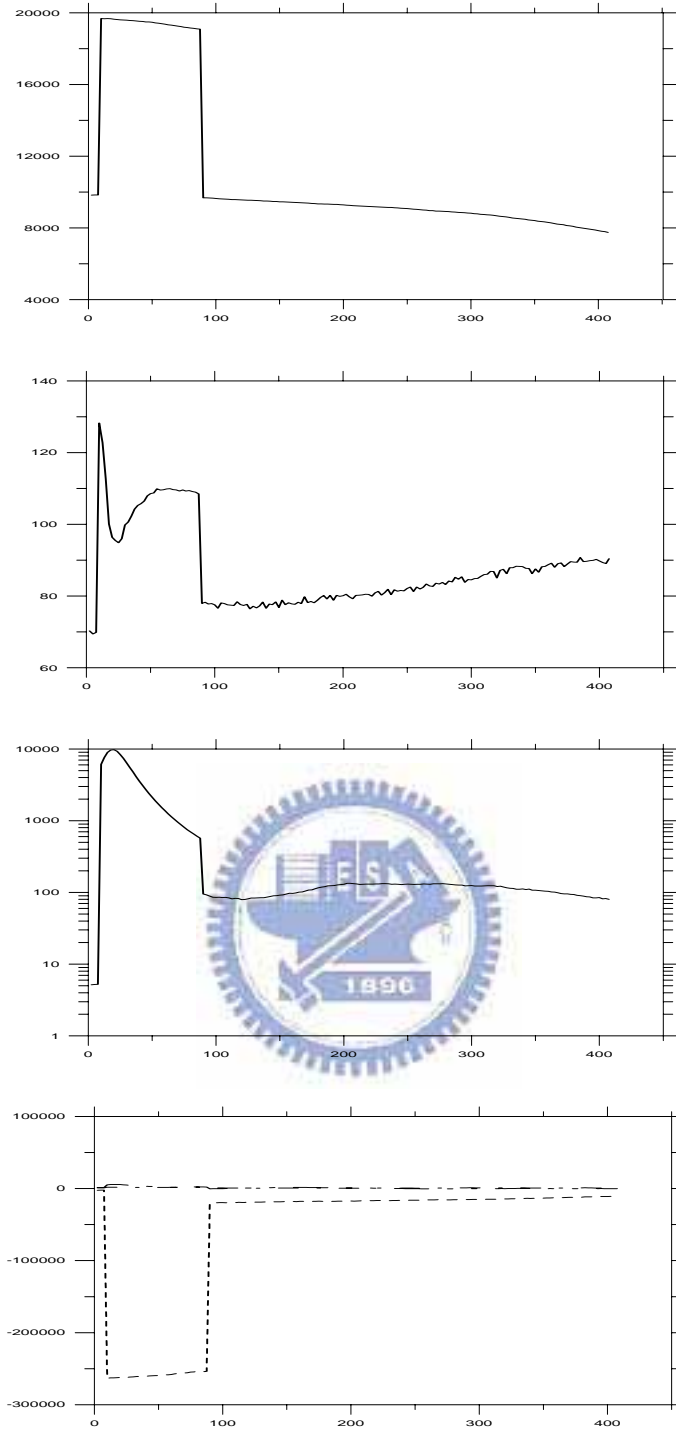
Fig. 4.46 Measurements of largest fragment of droplet pair collision **under high pressurized ambient**, b=0.625, V=1000*m/s*, (a)Number of atoms, (b)Vibrational temperature (k), (c)Rotational energy, (d)Angular momentum, respectively. This case is classified in **Stretching Separation** regime.
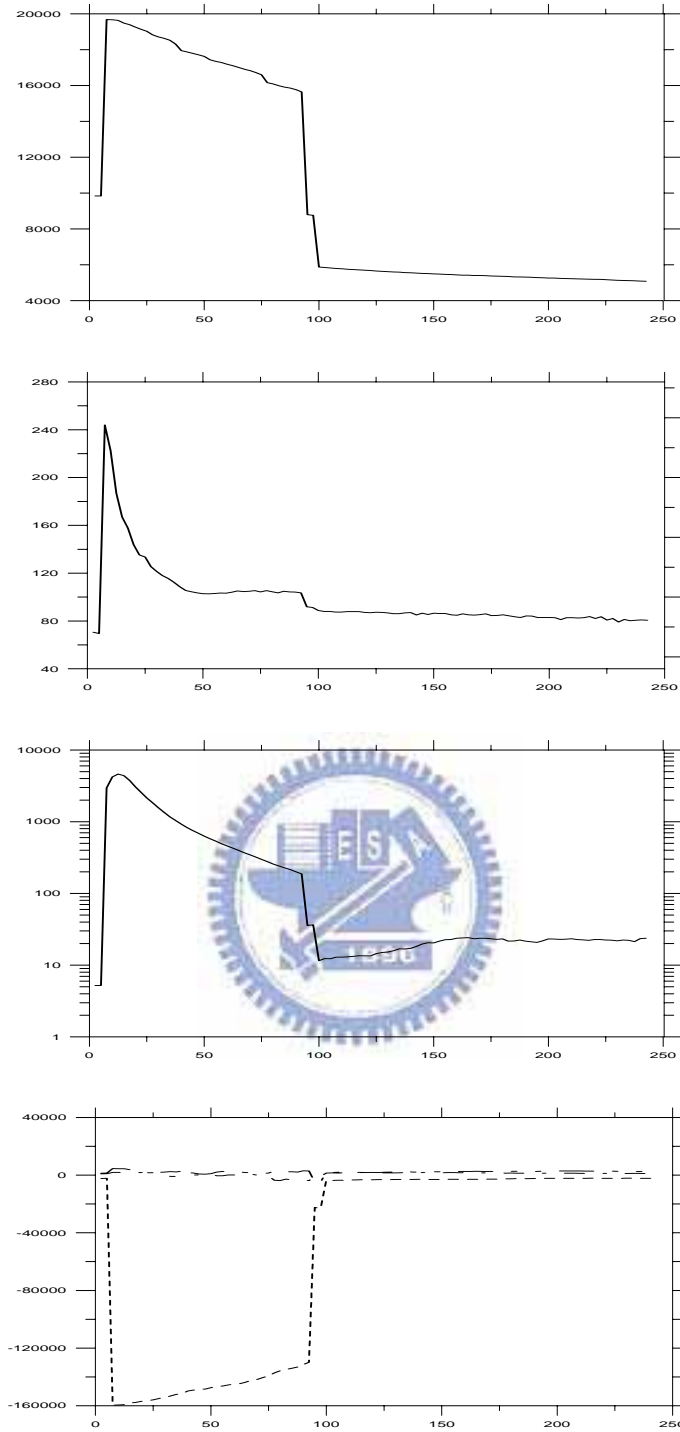
133

Fig. 4.47   Measurements of largest fragment of droplet pair collision **under high pressurized ambient**, b=0.25, V=1500*m/s*, (a)Number of atoms, (b)Vibrational temperature,   (c)Rotational energy, (d)Angular momentum, respectively. This case is classified in **Shattering** regime.
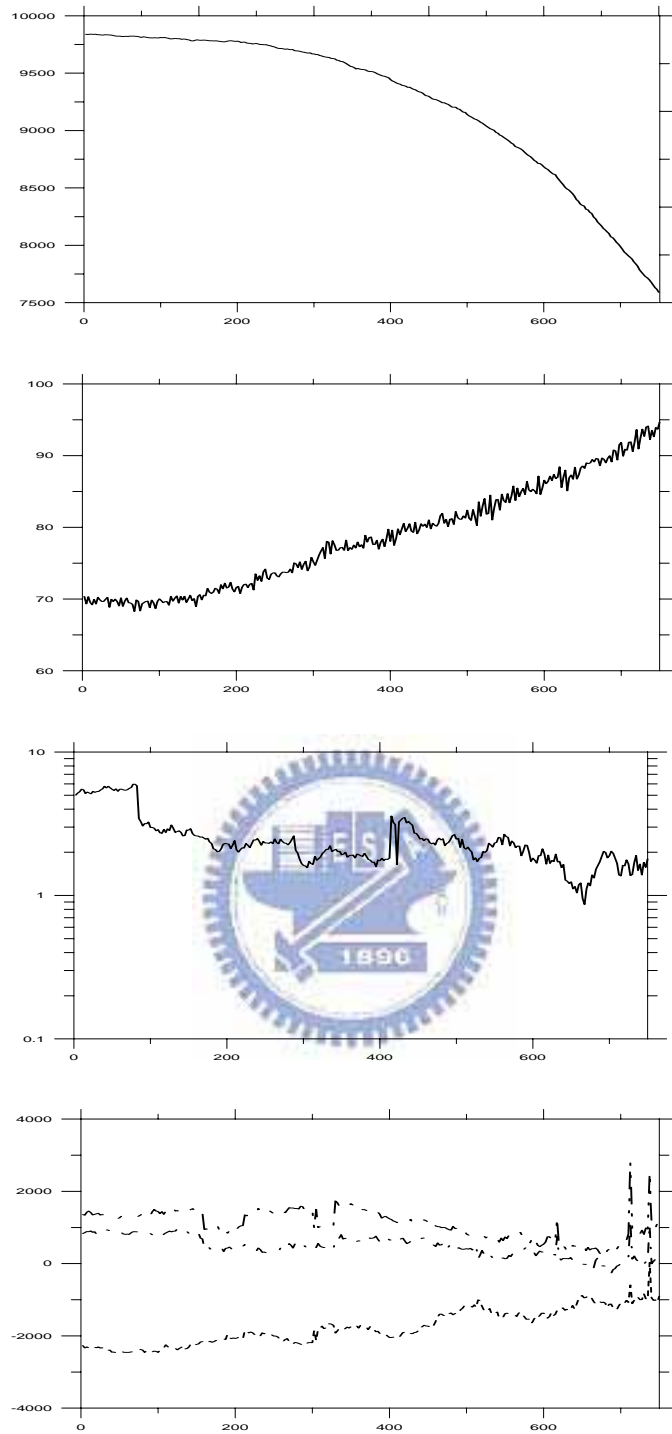
Fig. 4.48　Measurements of largest fragment of droplet pair collision **under high pressurized ambient**, b=0, V=30*m/s*, (a)Number of atoms, (b)Vibrational temperature (k), (c)Rotational energy, (d)Angular momentum, respectively. This case is classified in **Bouncing** regime.
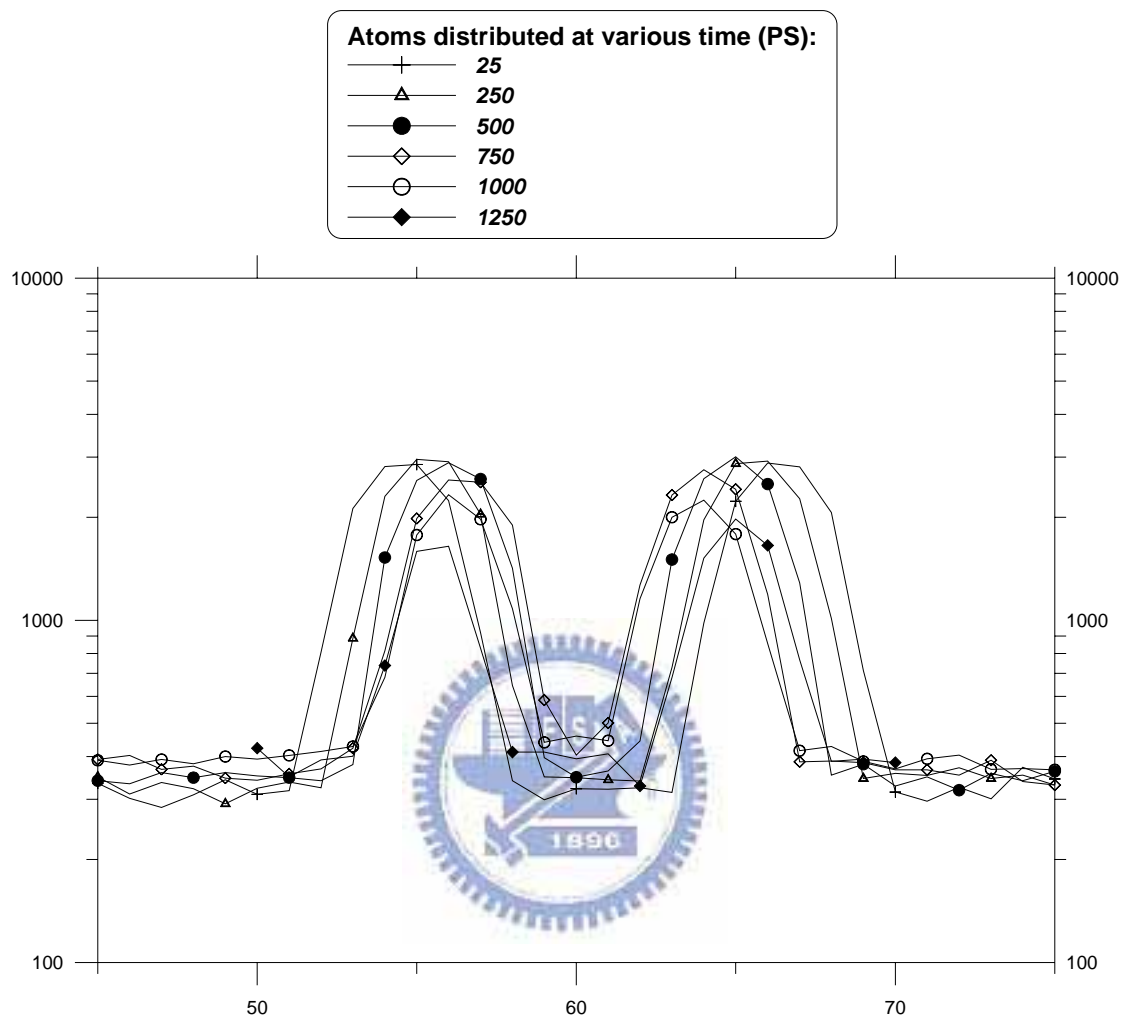
Fig. 4.49   The atoms distributions in X direction of **bounce** case **under high pressurized ambient**, b=0, V=10 *m/sec*.
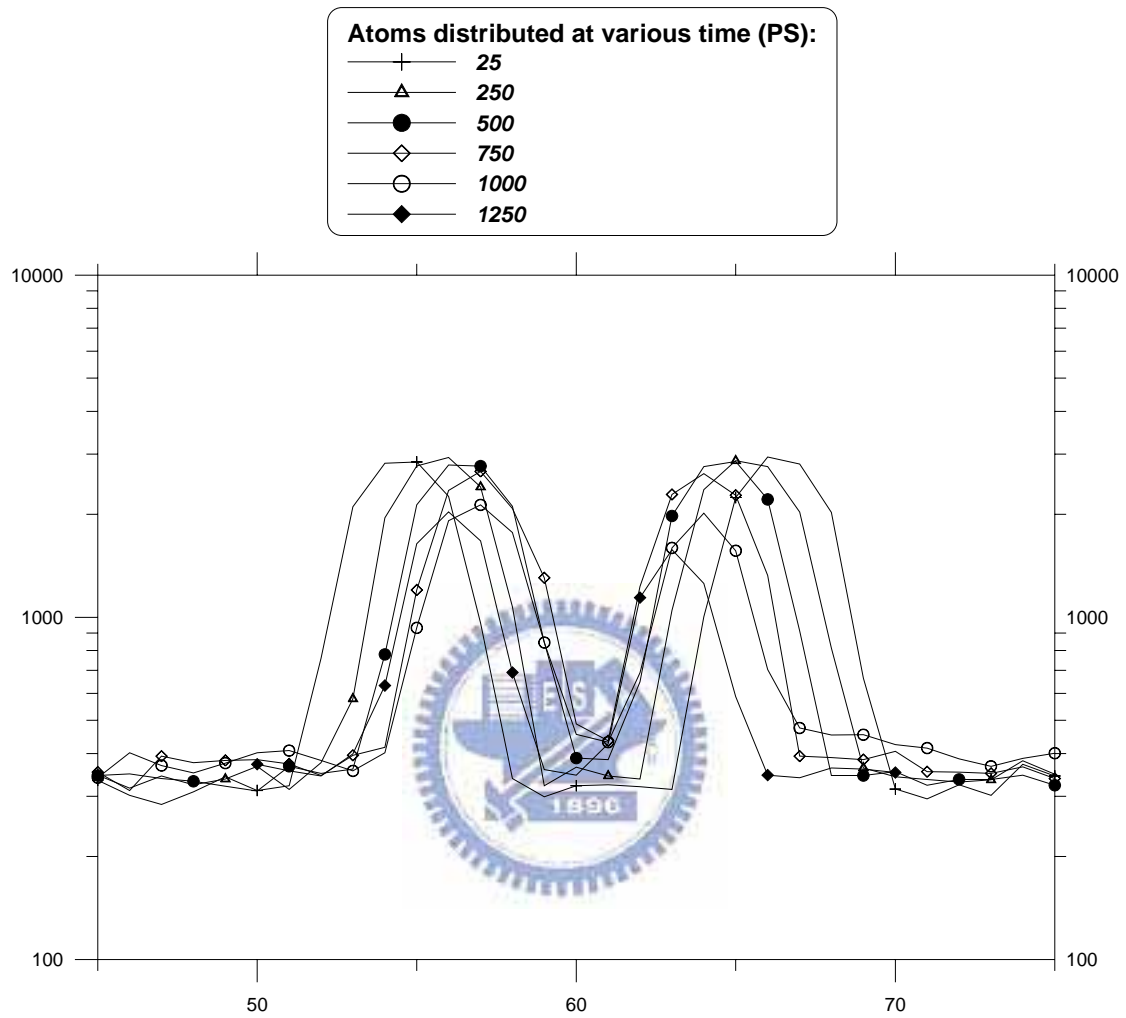
Fig. 4.50 The atoms distributions in X direction of **bounce** case **under high pressurized ambient**, b=0, V=30 *m/sec*..
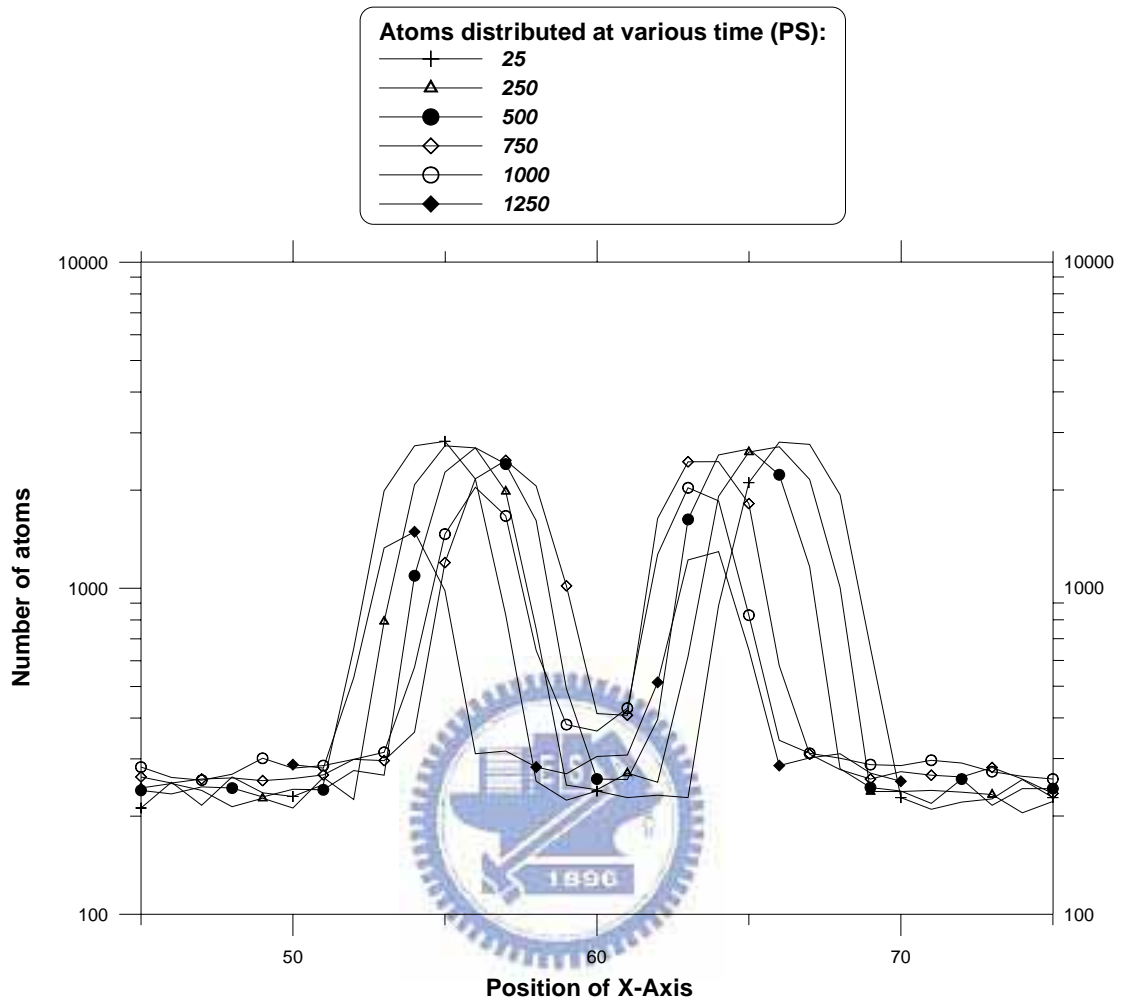
Fig. 4.51   The atoms distributions in X direction of **bounce** case **under high pressurized ambient** (0.55 atm, **T=324 K**), b=0, V=10 *m/sec*.
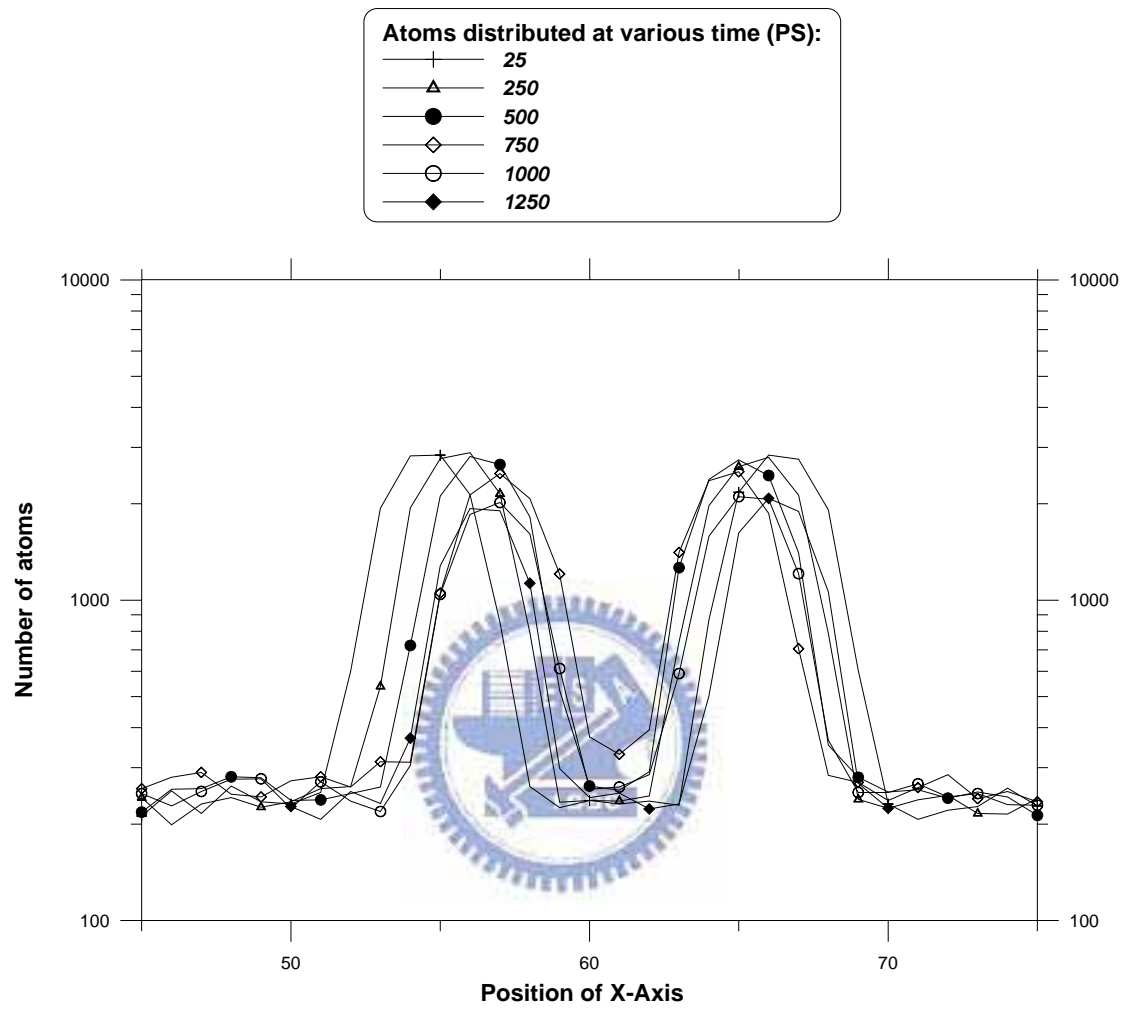
Fig. 4.52   The atoms distributions in X direction of **bounce** case **under high pressurized ambient**(0.55 atm, **T=324 K**), b=0, V=30 *m/sec.*.
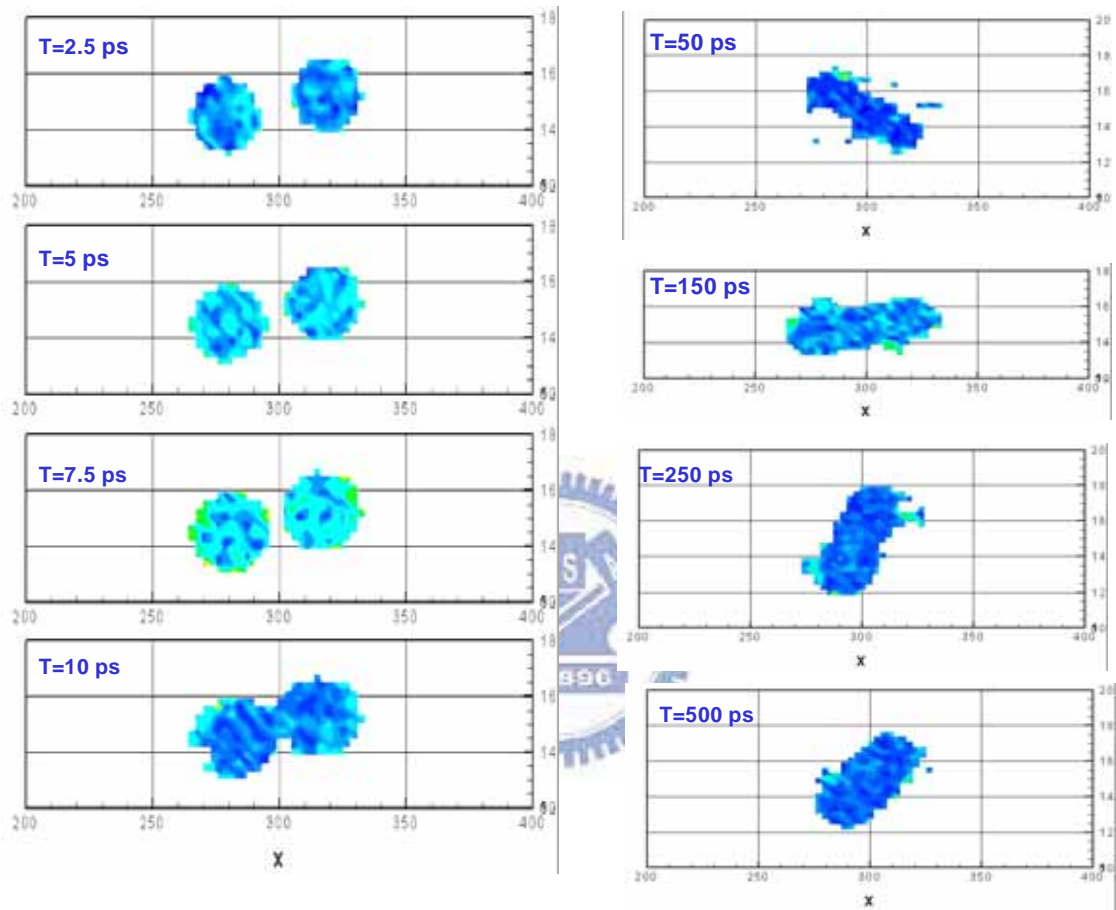
Fig. 4.53   The variation of surface tensions distributions of **coalescence** case **under low pressurized ambient** (0.055 atm, **T=216 K**), b=0.25, V=750 *m/sec.*.
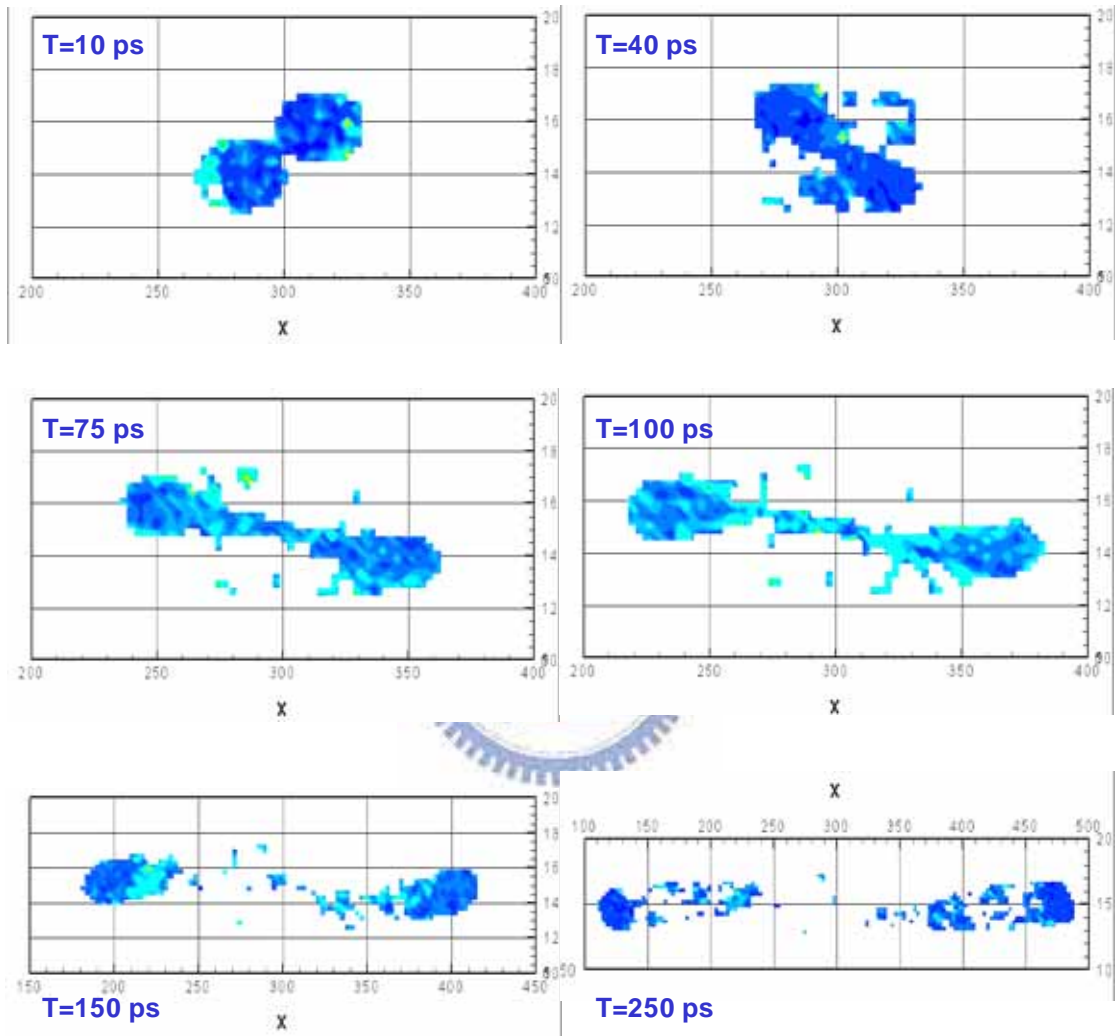
Fig. 4.54   The variation of surface tensions distributions of **separation** case **under low pressurized ambient** (0.055 atm, **T=216 K**), b=0.625, V=1000 *m/sec.*.

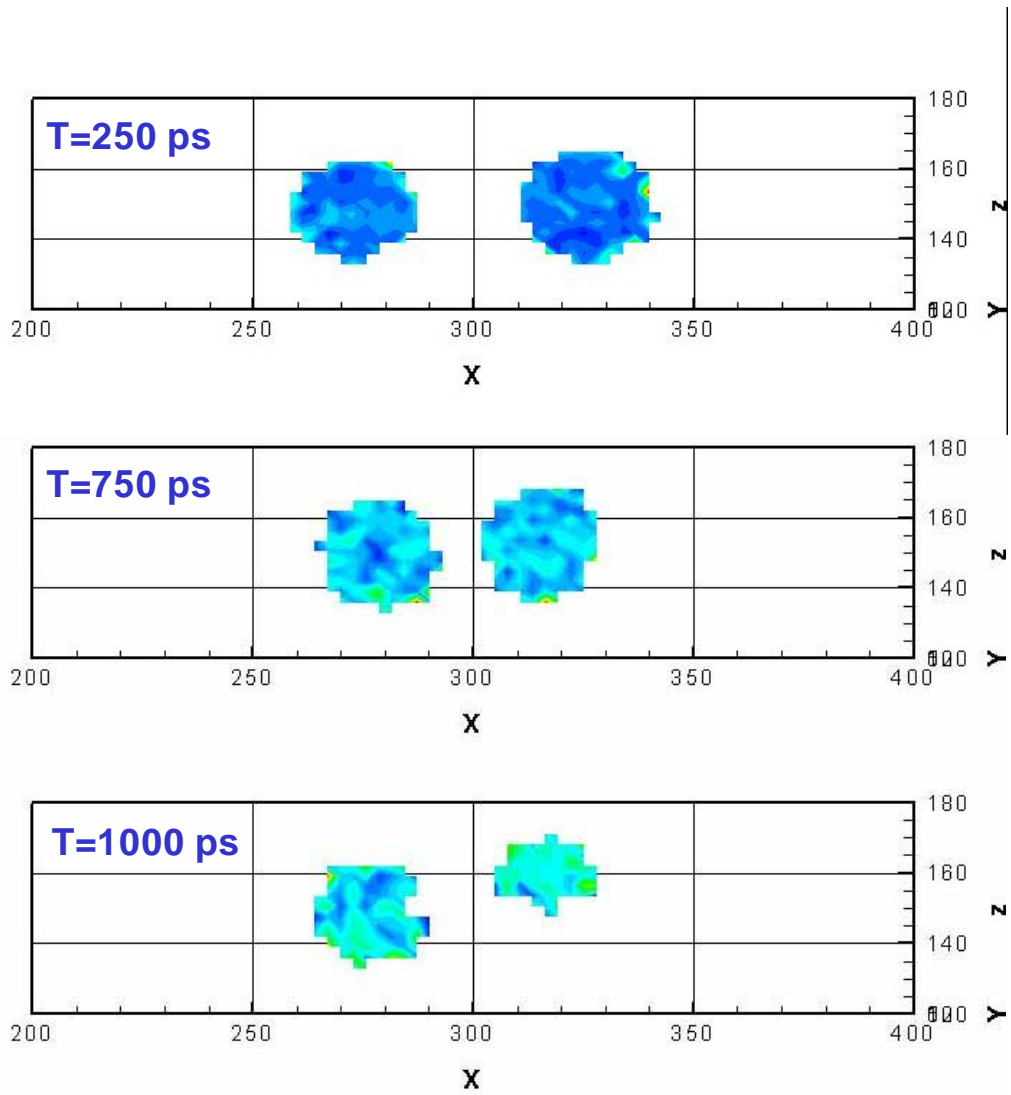Fig. 4.55　The variation of surface tensions distributions of **bouncing** case **under low pressurized ambient** (0.055 atm, **T=216 K**), b=0, V=30 *m/sec*..

Autobiography

Yu-Lin Hsu (許 祐 霖)

Phone +886-3-5712121-55175

E-mail yuyu.me88g@nctu.edu.tw

Education

1999-Pressent   **PhD Program** in Mechanical Engineering,
National Chiao-Tung University, Hsin-chu, Taiwan
The research emphasized on numerical methods of
the Parallel Cellular Molecular Dynamics simulation
(PCMD) code and analysis the Droplet-Droplet
collision dynamics by using the PCMD code.

1997-1999   **M. S.** in Mechanical Engineering,
Chung-Yuan Christian University, Chung-Li, Taiwan
The research emphasized on numerical analysis by
using the Molecular Dynamics simulation method
for studying the rupture process of thin polymer
solution films.

1995-1997   **B. S.** in Mechanical Engineering,
Yuan-Ze College of Engineering, Chung-Li, Taiwan

Language

Mandarin Chinese, Taiwanese and English

List of Publications

Referred Papers:

1. J.-S. Wu, and **Y.-L. Hsu**, "Derivation of VSS model Parameters in Direct Simulation Monte Carlo Method Using Quantum Chemistry Computation," Japanese Journal of Applied Physics, Vol. 42, pp.7574-7575, 2003.

2. J.-S. Wu, **Y.-L. Hsu** and Y.-M. Lee, "Parallel Implementation of Molecular Dynamics Simulation for Short-Ranged Interaction," Computer Physics Communications, Vol. 170, pp. 175-185, 2005.*

3. **Y.-L. Hsu**, C.-H. Chiang, Y.-M. Lee and J.-S. Wu, "MD Simulation of Two Colliding Nanoscale Argon Droplets Under Vacuum and Pressurized Environments," 2006 (Preparing).*

4. **Y.-L. Hsu**, C.-H. Chiang, Y.-M. Lee and J.-S. Wu, "MD Simulation of Two Bouncing Nanoscale Argon Droplets," 2006 (Preparing).*

International Conference Papers:

1. **Y.-L. Hsu**, J.-S. Wu, C.-H. Chiang and Y.-M. Lee, "MD Simulation of Two Colliding Nanoscale Argon Droplets Under Vacuum and Pressurized Environments," 25th Internal Symposium on Rarefied Gas Dynamics, July 21-28, 2006, Saint-Petersburg, Russia.*

National Conference Papers:

1. J.-S. Wu, **Y.-L. Hsu** and U.-M. Lee, "平行化分子動力學模擬方法之發展 (Parallel Cellular Molecular Dynamics Simulation for Short-Ranged Interaction)," The 11th National Computational Fluid Dynamics Conference (0405), 2004.*

2. J.-S. Wu, J.-S. Wu, U.-M. Lee and **Y.-L. Hsu**, "Argon 離子轟擊引致銅濺現象之分子動力學模擬(Molecular Dynamics Simulation of Sputtering of Copper Atoms Due to Argon Ion Bombardment)," The 11th National Computational Fluid Dynamics Conference (1504), 2004.

(* are those presented in this thesis)